ISSN 2672-9393

JAN.-APR. 2026 • Volume XXVII Number II

THE ASEAN JOURNAL OF RADIOLOGY

Highlight

- Original Article
- Case Report
- Classic Case
- Perspectives
- Pictorial Essay
- ASEAN Movement in Radiology

Official Journal of The

Foundation for Orphan and Rare Lung Disease

Royal College of Radiologists of Thailand

Thai Society of Vascular and Intervention Radiology

Radiological Society of Thailand

ASEAN Association of Radiology

The ASEAN Journal of Radiology

Editor:	Wiwatana Tanomkiat, M.D.
Associate Editors:	Pham Minh Thong, M.D., Ph.D.
	Narufumi Suganuma, M.D., Ph.D.
	Kwan Hoong Ng, Ph.D.
	Keerati Hongsakul, M.D.
	Siriporn Hirunpat, M.D.
	Chang Yueh Ho, M.D.
	Maung Maung Soe, M.D.
	Kyaw Zaya, M.D.
Assistant Editor:	Nucharin Supakul, M.D.
Statistical Consultant:	Alan Frederick Geater, B.Sc., Ph.D.
Language Consultant:	Siriprapa Saparat, EIL
Publishing Consultant:	Ratchada Chalarat, M.A.
Editorial Coordinator:	Supakorn Yuenyongwannachot, B.A., M.Sc.
Graphics:	Kowa Saeooi, B.A.
Publisher:	Foundation for Orphan and Rare Lung Disease

CONTENTS

THE ASEAN JOURNAL OF RADIOLOGY
ISSN 2672-9393

From The Editor

The small world we live in

Received 17 May 2026; accepted 18 May 2026
doi:10.46475/asean-jr.v27i2.1031

Wiwatana Tanomkiat, M.D.
Editor-in-Chief,
The ASEAN Journal of Radiology

Evelyn Lai Ming Ho, M.B.B.S., M.Med.*
Imaging Department, ParkCity Medical Centre, Kuala Lumpur, Malaysia

The current 2026 Iran war disrupted the Strait of Hormuz, where about a third of the global crude oil passes daily [1]. It is the only waterway connecting the Persian Gulf and Gulf countries; including Iraq, Kuwait, Qatar and UAE; to the open sea, causing severe supply shortage of petroleum products and gas to Europe and Asia. Similar to what has happened to the major Asian importers, including China, Japan, South Korea, and India; Thai people are suffering from the rising prices of gasoline, diesel, gas and fertilizers. The gasoline (Benzene 95), which was at the lowest point in the decade at 26.75 Baht/liter during the Covid-19 pandemic in 2020, increased to 52.06 Baht/liter during the Russia-Ukraine war in 2022, and has currently reached 57.51 Baht/liter in Thailand, and is even higher in Laos and Singapore [2]. The rising price of gasoline directly raises the cost of traveling which will eventually affect tourism. Tourism, which accounts for 20% of the country's GDP, is the most important sector that distributes income to Thai people of all levels, from street vendors to hotel owners. Recently, the government has limited the travel of its officers to meetings, either domestic or international.

**Evelyn Lai Ming Ho is the past president the Asian Oceanian Society of Radiology (AOSR) and currently the AOSR Honorary Advisor, committee member of AOSR Sustainability Working Group, AsiaSafe, and E-Archives Project Lead.*

Price controls on consumer goods and electricity are a short-term effort of the government to relieve the people's distress. However, it is estimated that prices will finally rise after this month especially for consumer goods because of not only the rising transportation costs, but also the rising price of plastic containers. Essential hospital consumables made of plastic—including bottles, bags and lines, cannulas, and syringes—could face disruptions as early as next month. Currently, many manufacturers are operating with barely 15–20 days of inventory. If supply chains remain unstable, hospitals could soon encounter shortages of these critical consumables.

Apart from oil and petroleum products, the supply shortage of helium, which is a byproduct of natural gas processing that rarely draws public attention, has become one of the critical issues, as Qatar ranks second after USA in terms of the amount of helium resources, production and exports in the world (Figure 1) [3]. Helium, a gas having the lowest boiling point of any element on earth, is widely used as a coolant in aerospace, semiconductor manufacturing, cutting-edge scientific research and other fields, including providing extremely low temperature (-269 degrees Celsius) for superconducting magnets, enabling modern MRI machines to operate. With the development of high-tech industries and scientific research, the global demand for helium, especially in the Asia-Pacific region, has increased year on year, mainly from high-end manufacturing, low-temperature superconductivity and the cooling gas used in the fourth-generation nuclear reactors. It is estimated that the disruption of the Strait of Hormuz will affect 30% of the global helium supply, as previously occurred in 2017 when, due to political factors, many Arab countries closed their borders with Qatar, interrupting helium production and transportation for several weeks [4]. Conventional MRI machines, depending on the device, use more than 1,000 liters of liquid helium, the only medium able to provide temperatures low enough for the coil to become superconducting (permitting electricity to flow with virtually zero resistance) and generate the stable powerful magnetic fields necessary for detailed images of the human body. Some of that helium naturally evaporates over time, so it needs periodic top-offs [5,6]. Currently, hospitals that operate MRI machines have not yet experienced severe shortages of helium. However, the price of helium in Thailand is around 20-30% higher.

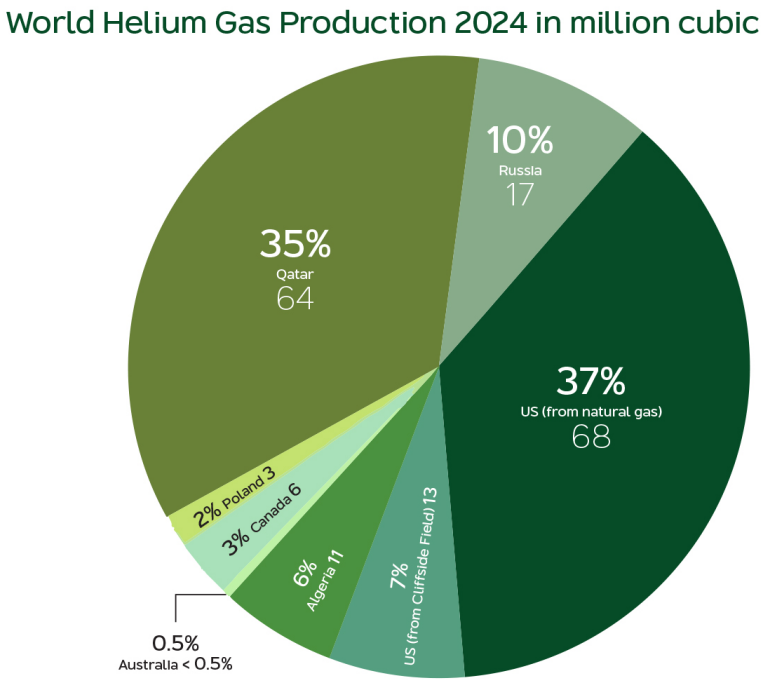

World production of helium gas in 2024 [2].

Qatar, and other gulf countries, bordering the Persian Gulf which connects with the Arabian Sea through the Strait of Hormuz.

When one door closes, another opens. While the conflicts in the Persian Gulf countries have reminded us that the global supply chain lacks flexibility, several medical imaging companies have accelerated the development of helium-efficient or even helium-free MRI systems. These new MRI systems will also have less weight and smaller dimensions, likely saving more money and paving the way for delivering MRI systems to locations where access to this technology was previously considered impossible.

This crisis of helium shortage felt variably globally should be a catalyst for many imaging departments to reduce low-value imaging, where unnecessary imaging examinations are done that did not change the management of the patient, such as overuse of MRI in low back pain or headaches without any red flags. The environmental impact and wasted resources is not just the MRI, but includes patient travel, to occupying the MRI scanner preventing another patient who really needs it, to use of contrast media, human resources, consumables, energy consumption to adding to the work burden of the radiologists and radiographers [7,8]. The "Hormuz effect" also pressures governments and consumers to rethink their reliance on petrol and diesel, leading to fast-track adoption of electric mobility and a surge in demand for clean energy storage systems, both of which are significantly manufactured in China.

MV Hondius, the ship named after the Flemish cartographer Jodocus Hondius, is an expedition cruise ship owned by Oceanwide Expeditions, based in the Netherlands. The vessel entered service in 2019 and operates primarily in the Arctic and Antarctic regions [9]. In April 2026, an outbreak of Andes virus, most commonly reported in Latin America and the only known species of the rodent-borne hantavirus that spread via human-to-human transmission, was identified on board after sailing from Argentina [10]. The route of transmission is still unknown but people are usually infected by breathing air contaminated with virus particles from rodent urine, dropping or saliva. There have so far been nine confirmed cases with 2 other probable cases, two confirmed deaths and one other probable death from the hantavirus [11]. The original passengers have now all disembarked and been evacuated; many are quarantined in their home countries. All 38 Filipino crew members have tested negative for the virus and are undergoing a 42-day quarantine in the Netherlands before repatriation to the Philippines to ensure they remain disease-free [12]. The US Centers for Disease Control and Prevention has classified the outbreak as a "level 3" emergency response while the World Health Organization (WHO) has not declared a specific level of emergency response. Symptoms of hantavirus infection varies from fever, extreme fatigue, muscle aches, abdominal pain, nausea and vomiting, and diarrhea to the most severe form, hantavirus cardiopulmonary syndrome (HCPS), which causes irregular heart rate and pulmonary microvascular leakage leading to acute pulmonary distress syndrome responsible for up to 50% mortality rate [11,13].

References

1. International Energy Agency [Internet]. Paris: IEA; 2026 [cited 2026 May 25]. Strait of Hormuz Factsheet. Available from: https://www.iea.org/about/oil-security-and-emergency-response/strait-of-hormuz

2. https://www.globalpetrolprices.com/gasoline_prices/

3. U.S. Geological Survey, Mineral Commodity Summaries, January 2016 & 2025, https://doi.org/10.3133/mcs2025

4. Anderson, S.T. Economics, Helium, and the U.S. Federal Helium Reserve: Summary and Outlook. Nat Resour Res 27, 455–477 (2018). https://doi.org/10.1007/s11053-017-9359-y

5. https://westairgases.com/blog/helium-mri-cooling/

6. https://www.mtdialog.de/artikel/auf-dem-besten-weg-zur-mrt-sicherheit

7. Kjelle E, Brandsæter IØ, Andersen ER, Hofmann BM. Sustainability in healthcare by reducing low-value imaging – A narrative review. Radiography (Lond) 2024; 30 Suppl 1: S30-4. doi: 10.1016/j.radi.2024.05.014.

8. Kjelle E, Brandsæter IØ, Andersen ER, Hofmann BM. Cost of Low-Value imaging worldwide: A systematic review. Appl Health Econ Health Policy 2024;22:485–501. doi: 10.1007/s40258-024-00876-2.

9. https://en.wikipedia.org/wiki/MV_Hondius

10. Islam M, Chughtai A, Wood J, Sawleshwarkar S, Muscatello DJ, Seale H. Hantavirus outbreak on a cruise ship in the South Atlantic. Lancet 2026;S0140-6736(26)00934-7. doi: 10.1016/S0140-6736(26)00934-7.

11. World Health Organization [Internet]. Geneva: WHO; 2026 [cited 2026 May 25]. Hantavirus cluster linked to cruise ship travel, Multi-country. 13 May 2026. Available from: https://www.who.int/emergencies/disease-outbreak-news/item/2026-DON601

12. Philippine News Agency [Internet]. Manila: PNA; 2026 [cited 2026 May 25]. Rocamora JAL. 17 Filipino crew of MV Hondius now in Netherlands for quarantine. May 12, 2026. Available from: https://www.pna.gov.ph/articles/1274806

13. World Health Organization [Internet]. Geneva: WHO; 2026 [cited 2026 May 25]. Hantavirus cluster linked to cruise ship travel, Multi-country. 8 May 2026. Available from: https://www.who.int/news-room/fact-sheets/detail/hantavirus

THE ASEAN JOURNAL OF RADIOLOGY
ISSN 2672-9393

Original Article

Comparative diagnostic efficiency of ultrasonography-guided core needle biopsy versus stereotactic-guided vacuum-assisted biopsy in breast microcalcifications: Results from a single academic institution

Rujira Patanawanitkul, M.D.
Jidapa Iamwat, M.D.
Voraparee Suvannarerg, M.D.
Tita Vachirarojpaisarn, M.D.
Shanigarn Thiravit, M.D.
From Division of Diagnostic Radiology, Department of Radiology,
Faculty of Medicine Siriraj Hospital, Mahidol University, Bangkok, Thailand.
Address correspondence to R.P. (email: rujira.paw@mahidol.ac.th)

Received 26 June 2025; revised 16 January 2026; accepted 27 February 2026
doi:10.46475/asean-jr.v27i2.965

Abstract

Background: Image-guided biopsy is essential for evaluating suspicious breast microcalcifications detected on mammography. At our institution, both ultrasonography-guided core needle biopsy (US-CNB) and stereotactic-guided vacuum-assisted biopsy (S-VAB) are routinely used based on imaging visibility and lesion characteristics.

Objective: To assess the diagnostic performance and workflow outcomes of US-CNB and S-VAB as utilized in routine clinical practice for evaluating mammographically detected microcalcifications without an associated mass.

Materials and Methods: We retrospectively reviewed 200 patients who underwent US-CNB (n=100) or S-VAB (n=100) between January 2019 and December 2023 at our institution. Clinical, imaging, and histopathological data were collected. Outcomes included the malignancy rate, DCIS underestimation rate, false-negative rate, microcalcification retrieval rate, and malignancy rate by BI-RADS category.

Results: Both biopsy methods demonstrated good diagnostic performance. US-CNB showed a higher malignancy rate (77%) than S-VAB (34%) ($p < 0.001$), attributed to imaging-driven selection of higher-risk lesions. DCIS underestimation was 42% for US-CNB and 24% for S-VAB ($p = 0.297$). One false-negative occurred in the US-CNB group. Microcalcification retrieval was confirmed in 81% of evaluated US-CNB cases and 100% of S-VAB cases ($p < 0.001$).

Conclusion: In our institutional workflow, both US-CNB and S-VAB are effective and complementary techniques. While malignancy rates differ due to imaging selection bias, diagnostic outcomes support the continued use of both methods as appropriate to lesion characteristics.

Keywords: Breast cancer, Breast microcalcifications, Core needle biopsy, DCIS underestimation, Ultrasonography-guided biopsy, Vacuum-assisted biopsy.

Introduction

Mammographically detected breast microcalcifications present a diagnostic challenge due to their potential to represent either benign conditions or early malignancies, such as ductal carcinoma in situ (DCIS) or invasive breast cancer [1]. Image-guided biopsy techniques have become indispensable for accurately characterizing these lesions and informing clinical management [2]. Among these, ultrasonography-guided core needle biopsy (US-CNB) and stereotactic-guided vacuum-assisted biopsy (S-VAB) are two prominent methods, each tailored to distinct imaging scenarios. US-CNB is typically employed when microcalcifications are visible on ultrasound, often in association with a mass, offering benefits like real-time guidance and reduced patient discomfort[3]. Conversely, S-VAB is favored for microcalcifications detectable only on mammography, leveraging stereotactic precision and vacuum assistance to retrieve larger tissue samples [4].

The diagnostic performance of these techniques has been examined in various studies. Research on US-CNB has demonstrated its effectiveness in diagnosing sonographically visible microcalcifications, with malignancy rates as high as 83.3% in some cohorts, though it may carry a higher risk of underestimating invasive components [1, 5]. S-VAB, by contrast, boosts calcification retrieval rates exceeding 95% and lowers false-negative rates, making it a reliable choice for mammogram-only lesions [6, 7].

This study seeks to address the diagnostic outcomes of US-CNB and S-VAB in patients with suspicious breast microcalcifications at our institution. We aim to compare malignancy rates, false-negative rates, and underestimation rates between these techniques. Our research intends to provide evidence-based insights for radiologists and clinicians. Such data could optimize the diagnostic approach to microcalcifications, ultimately improving patient care and outcomes in breast cancer detection.

Materials and methods

Study population

This single-center retrospective observational study was approved by the institutional review board of Siriraj Hospital (certificate of approval number Si 059/2025).

A retrospective review included female patients aged > 18 years who had microcalcifications detected on mammography and subsequently underwent either US-CNB or S-VAB at the Siriraj Breast Imaging Center between January 1, 2019, and December 31, 2023. Exclusion Criteria included a mass detected in association with the microcalcifications on the mammogram or incomplete data (e.g., no pathology reports available or no imaging follow-up for at least 1 year in cases with benign biopsy results).

The sample size was calculated to study the DCIS underestimation rate between US-CNB and S-VAB. Based on a previous study by Bae et al[1], the underestimation rate for US-CNB was 42% (5/12) and for S-VAB was 8.6% (3/35). For this study, we estimated an underestimation rate of 25% in the US-CNB group compared to 10% in the S-VAB group. Setting a two-sided $\alpha = 0.05$ and aiming for 80% power, the required sample size was calculated to be n=100 for the US-CNB group and n=100 for the S-VAB group. Patients were assigned to the US-CNB or S-VAB group based primarily on the sonographic visibility of the target microcalcifications or associated findings, reflecting standard clinical practice.

Imaging technique

Mammography was performed with the Fujifilm Amulet full-field digital mammography system (Fujifilm, Tokyo, Japan). The standard craniocaudal and mediolateral oblique views were routinely obtained along with additional magnification views upon request. If the correlation of calcifications on mammogram and ultrasound was uncertain, a radio-opaque marker was placed on the skin at the location of the lesion to confirm its position on mammography.

Ultrasound was performed in every case using one of the high-resolution US units with a linear probe of at least 12 MHz (Logiq E9, E10 (GE Medical Systems, Milwaukee, WI, USA), Aplio i700 (Canon Medical Systems, Otawara, Japan), Aplio 500 (Toshiba Medical Systems, Tokyo, Japan)).

Biopsy procedure and management

S-VAB and US-CNB were performed using distinct techniques tailored to the imaging visibility of microcalcifications. The procedure was conducted by a breast imaging specialist or a fellowship trainee under supervision of one of four breast imaging specialists with 5-30 years of experience.

US-CNB used a 14-gauge automated needle (Magnum reusable core biopsy gun, Bard, USA), guided by real-time ultrasound to target sonographically visible calcifications or associated masses. The number of cores obtained was recorded. Specimen radiography in the US-CNB group was performed selectively based on the radiologist's preference and technical confidence in lesion targeting. For S-VAB was performed using digital breast tomosynthesis (DBT)-guided biopsy of suspicious calcification, with patients positioned in a lateral decubitus or upright position for stereotactic guidance by Fujifilm Amulet full-field digital mammography add-on biopsy system (Fujifilm, Tokyo, Japan). No device allowing a lateral arm approach was available. A 9-gauge standard vacuum-assisted breast biopsy device (Atec, Hologic, Massachusetts, USA) was utilized to obtain tissue samples in every case. The procedure typically included a scout image, prefire image, postfire image and after clip placement (if any). Specimen radiograph was conducted routinely to confirm calcification retrieval in the S-VAB group. For ultrasound-guided core needle biopsy, a 14-gauge automated needle was used, and typically 4–5 cores were obtained per lesion according to institutional practice. For stereotactic-guided vacuum-assisted biopsy, a 9-gauge vacuum-assisted device was used, and generally 6–8 cores were retrieved per lesion based on institutional protocol. Patients with histopathological results of malignancy, atypical ductal hyperplasia, or discordant benign lesions proceeded to surgery. The final surgical pathology was considered the reference standard. Patients who did not undergo surgery were scheduled

for follow-up at 6 and 12 months. If the lesion progressed, surgery or re-biopsy was performed. However, the decision for surgery was determined by the surgeons.

Data analysis

Data were gathered from medical records, radiology reports and pathology reports to comprehensively characterize the US-CNB and S-VAB groups.

The primary outcome included the malignancy rate, the DCIS underestimation rate and the false negative rate.

The malignancy rate was calculated as the proportion of cases diagnosed as DCIS or invasive cancer. The DCIS underestimation rate was determined by the proportion of initial DCIS cases upgraded to invasive ductal carcinoma (IDC) at surgery, and the false negative rate was determined by the proportion of cases initially diagnosed as benign by the respective image-guided biopsy method (US-CNB or S-VAB) that were subsequently found to have malignancy upon definitive surgical excision or during the minimum one-year imaging follow-up period for those not undergoing surgery.

The secondary outcome was microcalcification retrieval rate and the malignancy rate according to BI-RADS category. The microcalcification retrieval rate was defined as the presence of microcalcifications on specimen radiographs.

The variables collected encompassed demographic details such as age, clinical symptoms (e.g., palpable mass, nipple discharge), and history of prior biopsies, alongside mammographic features including BI-RADS categories, breast composition, and calcification shape and distribution. For the US-CNB group, ultrasound-specific lesion characteristics, such as size, mass shape, margins, and echogenicity, were recorded. Biopsy-related data included the number of core specimens, presence of microcalcifications on specimen radiograph, initial CNB histological results (benign, DCIS, or invasive cancer), final histology post-surgery (within one year of follow-up), and the rate of upgrades from DCIS to invasive cancer.

Comparative analyses utilized chi-square tests for categorical data and t tests for continuous variables.

Statistical analyses were performed using SPSS 20.0 software (SPSS Inc., Chicago, IL, USA). P-values < 0.05 were considered statistically significant.

Results

Patient demographics and mammographic features

A total of 200 patients with suspicious breast microcalcifications were analyzed, with 100 undergoing ultrasonography-guided core needle biopsy (US-CNB) and 100 undergoing stereotactic-guided vacuum-assisted biopsy (S-VAB).

Patients' demographic data and mammographic features were summarized in table 1. Breast composition did not differ in both groups and was predominantly heterogeneously dense (75% and 71%, p = 0.42). The mean age was 52.6 years in the US-CNB group, significantly lower than 56.4 years in the S-VAB group (p = 0.005). Clinical symptoms were present in 39% of US-CNB patients, predominantly palpable masses (87%), compared to 3% in the S-VAB group (p < 0.001). BI-RADS categories showed significant differences, with the US-CNB group having a higher proportion of category 5 lesions (47%) and fewer 4A lesions (16%), while S-VAB group had more 4A (41%) and 4B (47%) lesions (p < 0.001). Calcification shape varied significantly, with fine pleomorphic shapes predominant in the US-CNB group (42%) and amorphous shapes in S-VAB (51%) (p < 0.001). Distribution patterns of calcifications also differed significantly, with segmental calcifications more common in US-CNB (20%) and grouped calcifications in S-VAB (71%) (p < 0.001).

Table 1. *Patient's demographic data and mammographic features according to biopsy methods.*

Parameter	US-CNB (n=100)	S-VAB (n=100)	p-value
Age (mean ± SD)	52.6 ± 9.3	56.4 ± 9.5	0.005
Clinical symptoms	39 (39)	3 (3)	<0.001
• Palpable mass	34/39 (87)	1/3 (33)	
• Nipple discharge	3/39 (8)	1/3 (33)	
• Nipple retraction	1/39 (3)	0 (0)	
• Pain	0 (0)	1/3 (33)	
• Skin retraction	1/39 (3)	0 (0)	
History of prior biopsies	3 (3)	11 (11)	0.027

Parameter	US-CNB (n=100)	S-VAB (n=100)	p-value
BI-RADS			<0.001
• 4A	16 (16)	41 (41)	
• 4B	23 (23)	47 (47)	
• 4C	14 (14)	11 (11)	
• 5	47 (47)	1 (1)	
Breast composition			0.42
• Almost entirely fatty	0 (0)	0 (0%)	
• Scattered fibroglandular	2 (2)	6 (6%)	
• Heterogeneously dense	75 (75)	71 (71)	
• Extremely dense	23 (23)	23 (23)	
Shape of calcifications			<0.001
• Amorphous	17 (17)	51 (51)	
• Coarse Heterogeneous	15 (15)	18 (18)	
• Fine Linear/Fine linear branching	8 (8)	9 (9)	
• Fine Pleomorphic	42 (42)	14 (14)	
• Round	18 (18)	8 (8)	
Distribution of calcifications			<0.001
• None	9 (9)	0 (0)	
• Diffuse	6 (6)	1 (1)	
• Grouped	47 (47)	71 (71)	
• Linear	2 (2)	5 (5)	
• Regional	16 (16)	17 (17)	
• Segmental	20 (20)	6 (6)	

Note: Data are numbers with percentages in parentheses unless indicated otherwise.

Ultrasound features of US-CNB lesions were described in Table 2.

Table 2. *Ultrasound features of US-CNB lesions.*

Characteristics	n = 100
Location of calcification	
• Inside a mass	81/100 (81)
• Intraductal calcification	11/100 (11)
• Outside a mass or duct	8/100 (8)
Lesion size (mm, median (range))	16.5 (3.9, 66)
Shape of associated mass	
• Irregular	55/81 (68)
• Oval	25/81 (31)
• Round	1/81 (1)
Orientation of associated mass	
• Not parallel	4/81 (5)
• Parallel	77/81 (95)
Margins of associated mass	
• Circumscribed	8/81 (10)
• Angular	4/81 (5)
• Indistinct	42/81 (52)
• Microlobulated	6/81 (7)
• Spiculated	21/81 (26)
Echogenicity of lesions	
• Complex Cystic and solid	1/81 (1)
• Heterogeneous	6/81 (8)
• Hypoechoic	74/81 (91)

Characteristics	n = 100
Posterior Feature	
• No posterior feature	67/81 (81)
• Enhancement	1/81 (1)
• Shadowing	9/81 (11)
• Combined pattern	6/81 (7)
Associated features	
• Ductal changes	16/31 (52)
• Architectural distortion	12/31 (39)
• Skin thickening	2/31 (6)
• Edema	1/31 (3)

Note: Data are numbers with percentages in parentheses unless indicated otherwise.

Primary outcome: Malignancy rate, DCIS underestimation rate and false negative rate

Malignancy rates were 77% for US-CNB and 34% for S-VAB ($p < 0.001$). Among lesions with malignancy pathology, invasive carcinoma was more frequent in the US-CNB group (53%) than in S-VAB (9%) with significant difference. (Table 3)

Table 3. *Biopsy details and histopathology according to biopsy methods.*

Parameter	US-CNB (n=100)	S-VAB (n=100)	p-value
Number of core specimens (Median(range))	5 (3, 9)	10 (6, 22)	< 0.001
Microcalcifications on specimen radiograph			< 0.001
Yes	35/43 (81)	100/100 (100)	
No	8/43 (19)	0 (0)	
Initial biopsy result			< 0.001
Benign	23 (23)	66 (66)	
Invasive cancer	53 (53)	9 (9)	
DCIS	24 (24)	25 (25)	
Surgery	81/100 (81)	46/100 (46)	< 0.001
Benign	3/81 (4)	12/46 (27)	
Malignant	78/81 (96)	34/46 (73)	
Upgrade from DCIS to IDC at surgery	10/24 (42)	6/25 (24)	0.187

The underestimation of DCIS which means an upgrade from DCIS to IDC at surgery, was 42% (10/24) for US-CNB and 24% (6/25) for S-VAB, with no significant difference (p = 0.187) (Figures 1 and 2)

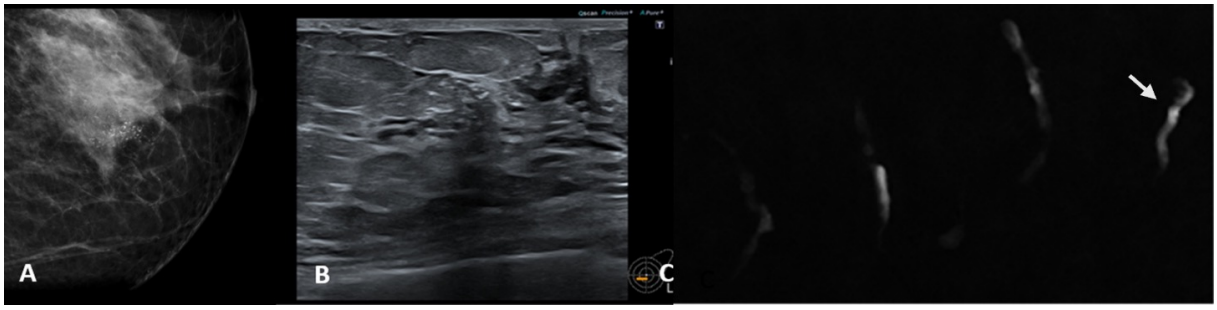

Figure 1. *A case with pathology upgraded from DCIS on CNB to IDC at surgery from the US-CNB group.*
(A) Mammogram shows fine pleomorphic and coarse heterogeneous microcalcifications in a segmental distribution at the left central to lower inner quadrant (LIQ), measuring 43.8 × 21.6 mm (BI-RADS 4B). (B) Corresponding ultrasound reveals a prominent duct with intraductal calcifications in the same region. (C) Specimen radiograph of US-CNB confirms microcalcifications in one of the five obtained cores. The initial pathology showed DCIS, intermediate nuclear grade, solid and cribriform patterns with comedonecrosis. Subsequent mastectomy revealed moderately differentiated IDC (histologic grade 2) along with residual DCIS.

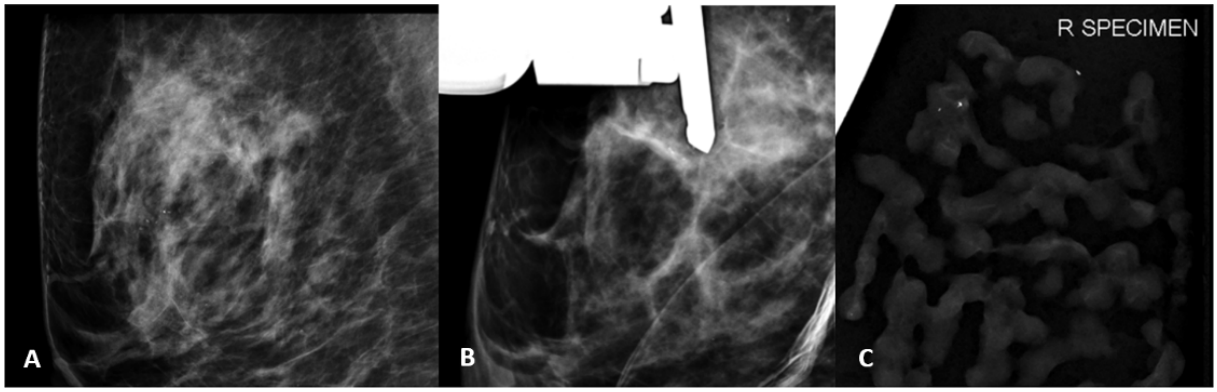

Figure 2. *A case with pathology upgraded from DCIS on CNB to IDC at surgery from the S-VAB group.*
(A) Mammogram reveals coarse heterogeneous microcalcifications in a linear distribution at the right upper breast (BI-RADS 4B). (B) S-VAB was performed under stereotactic guidance with 16 cores obtained. (C) Specimen radiograph confirms microcalcifications in four of the retrieved cores. The initial pathology demonstrated DCIS. Subsequent excisional biopsy revealed invasive ductal carcinoma.

One false negative case was identified in US-CNB group, and none were found in the S-VAB group. The false negative case presented with grouped fine pleomorphic calcifications on mammography and ultrasound-visible oval, indistinct hypoechoic mass. The ultrasound-guided CNB yielded five core specimens containing microcalcifications in one core. The initial biopsy result was benign breast tissue with dense collagenous and fibrotic stroma, with a focal pseudoangiomatous stromal hyperplasia-like appearance. Therefore, discordant radio-pathologic correlation was suspected, requiring surgical excision. The surgical pathology yielded atypical ductal hyperplasia with a focus of DCIS (Figure 3).

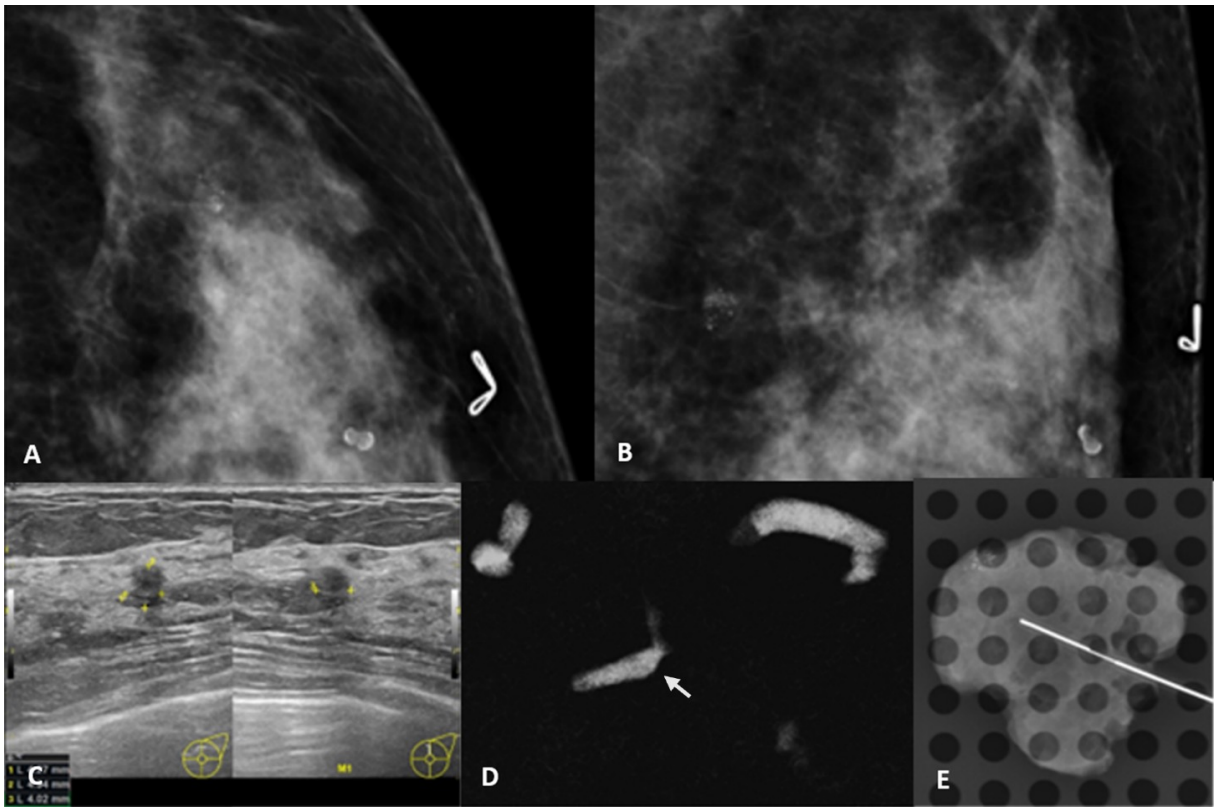

Figure 3. *A false negative case in US-CNB group.*
(A, B) Craniocaudal and mediolateral oblique mammograms show grouped fine pleomorphic microcalcifications at the upper outer quadrant (UOQ) of the left breast (BI-RADS 4B). (C) Ultrasound images reveal an oval, indistinct, hypoechoic mass measuring 4.9 mm without posterior acoustic features. (D) Specimen radiograph demonstrates microcalcifications within one of the four biopsy cores. (E) Biopsy setup showing targeting of the lesion under ultrasound guidance. Initial US-CNB pathology was benign fibrous tissue with dense collagenous and fibrotic stroma, with focal pseudoangiomatous stromal hyperplasia-like features. Due to discordant imaging-pathologic findings, surgical excision was performed and revealed atypical ductal hyperplasia with a focus of DCIS.

Secondary outcome: Microcalcification retrieval rate and malignancy rate according to BI-RADS category

Specimen radiography was performed in 43/100 cases in the US-CNB group, and all (100/100) in the S-VAB group. Microcalcification retrieval rate on specimen radiograph significantly differed between groups with US-CNB retrieving calcifications in 81% (35/43), failing in 8 cases (8/43) but successful S-VAB retrieving calcifications in 100% ($p < 0.001$) (Table 3).

The malignancy rate according to BI-RADS category was reported in Table 4. Most malignancy rates by BI-RADS category conformed to the published data in the BI-RADS manual. However, in the BI-RADS 4A category, the malignancy rate was 38% in US-CNB group and 20% in S-VAB group, which exceeded the expected range indicated in the BI-RADS manual.

Table 4. *Malignancy rates by BI-RADS category.*

BI-RADS Category	Malignancy Rate	
	US-CNB (n=100)	S-VAB (n=100)
4A	6/16 (38)	8/41 (20)
4B	13/23 (57)	17/47 (36)
4C	12/14 (86)	9/11 (73)
5	46/47 (98)	1/1 (100)

Note: Data are numbers with percentages in parentheses.

Discussion

Our results demonstrated the diagnostic outcomes of US-CNB and S-VAB for suspicious breast microcalcifications at a single tertiary-care institution. The results show that the malignancy rate was significantly higher in the US-CNB group (77%) compared to the S-VAB group (34%) ($p < 0.001$). There was one false negative case (1/100) in US-CNB group while there is none in the S-VAB group and there was no significant difference of the DCIS underestimation rate between the two groups (42% for US-CNB versus 24% for S-VAB; $p = 0.187$).

THE ASEAN JOURNAL OF RADIOLOGY
ISSN 2672-9393

The significant higher malignancy rate in the US-CNB group compared to the S-VAB group could be explained and was biased by differences in clinical indications for each procedure. The US-CNB group included a higher proportion of lesions with strong predictors of malignancy, such as BI-RADS 5 assessments (47% vs 1%), fine pleomorphic calcifications (42% vs 14%), segmental distribution (20% vs 6%), the presence of clinical symptoms (39% vs 3%), and associated ultrasound-visible masses (81%). These features are well known to correlate with a higher risk of malignancy[1, 8]. In contrast, the S-VAB group mainly consisted of lower-risk lesions, including a higher proportion of BI-RADS 4A and 4B assessments (88%) and amorphous calcifications (51%). Therefore, the higher malignancy rate observed in the US-CNB group reflects the higher-risk nature of the lesions selected for biopsy, rather than a true difference in the diagnostic performance between US-CNB and S-VAB.

In this study, one false-negative case was identified in the US-CNB group, while none were identified in the S-VAB group. This underscores the importance of radiologic-pathologic correlation[1, 9]. In concordance with Youk et al., who reported a false-negative rate of 2.5% for US-CNB in breast masses with DCIS being the most frequently missed diagnosis [9]. In our case, the biopsy result with US-CNB initially revealed benign. However, due to imaging-pathology discordance, surgical excision was pursued and the final pathology subsequently revealed DCIS. This false-negative outcome is possibly explained by insufficient sampling, as the tissue obtained may not have adequately represented the full extent of the lesion. Only one of the five cores contained microcalcifications. Bagnall (2000) showed that increased sensitivity of the stereotactic biopsy for calcifications was related to the number of calcifications on specimen radiography, with three or more cores containing calcium achieving 100% sensitivity [10]. Emphasizing the importance of obtaining an adequate number of calcifications in the tissue cores to minimize the risk of underdiagnosis [5, 10, 11]. No false negatives were found in the S-VAB group, consistent with the high reliability reported for VAB [4, 7].

The rate of upgrade from DCIS to IDC at surgery was numerically higher for US-CNB (42%, 10/24) than for S-VAB (24%, 6/25), but this difference was not statistically significant ($p = 0.187$). Similar to our results, previous literature has reported lower underestimation rates for VAB compared to CNB, attributed to the larger tissue volume obtained[1, 2]. The upgrade rate with both US-CNB (using a 14-gauge needle) and S-VAB (using a 9-gauge device) in our study were also consistent with the rate reported in the previous studies[1, 6, 9, 12, 13]. The higher upgrade rate observed in the US-CNB may be due to the significantly lower number of cores obtained (median 5 for US-CNB vs 10 for S-VAB) [1, 5].

The reported microcalcification retrieval rate for S-VAB in our study was 100% (100/100 assessed cases), aligning with literature benchmarks where retrieval rates confirmed by specimen radiography typically exceed 95% for vacuum-assisted systems [1, 4, 6]. For US-CNB, calcifications were reported as retrieved in 81% (35/43) of the cases where specimen radiography was performed. Although specimen radiography was not conducted in 57% (57/100) of the US-CNB procedures, the observed retrieval rate still falls within the previously reported range of 71%–97% in studies utilizing specimen radiography for US-CNB [3, 5, 10, 14, 15].

The malignancy rate according to BI-RADS category in this study mostly follows the BI-RADS manual, except for the BI-RADS 4A category. The malignancy rate in BI-RADS 4A category exceeded the BI-RADS manual which is 38% in US-CNB group and 20% in S-VAB group. The result may be attributed to practice at our institution in which BI-RADS categories may have been under-assigned due to cognitive factors, such as conservative bias, potentially varying by radiologist experience. Based on our observations, those US-CNB BI-RADS 4A cases mostly reported with grouped coarse heterogeneous calcifications and/ or associated with an oval indistinct mass on ultrasound. In S-VAB BI-RADS 4A cases, most cases were grouped amorphous calcifications. According to the BI-RADS 2013's manual, this can be categorized as BI-RADS 4B then explaining the malignancy rate at over 10% [16].

There are several limitations in our study. First, the retrospective design introduced potential biases—the selection bias driven by differing indications based on sonographic visibility, resulting in different baseline cohorts. Second, this study may have been underpowered to detect true differences in the DCIS upgrade rate so that generalizability of this result may be limited by a single-center study. Third, specimen radiography was not done in all US-CNB cases. This may invalidate the comparison of calcification retrieval rates between two groups. Our study included cases from real practices at our institution which were circulated by breast specialist radiologists with varying experiences. An audit of a breast imaging practice and assessment of reader accuracy may provide valuable feedback for readers and facility improvement.

Conclusion

In our institutional workflow, both US-CNB and S-VAB are effective and complementary techniques. While malignancy rates differ due to imaging selection bias, diagnostic outcomes support the continued use of both methods as appropriate to lesion characteristics.

Acknowledgements

The authors would like to thank the staff at the Siriraj Breast Imaging Center for their assistance in data collection and procedure coordination. We also acknowledge the support from the Department of Radiology, Faculty of Medicine Siriraj Hospital for facilitating this retrospective review.

Ethic

This retrospective study was approved by the Siriraj Institutional Review Board (SiRB), Faculty of Medicine Siriraj Hospital, Mahidol University. The requirement for informed consent was waived due to the retrospective nature of the study and anonymization of patient data.

References

1. Bae S, Yoon JH, Moon HJ, Kim MJ, Kim E-K. Breast microcalcifications: diagnostic outcomes according to image-guided biopsy method. Korean J Radiol. 2015;16(5): 996.

2. Huang XC, Hu XH, Wang XR, Zhou CX, Wang FF, Yang S, et al. A comparison of diagnostic performance of vacuum-assisted biopsy and core needle biopsy for breast microcalcification: a systematic review and meta-analysis. Ir J Med Sci. 2018; 187:999-1008.

3. Soo MS, Baker JA, Rosen EL. Sonographic detection and sonographically guided biopsy of breast microcalcifications. AJR Am J Roentgenol. 2003;180(4):941-8.

4. Kettritz U, Rotter K, Schreer I, Murauer M, Schulz-Wendtland R, Peter D, et al. Stereotactic vacuum-assisted breast biopsy in 2874 patients: a multicenter study. Cancer. 2004;100(2):245-51.

5. Yi J, Lee EH, Kwak JJ, Cha JG, Jung SH. Retrieval rate and accuracy of ultrasound-guided 14-G semi-automated core needle biopsy of breast microcalcifications. Korean J Radiol. 2014;15(1):12-9.

6. Liberman L, Smolkin JH, Dershaw DD, Morris EA, Abramson AF, Rosen PP. Calcification retrieval at stereotactic, 11-gauge, directional, vacuum-assisted breast biopsy. Radiology. 1998;208(1):251-60.

7. Jackman RJ, Marzoni Jr FA, Rosenberg J. False-negative diagnoses at stereotactic vacuum-assisted needle breast biopsy: long-term follow-up of 1,280 lesions and review of the literature. AJR Am J Roentgenol. 2009;192(2):341-51.

8. Popat PBT, Karbhari A, Shetty N, Gala K, Haria P, Katdare A, et al. Safety and Efficacy of Vacuum-Assisted Breast Biopsies under Ultrasound and Stereotactic Guidance. J Clin Interv Radiol ISVIR. 2023;7(03):172-8.

9. Youk JH, Kim E-K, Kim MJ, Kwak JY, Son EJ. Analysis of false-negative results after US-guided 14-gauge core needle breast biopsy. Eur Radiol. 2010;20:782-9.

10. Bagnall M, Evans A, Wilson A, Burrell H, Pinder S, Ellis I. When have mammographic calcifications been adequately sampled at needle core biopsy? Clin Radiol. 2000;55(7):548-53.

11. Margolin FR, Kaufman L, Jacobs RP, Denny SR, Schrumpf JD. Stereotactic core breast biopsy of malignant calcifications: diagnostic yield of cores with and cores without calcifications on specimen radiographs. Radiology. 2004;233(1):251-4.

12. Shrestha A, Wilkinson L, Given-Wilson R, Curtis J. Quantitative study: should vacuum-assisted biopsy be the first biopsy approach in breast interventional techniques in stereotactic guided microcalcifications rather than 14 gauge core needle biopsy? Breast Cancer Res. 2015;17(Suppl 1):P29.

13. Kim HS, Kim MJ, Kim E-K, Kwak JY, Son EJ, Oh KK. US-guided vacuum-assisted biopsy of microcalcifications in breast lesions and long-term follow-up results. Korean J Radiol. 2008;9(6):503-9.

14. Cho N, Moon WK, Cha JH, Kim SM, Jang M, Chang JM, et al. Ultrasound-guided vacuum-assisted biopsy of microcalcifications detected at screening mammography. Acta Radiol. 2009;50(6):602-9.

15. Hahn SY, Shin JH, Han B-K, Ko EY. Sonographically-guided vacuum-assisted biopsy with digital mammography-guided skin marking of suspicious breast microcalcifications: comparison of outcomes with stereotactic biopsy in Asian women. Acta Radiol. 2011;52(1):29-34.

16. D'Orsi CJ, Sickles EA, Mendelson EB, Morris EA. ACR BI-RADS® Atlas, Breast Imaging Reporting and Data System. Reston, VA: American College of Radiology; 2013.

Original Article

Radiomics-based texture and shape analysis to differentiate between lipoma and liposarcoma on magnetic resonance imaging

Chitsanucha Pantawee, M.D.[1, 2]
Jaravee Lasode, M.Sc.[1]
Yothin Rakvongthai, Ph.D.[3, 4]
Jindarat Ratanakornphan, M.D.[2]
Aticha Ariayachaipanich, M.D.[1, 2]
From [1]Division of Diagnostic Imaging, [3]Chulalongkorn University Biomedical Imaging Group, [4]Division of Nuclear Medicine, Department of Radiology, Faculty of Medicine, Chulalongkorn University, Bangkok, Thailand,
[2]Department of Radiology, King Chulalongkorn Memorial Hospital, Bangkok, Thailand.
Address correspondence to A.A (email: Aticha.a@chulahospital.org)

Received 21 September 2025; revised 23 April 2026; accepted 26 April 2026
doi:10.46475/asean-jr.v27i2.987

Abstract

Objective: This retrospective study aimed to assess the utility of magnetic resonance texture and shape analysis (MRTA) in enhancing the diagnostic accuracy of lipoma and liposarcoma differentiation on preoperative magnetic resonance imaging (MRI).

Materials and Methods: A total of 89 cases with pathologically confirmed lipoma or liposarcoma that underwent MRI before surgery at King Chulalongkorn Memorial Hospital between January 2010 and December 2022, were retrospectively included in this IRB-approved study. Axial T1-weighted (T1WI) and axial T1-weighted fat-saturated post-contrast (T1WI FS Gd) images were processed and segmented using the 3D Slicer program. Feature extraction was performed using PyRadiomics. Models were trained and internally validated using 5-fold stratified cross-validation and diagnostic accuracy was compared between MRTA and a musculoskeletal radiologist.

Results: Among 89 lesions (51 lipomas, 38 liposarcomas), MRTA demonstrated a sensitivity and specificity of 74.6% and 94.7%, respectively, on T1WI, and 77.6% and 97.4%, respectively, on T1WI FS Gd. MRTA demonstrated comparable or incrementally improved diagnostic performance compared with radiologist interpretation.

THE ASEAN JOURNAL OF RADIOLOGY
ISSN 2672-9393

Conclusion: MRTA can effectively differentiate lipoma from liposarcoma, with higher sensitivity and specificity than visual radiological assessment. Segmentation on both T1WI and T1WI FS Gd sequences showed that contrast-enhanced fat-suppressed imaging provides superior diagnostic performance by more effectively highlighting enhancing septa and non-lipomatous components.

Keywords: Atypical lipomatous tumor, Lipoma, Liposarcoma, Radiomics, Shape analysis, Texture analysis.

Introduction

Lipomatous soft tissue tumors are the most common mesenchymal neoplasms, ranging from benign to aggressive malignant tumors [1]. Lipoma is a common benign subcutaneous tumor composed of adipose tissue that typically grows slowly. Liposarcoma is among the most prevalent soft tissue sarcomas (STS), accounting for approximately 50% of retroperitoneal and 25% of extremity STS [2]. Liposarcomas are usually managed with surgery and may require adjuvant therapy [3,4] while lipomas often require no treatment unless symptomatic. Accurate diagnosis is therefore essential to guide appropriate treatment and follow-up management.

Magnetic resonance imaging (MRI) is the standard modality for evaluating lipomatous tumors [5]. Several MRI features including tumor size, location, presence of thick septa or enhancement, have been proposed as diagnostic indicators. However, substantial overlap exists between lipomas and liposarcomas [6]. Visual assessment of texture by radiologists remains subjective, leading to a risk of misinterpretation as well as inter- and intra-observer variability [7]. Computer-assisted diagnosis (CAD) has been shown to slightly improve sensitivity, specificity, and accuracy in differentiating liposarcoma from lipoma [8,9].

Radiomic-based texture analysis has emerged as a potential CAD tool for extracting clinically relevant information from tissue heterogeneity within the region of interest (ROI) on conventional imaging, beyond what is perceptible to the human eye. A growing body of research demonstrated that radiomic features can assist in lesion detection, classification, treatment response evaluation, and prognosis prediction in musculoskeletal soft tissue tumors. Magnetic resonance texture analysis (MRTA) has therefore gained attention as a promising adjunct in diagnosing lipomatous tumors. However, existing radiomics studies in lipomatous tumors have several important limitations. These include heterogeneous imaging protocols, variable segmentation strategies (single-slice or two-dimensional analysis versus whole-volume segmentation), incon-

sistent incorporation of contrast-enhanced fat-suppressed sequences, and limited direct comparison with expert musculoskeletal radiologist interpretation. Such methodological variability hinders reproducibility and limits clinical translation. Accordingly, there remains a need for radiomics studies that employ standardized, clinically relevant workflows using routinely acquired MRI sequences.

Therefore, the aim of this study was to develop and internally validate a magnetic resonance texture and shape analysis (MRTA) model using axial T1-weighted imaging (T1WI) and fat-suppressed post-contrast T1-weighted imaging (T1WI FS Gd) to differentiate lipoma from liposarcoma. In addition, we sought to directly compare radiomics-based model performance with that of an experienced musculoskeletal radiologist in a clinically representative setting.

Materials and methods

This retrospective study was approved by the Institutional Review Board (IRB) of our institute, with a waiver of informed consent due to its retrospective design and anonymized data (IRB No. 0540/65). We included patients with pathologically confirmed lipoma or liposarcoma who underwent MRI before surgery at King Chulalongkorn Memorial Hospital between January 2010 and December 2022.

Inclusion criteria were:

- Age >10 years with a lipomatous tumor of the trunk or extremities. Trunk lesions were defined as tumors arising from the chest wall, abdominal wall or back, and did not include mediastinal or retroperitoneal tumors.
- MRI performed prior to surgery with a protocol including axial T1-weighted imaging (T1WI), at least one plane of T2-weighted imaging with fat suppression or short tau inversion recovery (STIR), and axial T1WI with fat suppression and gadolinium contrast (T1WI FS Gd).
- Complete surgical excision of the mass.
- Histopathological confirmation of lipoma or liposarcoma.

Exclusion criteria were:

- Patients who underwent biopsy prior to MRI.
- Recurrent tumors.
- Poor-quality MRI images.
  Based on these criteria, a total of 86 patients with 89 lesions were included. Demographic and clinical data, and histopathological results, were obtained from electronic medical records (EMRs).

MRI acquisition

As a tertiary referral hospital, some patients were referred from outside institutions, resulting in variability in MRI scanners and protocols. All examinations were performed using 1.5- or 3.0-Tesla MRI systems.

For most cases, the slice thickness, repetition time (TR), and echo time (TE) were consistent across T1WI and T1WI FS Gd sequences, except for one lesion acquired using a gradient-echo sequence on post-contrast imaging. The median slice thickness was 5.5 mm (range 2.5–8 mm). The median TR was 626 ms (range 420–817 ms for T1WI and 495–817 ms for T1WI FS Gd). The median TE was 12 ms (range 6.0–20.8 ms for T1WI and 6.0–20.8 ms for T1WI FS Gd).

Segmentation

Manual segmentation of all lipomatous tumors was performed using the open-source software 3D Slicer (version 5.5.2; http://download.slicer.org). For each case, regions of interest (ROIs) encompassing the entire tumor volume were delineated on axial T1WI and axial T1WI FS Gd sequences. In all cases, segmentation was performed by a third-year radiology resident and used for feature extraction.

To evaluate interobserver variability, 30 cases (17 lipomas and 13 liposarcomas) were randomly selected and segmented independently by two additional observers (musculoskeletal radiologists with 10 and 11 years of experience, respectively), blinded to pathology and clinical data. Interobserver agreement was assessed using intraclass correlation coefficients (ICCs).

Feature extraction and selection

The segmented ROIs and original MRI images were exported into Python (version 3.9) and processed using the open-source PyRadiomics package (version 3.0.1) [10]. Images were normalized to reduce signal intensity variability. Texture-based, shape-based, and first-order statistical features were extracted from both T1WI and T1WI FS Gd sequences (105 radiomic features per sequence).

To ensure feature stability, intraclass correlation coefficient (ICC) analysis was performed at thresholds of 0.90, 0.95, and 0.99. Subsequently, recursive feature elimination with cross-validation (RFECV) was applied using L2-penalized logistic regression to identify the most informative features. Five-fold stratified cross-validation was performed with the StratifiedKFold function (scikit-learn in Python), maintaining a training-to-validation ratio of 4:1.

Model creation

All selected features from T1WI, T1WI FS Gd and combined sequences (SEs) were used to develop diagnostic models to differentiate lipoma from liposarcoma. We trained multivariate logistic regression classifiers implemented in scikit-learn. Because the proposed approach is a classical machine-learning model using radiomic features, no data augmentation was applied.

Model training and evaluation were performed using 5-fold stratified cross-validation (StratifiedKFold; n_splits = 5, shuffle = True, random_state = 9559), maintaining a training-to-validation ratio of 4:1 in each split. Hyperparameter tuning was performed using GridSearchCV to select the best-performing individual and combined feature sets based on the mean cross-validated AUC. We evaluated L1 (Lasso) and L2 (Ridge) regularization with an inverse regularization strength C in the range 0.0001–100. Optimization was performed using the scikit-learn logistic regression solver (solver = liblinear) with a maximum number of iterations (max_iter = 10000). Training terminated upon solver convergence (default tolerance in scikit-learn) or reaching the maximum iterations (i.e., no separate early-stopping rule was used). Model parameters were initialized using the scikit-learn default setting (no manual initialization). An overview of the radiomics workflow, including segmentation, preprocessing, feature extraction, feature selection, and model training/validation, is summarized in Figure 1.

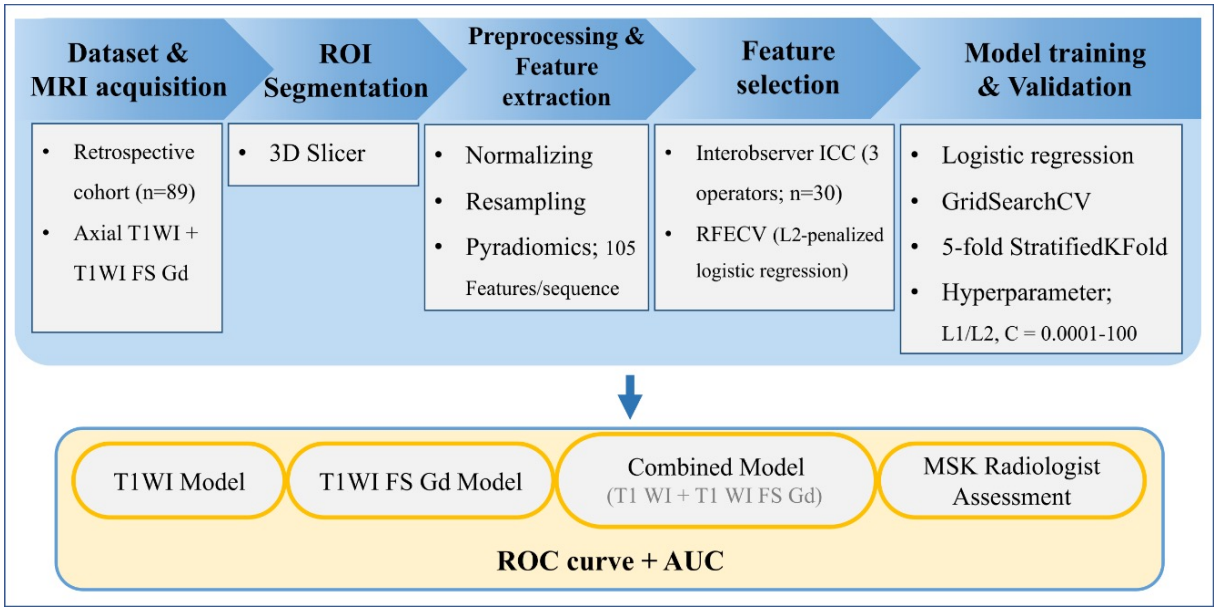

Figure 1. *Study workflow and radiomics pipeline. The flowchart summarizes segmentation, preprocessing, feature extraction, feature selection (interobserver ICC and RFECV), and model training and validation for T1WI, T1WI FS Gd, and combined models, with performance reported as ROC curves and AUC values.*

THE ASEAN JOURNAL OF RADIOLOGY
ISSN 2672-9393

Radiologist diagnosis assessment

An experienced musculoskeletal (MSK) radiologist with 10 years of practice, blinded to clinical and pathological information, independently classified each tumor as either lipoma or liposarcoma. Image interpretation was performed using the Picture Archiving and Communication System (PACS) with Synapse software (Version 5, Fujifilm Global, Japan). For each case, the radiologist reviewed all available MRI sequences, which typically included axial T1WI, at least one plane of T2 FS or STIR, and axial T1WI FS Gd, in accordance with routine clinical practice at our institution. No radiomic features or quantitative outputs were available to the radiologist during interpretation.

Radiological diagnosis was based on established MRI features described in prior studies [11-16]. Lipoma was favored when lesions showed homogeneous fat signal intensity with thin internal septa, complete fat suppression, and no nodular or abnormal enhancement. Atypical lipomatous tumor (ALT) was suspected in predominantly fatty lesions demonstrating atypical features such as a few thickened septa (≥2 mm), focal or septal enhancement, or subtle areas of non-lipomatous components. High-grade liposarcoma was diagnosed when lesions exhibited more aggressive characteristics, including nodular non-lipomatous areas, thick irregular enhancing septa, and heterogeneous internal architecture. For descriptive purposes, radiologists recorded impressions as lipoma, ALT, or high-grade liposarcoma; however, all quantitative analyses were performed using a binary classification of lipoma versus liposarcoma. In addition to classification, the radiologist recorded the tumor depth (superficial, deep, or involving both compartments) and measured the maximum tumor dimension.

Histopathological diagnosis

Histopathological diagnosis, which served as the reference standard, was based primarily on routine morphologic evaluation by experienced musculoskeletal pathologists. Ancillary testing was performed selectively in cases with equivocal histologic features: MDM2 amplification analysis was used to support the diagnosis of atypical lipomatous tumor and was concordant with the final diagnosis in all tested cases, and CDK4 immunohistochemistry was performed in two cases as supportive evidence.

Statistical analysis

All statistical analyses were performed using STATA software (version 18). A two-sided p-value < 0.05 was considered statistically significant. Comparisons of patient demographics and imaging features were conducted using the non-parametric Mann–Whitney test. Interobserver variability of manual segmentation was assessed using intraclass correlation coefficients (ICCs) to evaluate reproducibility between the radiology resident and the two musculoskeletal radiologists.

Diagnostic performance of the computer-assisted models was assessed using the area under the receiver operating characteristic curve (AUC), true positive rate (TPR), and false positive rate (FPR). Sensitivity and specificity were determined using Youden's index derived from the receiver operating characteristics (ROC) analysis of the multivariate logistic regression models. For the radiologist, diagnostic performance was based on a single binary classification per lesion. Sensitivity and specificity were calculated, and the corresponding operating point was plotted in ROC space for comparison with MRTA models. Statistical analyses and performance graphs were generated using Python.

Results

A total of 86 patients with 89 lipomatous lesions were included in the analysis: 51 lipomas and 38 liposarcomas (18 atypical lipomatous tumors [ALTs] and 20 other histologic subtypes of liposarcoma), as shown in Table 1.

Table 1. *Histopathological classification of lipomatous tumors, with atypical lipomatous tumors included in the liposarcoma group. MDM2 amplification testing was performed selectively.*

Lipoma (N=51)	Liposarcoma (N=38)

• Lipoma, not otherwise specified (NOS) (n = 46)*
• Osteochondrolipoma (n = 2)
• Spindle cell lipoma (n = 1) *
• Lipoma with focal myxoid change (n = 2) *
	• Atypical lipomatous tumor (ALT) (n = 18) *
	• High-grade liposarcoma (n = 20)
	  • Dedifferentiated liposarcoma (n = 14)
	  • Myxoid/round cell liposarcoma (n = 4)
	  • Mixed-type liposarcoma (n = 2)

Note * MDM2 amplification testing was performed in selected cases with equivocal histopathologic features; all tested ALT cases (n=12) showed positive MDM2 amplification, whereas all tested lipoma cases (n=15) were negative.	

The mean patient age was 58.7 years (range, 10–83 years). Most lesions occurred in women (52.3%), were located in deep compartments (73%), and most commonly involved the lower extremities (41.6%). The mean maximum diameter of lipomas was 7.6 cm, compared with 14.1 cm for liposarcomas. There were no statistically significant differences between the lipoma and liposarcoma groups with respect to age, sex, tumor depth, or maximum diameter. In contrast, tumor location differed significantly between groups ($p < 0.01$), with liposarcomas occurring more frequently in the lower extremities, whereas lipomas were more commonly located in the upper extremities and trunk. The clinical and demographic characteristics of the study population are summarized in Table 2.

Table 2. *The clinical and demographic characteristics of the patients.*

	All (N=89)	Lipoma (N=51)	Liposarcoma (N=38)	p value
Age (years), mean ± SD	58.7 ± 13.3	56.7	56.6	0.74
Gender				0.40
Male, n (%)	43 (47.7)	25 (49.0)	18 (47.3)	
Female, n (%)	46 (52.3)	26 (51.0)	20 (52.7)	
Anatomical region				<0.001
Upper extremity, n (%)	29 (32.6)	22 (43.1)	7 (18.4)	
Lower extremity, n (%)	37 (41.6)	9 (17.7)	28 (73.6)	
Trunk, n (%)	23 (25.8)	20 (39.2)	3 (8.0)	
Tumor depth				0.28
Superficial, n (%)	20 (22.5)	18 (35.2)	2 (5.3)	
Deep, n (%)	65 (73.0)	30 (58.8)	35 (92.1)	
Both, n (%)	4 (4.5)	3 (6.0)	1 (2.6)	
Longest diameter (centimeters), mean ± SD	10.4 ± 5.5	7.6 ± 3.9	14.1 ± 5.2	0.79

Diagnostic Performance of Radiomics Models

The diagnostic performance of radiomics models was evaluated using multivariate logistic regression analyses across T1WI, T1WI FS Gd, and combined sequences, at different intraclass correlation coefficient (ICC) thresholds (0.90, 0.95, and 0.99). On T1WI, the mean training AUC was 0.91 (SD 0.015), with the mean validation AUCs of 0.89 (SD 0.068). On T1WI FS Gd, the multivariate models achieved the best performance, with a mean training AUCs of 0.94 (SD 0.016) and a mean validation AUCs of 0.94 (SD 0.068). When both sequences were combined, the mean training AUC was 0.964 (SD 0.012) and the mean validation AUC was 0.93 (SD 0.044).

Overall, the T1WI FS Gd multivariate model provided the highest and most consistent diagnostic performance, while the combined model showed comparable performance and the T1WI model achieved slightly lower but still good discrimination.

The three most informative features identified in the multivariate analysis were:
For T1WI: maximum 3D diameter, median first-order intensity, and small dependence high gray-level emphasis.

For T1WI FS Gd: size zone non-uniformity, maximum 3D diameter, and first-order10th percentile intensity.

A comparison of diagnostic performance between the MRTA and an experienced MSK radiologist in multivariate logistic regression model for T1WI, T1WI FS GD and combined. The radiologist provided a single binary interpretation using all available MRI sequences, therefore, the operating point is identical across panels. Visually, the MRTA demonstrated comparable or higher discrimination than the radiologist operating point in ROC space (Figure 2).

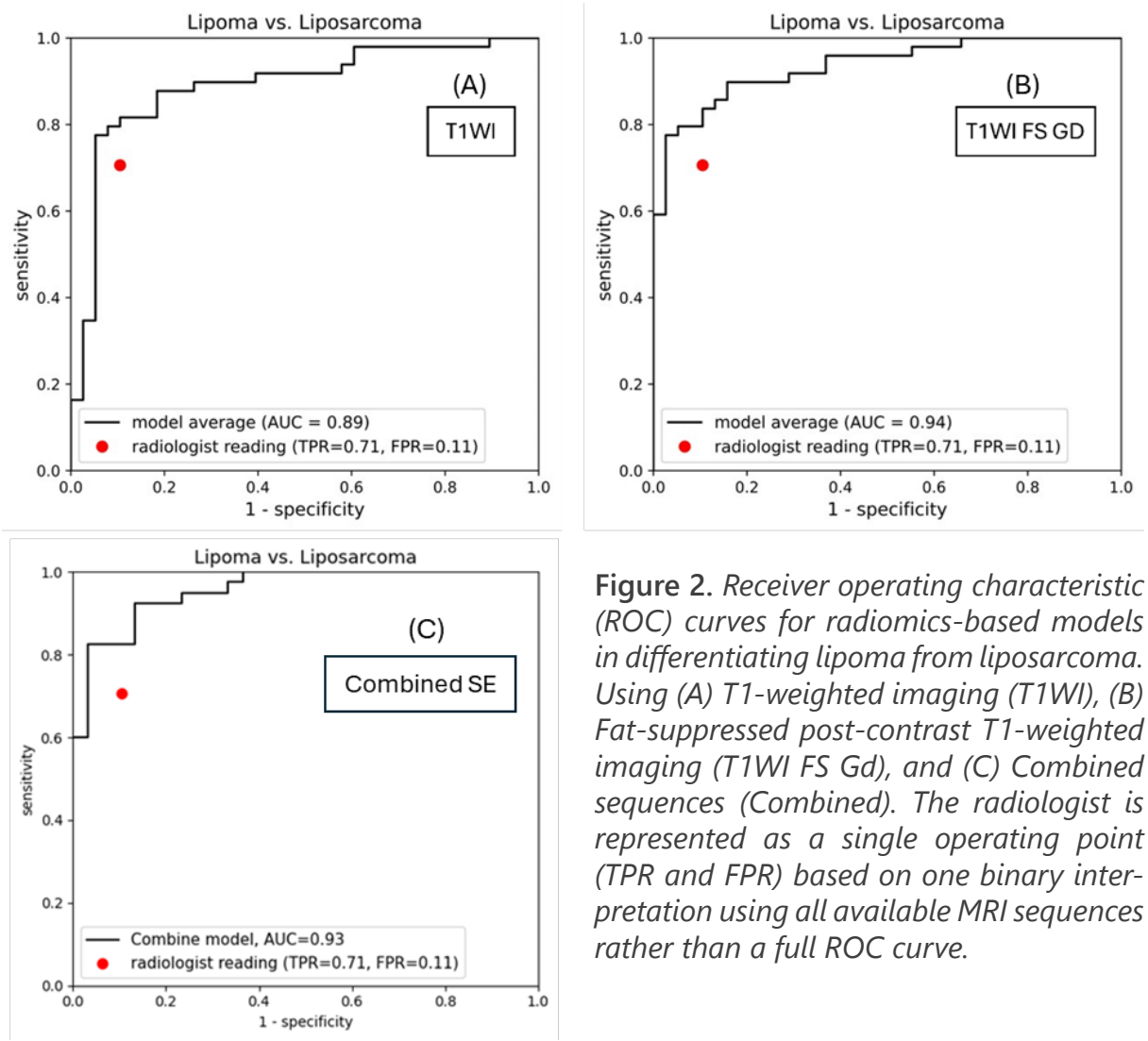

Figure 2. *Receiver operating characteristic (ROC) curves for radiomics-based models in differentiating lipoma from liposarcoma. Using (A) T1-weighted imaging (T1WI), (B) Fat-suppressed post-contrast T1-weighted imaging (T1WI FS Gd), and (C) Combined sequences (Combined). The radiologist is represented as a single operating point (TPR and FPR) based on one binary interpretation using all available MRI sequences rather than a full ROC curve.*

The sensitivity and specificity were calculated using Youden's index derived from receiver operating characteristic (ROC) analysis of the multivariate logistic regression models. On T1WI, MRTA achieved a sensitivity of 74.6% and specificity of 94.7%. On T1WI FS Gd, performance improved further, with a sensitivity of 77.6% and specificity of 97.4%. On combined sequences, MRTA achieved a sensitivity of 85.7% and specificity of 86.8%. The radiologist's operating point lies below the ROC curve of the MRTA model, indicating lower overall discrimination compared with the radiomics-based approach. The radiologist diagnostic performance was a sensitivity of 71% and specificity of 91%

The number of correctly classified and misclassified cases for lipoma, atypical lipomatous tumor (well-differentiated liposarcoma), and other liposarcoma subgroups, as diagnosed by the radiologist, the T1WI multivariate model, and the T1WI FS Gd multivariate model (using Youden's index as the cutoff from ROC analysis), are summarized in Table 3.

Table 3. *Diagnostic performance of radiologist versus MRTA multivariate models in differentiating lipoma, atypical lipomatous tumor, and other liposarcomas. Values represent the number of correctly classified cases (Correct) and misclassified cases (Miss) for each method.*

Diagnosis / Pathology (n)	Radiologist		MRTA on T1WI		MRTA on T1WI FS Gd	
	Correct (n)	Miss (n)	Correct (n)	Miss (n)	Correct (n)	Miss (n)
Lipoma (51)	37	14	41	10	42	9
Atypical lipomatous tumor (18)	14	4	16	2	16	2
Other types of liposarcoma (20)	20	0	20	0	19	1

In the atypical lipomatous tumor and other liposarcoma subgroups, no lesion was misclassified simultaneously by all three methods (radiologist, T1WI multivariate model, and T1WI FS Gd multivariate model).

Notable examples of misclassified cases by the radiologist, MRTA, or both methods are illustrated in Figures 3-6.

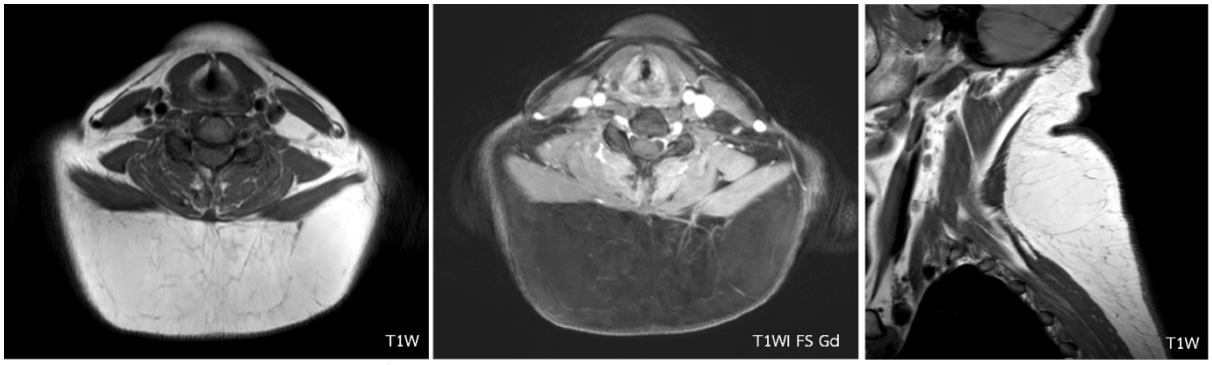

Figure 3. *A neck mass in a 30-year-old woman, diagnosed as subcutaneous lipoma by the radiologist but classified as liposarcoma by both the T1WI and T1WI FS Gd multivariate models. Histopathology confirmed an atypical lipomatous tumor (well-differentiated liposarcoma).*

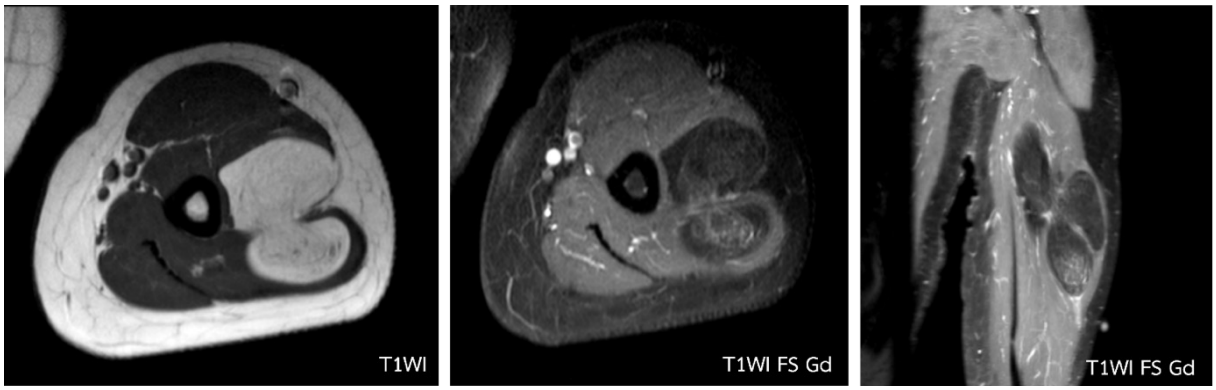

Figure 4. *An arm mass in a 46-year-old woman, diagnosed as liposarcoma by the radiologist and T1WI model, classified as lipoma by the T1WI FS Gd model. Histopathology confirmed an atypical lipomatous tumor.*

Figure 5. *A shoulder mass in a 50-year-old woman, diagnosed as lipoma with intralesional muscle fibers (arrow) by the radiologist and T1WI FS Gd model, classified as liposarcoma by the T1WI model. Histopathology confirmed a lipoma.*

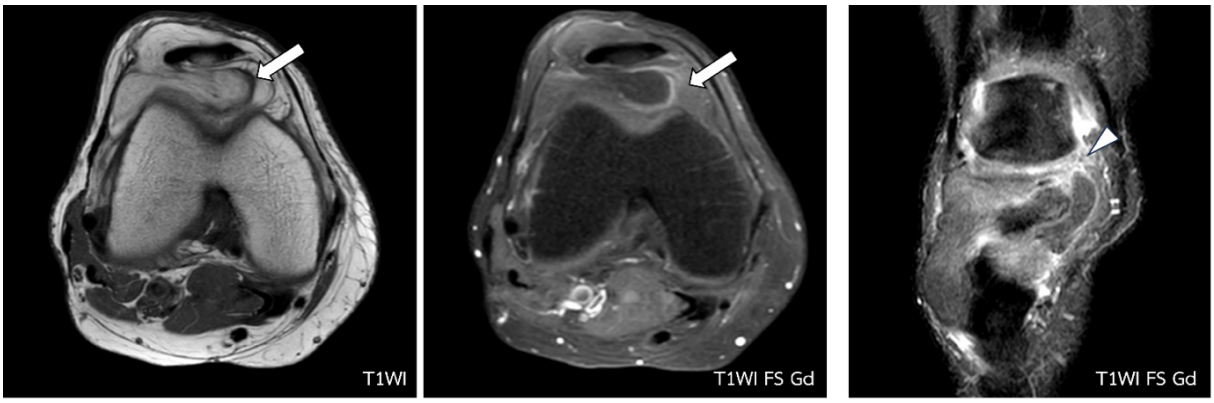

Figure 6. *An anterior knee mass in a 59-year-old woman with thick enhanced internal septation (arrow) and an area of patchy enhancement (arrowhead). The radiologist, T1WI, and T1WI FS Gd models all diagnosed liposarcoma; however, histopathology confirmed a lipoma.*

Discussion

Differentiating lipoma from liposarcoma remains a common and clinically important challenge in musculoskeletal imaging. Conventional MRI features—such as lesion size, internal septation, and enhancement patterns—are helpful but often overlap between benign lipomas and malignant liposarcomas, particularly atypical lipomatous tumors [12-16]. In recent years, radiomics-based approaches have shown promise in improving diagnostic accuracy; however, prior studies have been limited by heterogeneous imaging protocols, two-dimensional or single-slice segmentation, lack of comparison with expert radiologists, and inconsistent use of contrast-enhanced imaging [8-10,17-19]. The strength of the present study lies in its clinically oriented design, combining whole-volume radiomics analysis of routine MRI sequences with direct comparison to an experienced musculoskeletal radiologist. By evaluating both non-contrast T1-weighted and fat-suppressed contrast-enhanced sequences within a standardized workflow, this study addresses key knowledge gaps highlighted in recent reviews and provides new insight into the incremental value of radiomics in routine clinical practice.

According to our results, the radiologist achieved a sensitivity of 71% and specificity of 91%. In comparison, MRTA demonstrated higher performance, with sensitivity and specificity of 74.6% and 94.7% on T1WI, 77.6% and 97.4% on T1WI FS Gd, and 85.7% and 86.8% in the combined model, respectively. These findings suggest that radiomics-based texture and shape analysis may enhance diagnostic efficacy and reduce the risk of misinterpretation. Importantly, in the atypical lipomatous tumor and other liposarcoma subgroups, no lesion was misclassified simultaneously by all three methods (radiologist, T1WI multivariate model, and T1WI FS Gd multivariate model), underscoring the complementary value of MRTA in clinical decision-making.

Beyond overall performance, the selected radiomic features may provide insight into imaging characteristics that may discriminate between benign and malignant lipomatous tumors. For T1WI model, the most informative features (maximum 3D diameter, first-order median intensity, and small dependence high gray-level emphasis) reflect lesion size, signal distribution, and fine-scale texture. For T1WI FS Gd, key features (size zone non-uniformity, maximum 3D diameter, and first-order 10th percentile intensity) highlight post-contrast heterogeneity, which may reflect a more complex internal structure, such as enhancing septa and non-fatty components. Size related features were consistently incorporated into the models, indicating that tumor size contributes meaningfully to malignancy prediction in lipomatous tumors, in line with conventional imaging-based literature [20-22]. In addition, texture features — specifically GLDM- and GLSZM-derived non-uniformity metrics and First-order intensity descriptors were

also retained, suggesting that the pattern of enhancement heterogeneity and internal complexity, rather than enhancement intensity alone, is important for distinguishing benign from malignant lipomatous tumors [18,23]. Together, these findings suggest that radiomics quantitatively captures subtle heterogeneity and internal complexity that may be underappreciated by visual assessment, providing biological plausibility for the observed diagnostic benefit.

Our findings are consistent with and extend prior radiomics studies of lipomatous tumor. Earlier work demonstrated that MRI-based texture and shape analysis and demonstrated improved differentiation between lipoma and liposarcoma [9] and subsequent studies reported high diagnostic accuracy using radiomics derived from contrast T1WI [18,19]. Most recently, Haidey et al. (2023) have systematically reviewed and highlighted the overall promise of radiomics while emphasizing substantial methodological heterogeneity and limited clinical validation [17]. In contrast to many prior studies, the present work applies whole-volume segmentation, evaluates routinely acquired MRI sequences, and directly benchmarks radiomics performance against expert musculoskeletal radiologist interpretation. While large multicenter deep-learning approaches have demonstrated scalability and external validation [21], our manual whole-volume approach provides complementary insight into the specific contribution of contrast-enhanced fat-suppressed imaging and interpretable radiomic features in everyday clinical practice.

Taken together, our findings reinforce the potential of MRTA to improve diagnostic accuracy for lipomatous tumors, especially when applied to contrast-enhanced FS sequences. However, the variability in ROI methodology across studies underscores the need for standardized segmentation protocols. Larger multicenter studies, ideally incorporating automated segmentation approaches similar to those reported by Spaanderman et al. [24], will be essential to validate and generalize these results.

Conclusion

This study demonstrated that magnetic resonance texture and shape analysis (MRTA) can effectively differentiate lipoma from liposarcoma, with higher sensitivity and specificity than visual radiological assessment. Segmentation on both T1WI and T1WI FS Gd sequences showed that contrast-enhanced fat-suppressed imaging provides superior diagnostic performance by better highlighting enhancing septa and non-lipomatous components.

Our findings support MRTA as a promising adjunct to radiologist interpretation, helping to reduce diagnostic uncertainty and misclassification, particularly in challenging cases. Future multicenter studies with larger cohorts, standardized segmentation protocols, and external validation—ideally incorporating automated or semi-automated workflows—will be essential to further validate and generalize these findings.

Conflict of interest

None declared.

References

1. Johnson CN, Ha AS, Chen E, Davidson D. Lipomatous soft-tissue tumors. J Am Acad Orthop Surg 2018;26:779–88. doi: 10.5435/JAAOS-D-17-00045.

2. Crago AM, Dickson MA. Liposarcoma: Multimodality management and future targeted therapies. Surg Oncol Clin N Am 2016;25:761–73. doi: 10.1016/j.soc.2016.05.007.

3. Gronchi A, Miah AB, Dei Tos AP, Abecassis N, Bajpai J, Bauer S, et al. Soft tissue and visceral sarcomas: ESMO-EURACAN-GENTURIS clinical practice guidelines for diagnosis, treatment and follow-up. Ann Oncol 2021;32:1348–65. doi: 10.1016/j.annonc.2021.07.006.

4. Mullen JT, Kobayashi W, Wang JJ, Harmon DC, Choy E, Hornicek FJ, et al. Long-term follow-up of patients treated with neoadjuvant chemotherapy and radiotherapy for large, extremity soft tissue sarcomas. Cancer 2012;118:3758–65. doi: 10.1002/cncr.26696.

5. Sommerville SM, Patton JT, Luscombe JC, Mangham DC, Grimer RJ. Clinical outcomes of deep atypical lipomas (well-differentiated lipoma-like liposarcomas) of the extremities. ANZ J Surg 2005;75:803–6. doi: 10.1111/j.1445-2197.2005.03519.x.

6. Billing V, Mertens F, Domanski HA, Rydholm A. Deep-seated ordinary and atypical lipomas: histopathology, cytogenetics, clinical features, and outcome in 215 tumours of the extremity and trunk wall. J Bone Joint Surg Br 2008;90:929–33. doi: 10.1302/0301-620X.90B7.20348.

7. O'Donnell PW, Griffin AM, Eward WC, Sternheim A, White LM, Wunder JS, et al. Can experienced observers differentiate between lipoma and well-differentiated liposarcoma using only MRI? Sarcoma 2013;2013:982784. doi: 10.1155/2013/982784.

8. Juntu J, Sijbers J, De Backer S, Rajan J, Van Dyck D. Machine learning study of several classifiers trained with texture analysis features to differentiate benign from malignant soft-tissue tumors in T1-MRI images. J Magn Reson Imaging 2010;31:680–9. doi: 10.1002/jmri.22095.

9. Thornhill RE, Golfam M, Sheikh A, Cron GO, White EA, Werier J, et al. Differentiation of lipoma from liposarcoma on MRI using texture and shape analysis. Acad Radiol 2014;21:1185–94. doi: 10.1002/jmri.22095.

10. van Griethuysen JJM, Fedorov A, Parmar C, Hosny A, Aucoin N, Narayan V, et al. Computational Radiomics System to Decode the Radiographic Phenotype. Cancer Res 2017;77:e104–7. doi: 10.1158/0008-5472.CAN-17-0339.

11. Chernev I, Petit-Clair N. Magnetic resonance imaging characteristics of intramuscular lipomas. Sao Paulo Med J 2015;133:64–6. doi: 10.1590/1516-3180.2014.86200716.

12. Doyle AJ, Pang AK, Miller MV, French JG. Magnetic resonance imaging of lipoma and atypical lipomatous tumour/well-differentiated liposarcoma: observer performance using T1-weighted and fluid-sensitive MRI. J Med Imaging Radiat Oncol 2008;52:44–8. doi: 10.1111/j.1440-1673.2007.01910.x.

13. Gupta P, Potti TA, Wuertzer SD, Lenchik L, Pacholke DA. Spectrum of fat-containing soft-tissue masses at MR imaging: The common, the uncommon, the characteristic, and the sometimes confusing. Radiographics 2016;36:753–66. doi: 10.1148/rg.2016150133.

14. Knebel C, Neumann J, Schwaiger BJ, Karampinos DC, Pfeiffer D, Specht K, et al. Differentiating atypical lipomatous tumors from lipomas with magnetic resonance imaging: A comparison with MDM2 gene amplification status. BMC Cancer 2019;19:309. doi: 10.1186/s12885-019-5524-5.

15. Kransdorf MJ, Bancroft LW, Peterson JJ, Murphey MD, Foster WC, Temple HT. Imaging of fatty tumors: distinction of lipoma and well-differentiated liposarcoma. Radiology 2002;224:99–104. doi: 10.1148/radiol.2241011113.

16. Muhib M, Abidi SLF, Ahmed U, Afzal A, Farooqui A, Khalid Jamil OB, et al. Use of radiologic imaging to differentiate lipoma from atypical lipomatous tumor/well-differentiated liposarcoma: Systematic review. SAGE Open Med 2024;12:20503121241293496. doi: 10.1177/20503121241293496.

17. Haidey J, Low G, Wilson MP. Radiomics-based approaches outperform visual analysis for differentiating lipoma from atypical lipomatous tumors: a review. Skeletal Radiol 2023;52(:1089–100. doi: 10.1007/s00256-022-04232-0.

18. Leporq B, Bouhamama A, Pilleul F, Lame F, Bihane C, Sdika M, et al. MRI-based radiomics to predict lipomatous soft tissue tumors malignancy: a pilot study. Cancer Imaging 2020;20:78. doi: 10.1186/s40644-020-00354-7.

19. Pressney I, Khoo M, Endozo R, Ganeshan B, O'Donnell P. Pilot study to differentiate lipoma from atypical lipomatous tumour/well-differentiated liposarcoma using MR radiomics-based texture analysis. Skeletal Radiol 2020;49:1719–29. doi: 10.1007/s00256-020-03454-4.

20. Coran A, Ortolan P, Attar S, Alberioli E, Perissinotto E, Tosi AL, et al. Magnetic resonance imaging assessment of lipomatous soft-tissue tumors. In Vivo 2017; 31:387–95. doi: 10.21873/invivo.11071.

21. Datir A, James SL, Ali K, Lee J, Ahmad M, Saifuddin A. MRI of soft-tissue masses: The relationship between lesion size, depth, and diagnosis. Clin Radiol 2008;63:373–8; discussion 379–80. doi: 10.1016/j.crad.2007.08.016.

22. El Ouni F, Jemni H, Trabelsi A, Ben Maitig M, Arifa N, Ben Rhouma K, et al. Liposarcoma of the extremities: MR imaging features and their correlation with pathologic data. Orthop Traumatol Surg Res 2010;96:876–83. doi: 10.1016/j.otsr.2010.05.010.

23. Wang S, Chan LW, Tang X, Su C, Zhang C, Sun K, et al. A weighted scoring system to differentiate malignant liposarcomas from benign lipomas. J Orthop Surg (Hong Kong) 2016;24:216–21. doi: 10.1177/1602400219.

24. Spaanderman DJ, Hakkesteegt SN, Hanff DF, Schut ARW, Schiphouwer LM, Vos M, et al. Multi-center external validation of an automated method segmenting and differentiating atypical lipomatous tumors from lipomas using radiomics and deep-learning on MRI. EClinicalMedicine 2024;76:102802. doi: 10.1016/j.eclinm.2024.102802.

THE ASEAN JOURNAL OF RADIOLOGY
ISSN 2672-9393

Original Article

Evaluation of the clinical utility of liver MRI T2* as a surrogate marker in liver iron overload: Experience from a Malaysian haematology referral centre

Mohd Zulkimi Roslly, M.D., Dr.Rad.[1, 3]
Nizam Baharom, M.B.B.S., M.P.H., Dr.P.H.[3]
Mohd Firdaus A Bakar, M.B.B.Ch., M.R.C.P.[2, 3]
Arissa Chua Ai Ting, M.B.B.S.[4]
Siti Maisarah Abdl Rahman, M.B.B.Ch., B.A.O.[4]
Noor Komalasari Roslan, M.B.B.Ch.[4]
Wan Asma' Wan Mohd Yusof, M.B.B.S.[4]
From [1]Radiology Unit, [2]Internal Medicine Unit, [3]Faculty of Medicine and Health Sciences, Universiti Sains Islam Malaysia, Negeri Sembilan, Malaysia,
[4]Radiology Department, Hospital Ampang, Ampang Jaya, Selangor, Malaysia.
Address correspondence to M.Z.R. (email: zulkimiroslly@usim.edu.my)

Received 1 February 2026; revised 10 March 2026; accepted 27 March 2026
doi:10.46475/asean-jr.v27i2.1017

Abstract

Introduction: Thalassaemia significantly contributes to the disease burden in South-east Asia, particularly due to complications such as liver iron overload from long-term blood transfusions. The assessment of liver iron overload moves from liver biopsy towards non-invasive methods by utilizing MRI T2* technique. This study evaluated the clinical utility of MRI T2* as a gold standard for assessing hepatic iron overload, and investigated its correlation with serum ferritin and other clinical parameters.

Materials and Methods: A one-year cross-sectional study was conducted on Thalassaemia patients who underwent MRI T2* in the year 2025. Liver iron concentration (LIC) was calculated using cvi-42 post-processing software and the serum ferritin levels, transfusion regimen, and demographic data were recorded. The relationships between T2* values, serum ferritin, and other clinical parameters were then analysed.

Results: A total of 158 Thalassaemia patients, predominantly transfusion-dependent, were enrolled. HbE-Beta Thalassaemia was the most common subtype (48.1%), followed by Beta-Thalassaemia Major (24.7%). Severe liver iron overload was observed in 63.3% of patients, with Malay patients exhibiting higher severity than Chinese patients ($p<0.001$). Serum ferritin levels showed a strong negative correlation with liver T2* values ($Rs = -0.699$, $p < 0.001$) However, the type of Thalassaemia, transfusion duration and regimen were not significantly associated with T2* values or LIC.

Conclusion: Liver MRI T2* demonstrated an effective assessment of hepatic iron overload, exhibiting a strong correlation with serum ferritin levels. These findings elucidate the reliability of MRI T2* imaging to be utilized in the management of transfusion-related iron overload.

Keywords: Ferritin, Iron, Liver iron concentration, Malaysia, MRI T2*, Thalassaemia.

Introduction

Haemoglobin disorders represent a significant global health burden, with 71% of 229 countries reporting a substantial prevalence. Notably, these countries account for 89% of all live births worldwide, of whom 83% have sickle cell disorders and 17% have Thalassaemia [1]. These disorders impact 89% of newborns worldwide, with approximately 330,000 newborns affected annually, Thalassemia, a hereditary haematological disease identified nearly a century ago, is characterized by ineffective erythropoiesis and requires regular blood transfusions to prevent severe anaemia and maintain adequate haemoglobin levels [2]. According to Weatherall et al., Thalassaemia is most prevalent in the tropical belt [3], with high incidences reported in populations from the Mediterranean Basin, the Middle East, the Indian subcontinent, Southeast Asia, Melanesia, and the Pacific Islands, including Malaysia [4]. The Malaysian Thalassemia Registry (MTR) 2019 reported 8,681 registered thalassemia patients in Malaysia, revealing that a majority, exceeding 50%, presented with transfusion-dependent thalassemia (TDT) [5].

THE ASEAN JOURNAL OF RADIOLOGY
ISSN 2672-9393

Transfused iron is deposited first within the reticuloendothelial cells prior to parenchymal iron loading within the heart and liver [6], and this begins as early as one year after the initiation of treatment [7]. Multiple organs are susceptible to excessive iron accumulation, with the liver being the most affected, followed by the myocardium and endocrine glands [8]. While other organs, such as the pancreas, brain, and additional endocrine glands, may also be impacted, the liver and myocardium are among the most commonly monitored sites. Local guidelines recommend serum ferritin measurement for the assessment of iron overload, with iron chelation therapy initiated when serum ferritin levels exceed 1000 µg/L [9].

If left untreated or managed with inadequate chelation, chronic iron overload in the liver can lead to liver fibrosis and cirrhosis, increasing the risk of developing hepatocellular carcinoma [10]. Consequently, regular monitoring of iron overload and ensuring the adequacy of iron chelation therapy are crucial, as emphasized by the Malaysian Ministry of Health, particularly through the utilization of MRI T2*. According to the Malaysian Clinical Practice Guideline for the Management of Thalassaemia, MRI T2* assessment is recommended every 1–2 years for patients who are not receiving chelation therapy, and every 6–12 months for patients undergoing chelation therapy [9]. Prior investigations have explored the use of MRI for assessing hepatic iron concentration; however, in 2005, St. Pierre et al. introduced MRI T2* as a novel, non-invasive method for quantifying liver iron concentration [11]. They outlined the methods, MRI parameters, and image analysis techniques, establishing T2* value categories calibrated against liver biopsy findings. This breakthrough became a cornerstone in global Thalassaemia management. Later, a comprehensive 10-year study by the Thalassemia Longitudinal Cohort, involving North American and British patients in year 2012, further highlighted the critical role of MRI in assessing and monitoring liver iron concentration (LIC) [12].

Despite the increased availability of MRI facilities in Malaysia, comprehensive data on MRI T2* for LIC assessment from treating centres remain limited. Only one state out of the 14 has provided limited data on the use of MRI T2* to monitor liver iron overload, as reported in the latest MTR [5, 6]. Therefore, this study aims to contribute valuable findings and data on the role of MRI T2* in quantifying hepatic iron overload, particularly within the largest Malaysian cohort of patients with TDT.

Materials and methods

Study design and study population:
This is a cross-sectional study employing a universal sampling method, with samples obtained over one year period from January 2025 to December 2025. We included all patients who underwent MRI examinations for LIC assessment. This study was conducted at Hospital Ampang, the national referral centre for adult haematological disorders treating the highest number of thalassaemia patient in Malaysia. The cases included individuals with hemoglobinopathies, primarily Thalassaemia, who had received blood transfusions and were experiencing iron overload. Exclusion criteria consisted of patients who underwent MRI T2* for purposes other than LIC assessment, as well as those with concurrent liver lesions or malignancies. Assuming a 30% prevalence of severe iron overload among thalassaemia patients in Malaysia and a total population of approximately 800 patients at our center, the adjusted sample size required for the study, with a 95% confidence level and 5% precision, was 188.

Patients were selected based on the inclusion and exclusion criteria from the Picture Archiving and Communication System (PACS). MRI T2* values, along with demographic data, blood parameters, and transfusion history, were retrieved from the E-Hospital Information System (E-HIS) for further analysis.

As this study was considered as a human study, we adhered to the principles outlined in the Declaration of Helsinki. This study was approved by the Malaysia National Medical Research Registry and Medical Research Ethics Committee.

Image acquisition:
The MRI scans were performed by qualified radiographers with over 10 years of experience, using a 1.5T United Imaging uMR570 MRI machine (2020 Shanghai United Imaging Healthcare Co., Ltd, China). A torso coil was used to minimize signal drop and ensure signal homogeneity throughout the scanning area. Non-ECG gated 'white blood' imaging was performed at the level of the upper abdomen in free breathing for topographic purposes. Following this, T2* imaging of the liver was conducted using a single breath-holding technique. Liver images were acquired in the axial plane at eight different echo times (TE) in millisecond (ms) intervals to evaluate the magnitude and rate of signal decay.

The scanning parameters were as follows: Time of Echo (TE) ranging from 0.98 to 6.23 ms, repetition time (TR) maintained at 7.39 ms throughout the scan, flip angle set to 20 degrees, field of view (FOV) of 300-400 x 200-300 mm, matrix size of 132 x 340

THE ASEAN JOURNAL OF RADIOLOGY
ISSN 2672-9393

pixels, slice thickness of 2.0 mm, and bandwidth of 1500 Hz. The total scan time varied depending on the patient's ability to cooperate with breath-holding. Post-processing analysis was conducted using specialized software (Thalassemia-Tools; Cardiovascular Imaging Solutions, cvi42, London, United Kingdom) to measure the T2* value. Two regions of interest (ROIs), with an elliptical size of 3 - 4 cm2 were placed either the right or left lobe (preferably the right lobe) in the axial plane at the porta hepatis level to calculate the T2* value, generating a signal decay versus time graph. The ROIs also needed to avoid of vessels, bone or air. The corresponding LIC was then generated (Figure 1). This approach was based on the study by Hernando D et al. [13], with the right lobe selected due to its signal homogeneity and reduced susceptibility to breathing motion artefacts.

Image analysis:
Based on the two ROIs (purple and green), the T2* value and corresponding signal decay curve were generated using the post-processing software CVi42. Identical T2* values and overlapping signal decay curves from both ROIs indicate that the selected regions are representative of the liver iron concentration (LIC) (Figure 1). The corresponding LIC, were classified into the following categories: normal (<2 mg/g), light (2-7 mg/g), moderate (8-15 mg/g), and severe (>15 mg/g) iron load as outlined by St Pierre in 2005 [11].

Serum ferritin:
The most recent serum ferritin level, measured within six months before the MRI date, was recorded for analysis to ensure accuracy in comparison with the T2* values. Serum ferritin serves as a clinically relevant biomarker of total body iron stores at the time of assessment. Despite this, its interpretation should be approached with caution, particularly in the presence of acute inflammation, underlying hepatitis, or when ferritin levels are markedly elevated.

Hemoglobinopathies, transfusion history, and iron chelation therapy:
This information for each study participant was obtained from the E-HIS and recorded. Hemoglobinopathies were classified into five categories based on the previous MTR: Beta-Thalassaemia Major, Beta-Thalassaemia Intermedia, HbE-Beta Thalassaemia, HbH Disease, and other hemoglobinopathies.

Transfusion history, including the duration of transfusion, transfusion frequency, and the type of iron chelation therapy, was also recorded. The duration of transfusion was calculated from the date of the first transfusion and expressed in years. The transfusion regimen was categorized into three groups: ≤6 weekly, >6 weekly, and Non-Transfusion

Dependent (NTD). Following the previous MTR, iron chelation therapy was categorized as follows: desferrioxamine (DFO), deferiprone (DFP), deferasirox (DFX), a combination of two or more iron chelators, and no chelation therapy. For statistical purposes, these parameters were recategorized as detailed in Tables 1 and 2.

Statistical analysis:
Data were analysed using the Statistical Package for Social Sciences (SPSS) version 24.0 [IBM Corp. Released 2023. IBM SPSS Statistics for Macintosh, Version 29.0.1.0 Armonk, New York: IBM Corp]. Descriptive statistics were used to assess demographic and clinical data. Normality tests were performed on continuous variables, and appropriate non-parametric tests were applied where necessary. A p-value of <0.05 was considered statistically significant.

Results

Table 1. *Clinical characteristics of the patients (n=158).*

Variables	n (%)	Mean (SD), or Median (IQR)
Gender		
Male	57 (36.1)	
Female	101 (63.9)	
Age (year)		
Mean (SD)		30.7 (11.75)
< 18	14 (8.9)	
18 - 29	66 (41.8)	
30 – 39	53 (33.5)	
40 – 49	19 (12.0)	
> 50	6 (3.8)	
Race		
Malay	129 (81.6)	
Chinese	29 (18.4)	

THE ASEAN JOURNAL OF RADIOLOGY
ISSN 2672-9393

Variables	n (%)	Mean (SD), or Median (IQR)
Type of Thalassaemia		
Beta-Thalassaemia Major	39 (24.7)	
Beta-Thalassaemia Intermedia	8 (5.1)	
HbE-Beta Thalassaemia	76 (48.1)	
HbH Disease	10 (6.3)	
Other Hemoglobinopathies	25 (15.8)	
Duration of transfusion (year), n=115		
Mean (SD)		19.3 (10.26)
< 10	27 (23.5)	
10-19	28 (24.3)	
20-29	38 (33.1)	
> 30	22 (19.1)	
Transfusion regimen		
≤ 6 weekly	111 (70.3)	
> 6 weekly	26 (16.5)	
NTD	21 (13.2)	
Patient on iron chelator		
DFO only	20 (12.7)	
DFP only	72 (45.6)	
DFX only	7 (4.4)	
Combination therapy	42 (26.6)	
Not on iron chelator	17 (10.8)	
Serum Ferritin level, (ng/mL)		
Median (IQR)		1.57 (2.40)
Min - max		0.30 – 24.00
Liver iron concentration (LIC), mg/g		
Mean	28.30	
Median	23.26	
Min - max	0.81 – 106.00	
Severity of LIC		
Normal	8 (5.1)	
Light	17 (10.8)	
Moderate	33 (20.9)	
Severe	100 (63.3)	

Table 2. *Liver iron concentration in relation to demographics, types of hemoglobinopathy and transfusion parameters (n=158).*

Variables	Liver iron concentration (LIC)		*p*
	Non-Severe [normal, mild, and moderate] (n, %)	Severe	
Gender			
Male	16 (28.1)	41 (71.9)	0.323
Female	42 (41.6)	59 (58.4)	
Age (year)			
< 18	7 (50.0)	7 (50.0)	
18 - 39	45 (37.8)	74 (62.2)	0.239
> 40	6 (24.0)	19 (76.0)	
Race			
Malay	38 (29.5)	91 (70.5)	<0.001
Chinese	20 (69.0)	9 (31.0)	
Type of Thalassaemia			
Beta-Thalassaemia	45 (36.6)	78 (63.4)	
Alpha-Thalassaemia	3 (30.0)	7 (70.0)	0.856
Other Hemoglobinopathy	10 (40.0)	15 (60.0)	
Duration of transfusion (year), n=115			
< 10	8 (29.6)	19 (70.4)	
10-19	13 (46.4)	15 (53.6)	0.372
20-29	13 (34.2)	25 (65.8)	
> 30	11 (50.0)	11 (50.0)	
Transfusion regimen			
≤ 6 weekly	41 (36.9)	70 (63.1)	
> 6 weekly	8 (30.8)	18 (69.2)	0.691
NTD	9 (42.9)	12 (57.1)	
Patient on iron chelator			
Monotherapy	32 (32.3)	67 (67.7)	
Combination therapy	18 (42.9)	24 (57.1)	0.319
Not on iron chelator	8 (47.1)	9 (52.9)	

Table 3. *Non-parametric correlation between the MRI T2* and serum ferritin and liver iron concentration (n=158).*

Variables	Median (IQR)	r	*P*
Serum Ferritin, (ng/mL)	1584.5 (2090.0)	-0.699	< 0.001
MRI T2* value	1.57 (2.40)		
Liver Iron Concentration, (mg/g)	23.26 (35.76)	-0.982	< 0.001
MRI T2* value	1.57 (2.40)		

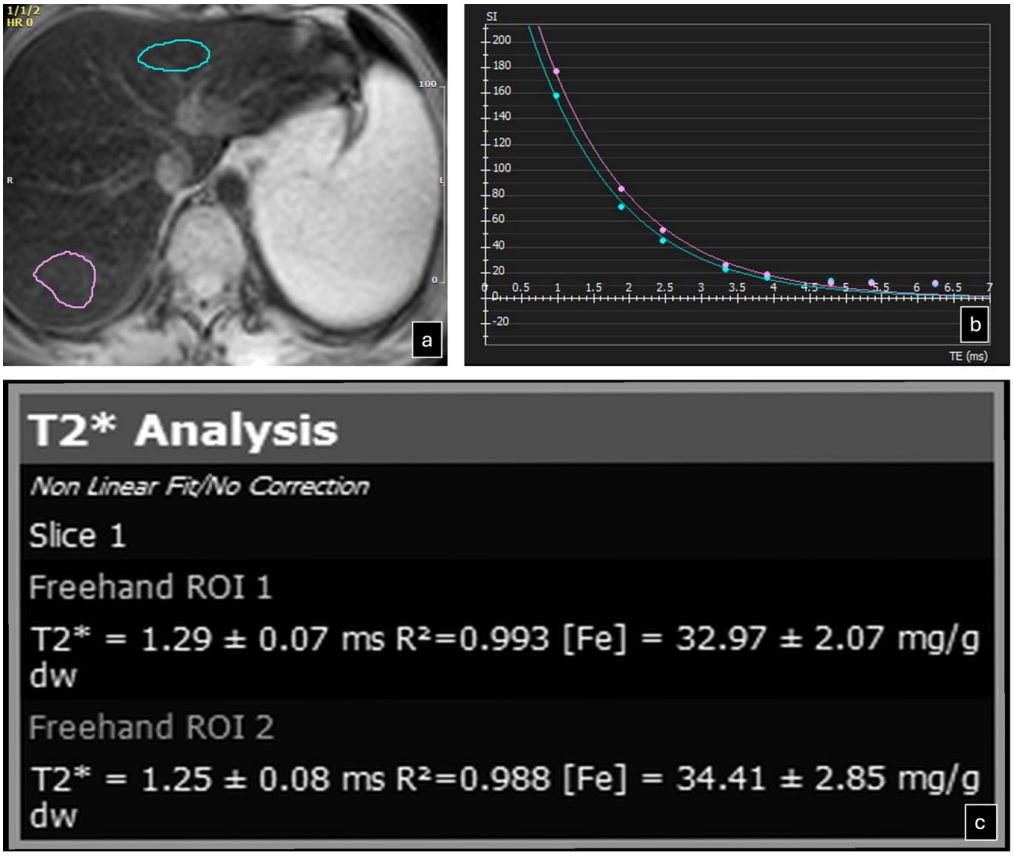

Figure 1. *Example of post-processing data images using cvi42. (a) The ROI (purple and green) was placed at the right or the left lobe of the liver, where the region must be devoid of vessels, bone or air. (b) The signal intensity at these regions in eight different echo time (TE) was automatically plotted and subsequently, the T2* value with its corresponding R2 and liver iron concentration (in mg/g) were expressed. (c) The T2* value for each ROI was expressed with +/- standard deviation, along with its corresponding LIC.*

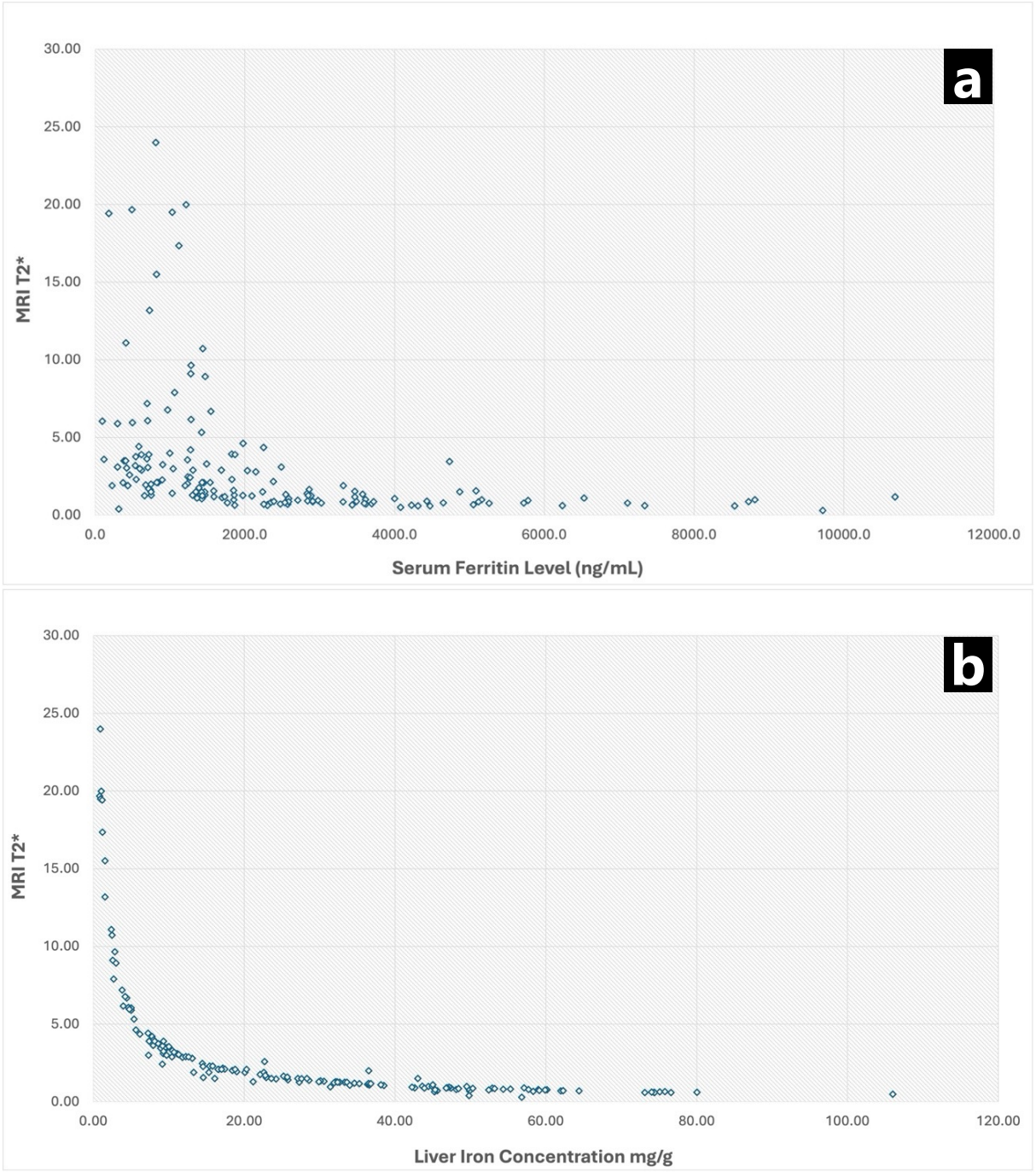

Figure 2. *Scatter plots of MRI T2* values versus serum ferritin levels (a) and liver iron concentration (b) in 158 patients demonstrated significant, strong negative correlations for both relationships.*

THE ASEAN JOURNAL OF RADIOLOGY
ISSN 2672-9393

Demography:
A total of 158 MRI T2* of the liver studies were performed throughout the study period regardless of the type of hemoglobinopathy, comprised of 57 male (36.1%) and 101 female patients (63.9%). The mean age was 30.7 years with the youngest and oldest cases being 7 and 73 years old respectively. The majority of cases were from the 18-29 years old group (41.8%). In this study, most thalassemia patients were of Malay ethnicity (81.6%, n=129), followed by Chinese ethnicity (18.4%, n=29). Notably, no patients of Indian ethnicity were represented in this study.

The most common type of Thalassaemia encountered was HbE-Beta Thalassaemia which was 48.1% (n=76) followed by Beta-Thalassaemia Major at 24.7% (n=39). While HbH disease and Beta-Thalassaemia Intermedia contributed to 6.3% (n=10) and 5.1% (n=8) respectively. Other rarer types of hemoglobinopathies were also encountered, such as HbH Constant Spring, Adana + Constant Spring, and other heterozygous hemoglobinopathies, which collectively contributed to 15.8% (n=25) of all patients.

Transfusion regimen:
The total duration of transfusion (in years) was classified into several categories: <10 years, 10-19 years, 20-29 years, and >30 years. However, the documentation on the total duration of transfusion was only available in 115 out of 158 patients, where the mean, SD duration of transfusion was 19.3,10.26 years. The majority of patients had received transfusions for 20-29 years (n=38, 33.1%). The shortest duration was one year, and the longest was 41 years.
According to the MTR 2019, regular transfusion was defined as the requirement for packed red blood cell transfusions at least once every six weeks to maintain optimal haemoglobin levels [5]. The majority of the patients were receiving regular transfusion (70.3%, n=111) while only 26 patients (16.5%) were receiving more than 6-weekly packed cell transfusion. A minority of the cases (13.2%, n=21) were classified as NTD, with the majority of these patients diagnosed with the HbH subtype or other rare hemoglobinopathies.

Both duration of transfusion and transfusion regimen showed no significant correlation with the LIC, (p=0.372 and p=0.691, respectively) (Table 2).

Iron chelation therapy:
Among the 158 patients included in this study, the majority were receiving iron chelation therapy. Deferiprone (DFP) monotherapy was the most common regimen, used by 72 patients (45.6%). This was followed by combination therapy in 42 patients (26.6%) and deferoxamine (DFO) monotherapy in 20 patients (12.7%). A smaller proportion of

patients were treated with deferasirox (DFX) monotherapy (7 patients, 4.4%). Seventeen patients (10.8%) were not receiving any iron chelation therapy at the time of the study. However, the type of iron chelation did not show a significant association with the liver iron concentration (p = 0.319) (Table 2).

Serum ferritin:
All patients had the latest serum ferritin level recorded within 6 months of the MRI T2* examination. Serum ferritin levels were below 2500 ng/mL in 67.7% of the study population, with a median (IQR) of 1584.5 (2.4) ng/mL. A minority of patients (9.5%, n=16) demonstrated serum ferritin concentrations exceeding 5000 ng/mL. Notably, one patient (0.6%) presented with a markedly elevated serum ferritin level, surpassing 10000 ng/mL, and was diagnosed with diffuse large B-cell lymphoma (DLBCL) involving the bone marrow.

MRI T2*:
The T2* values were divided into four categories based on previously established research (10). The T2* value corresponds to the LIC, which is measured as the weight of iron (in milligrams, mg) in each gram of dry liver tissue (in gram, g). The mean LIC in patients was 28.3 mg/g where most of the patients have severe iron overload (63.3%, n=100), followed by moderate iron load (20.9%, n=33), light iron load (10.8%, n=17), and normal iron load (5.1%, n=8).

Liver iron concentration:
MRI T2* value was inversely proportional to the liver iron concentration in a negative exponential manner (Figure 2(b)), as the iron deposition in the liver parenchyma alters the MRI T2* relaxation time (13). Based on the MRI T2* value with its corresponding LIC, we categorized the cohort into four categories: normal, mild, moderate, and severe. In Table 2, using the Chi-Square Test, the correlation between the LIC categories and gender, age, and ethnicity is shown. There was no significant correlation between gender or age and LIC. There was a significant strong correlation between LIC and ethnicity ($p<0.001$), indicating that patients of Chinese ethnicity presented with less severe hepatic iron overload than those of Malay ethnicity. After adjustment for confounders were made including gender, age group, transfusion duration, and chelation therapy using binary logistic regression, Chinese ethnicity remained significantly associated with a lower likelihood of severe liver iron overload compared to Malay patients (adjusted odds ratio = 0.079, 95% CI: 0.078 to 0.045, $p < 0.001$).

THE ASEAN JOURNAL OF RADIOLOGY
ISSN 2672-9393

The type of Thalassaemia and total duration of blood transfusion were not significantly different among the groups of patients. We noticed that among our patients who had been receiving blood transfusions for more than 30 years, 50% (n=11) of patients had severe liver iron overload and another 50% (n=11) had from mild and moderate liver iron load. Similarly, the transfusion regimen did not show a significant correlation with the degree of LIC.

Correlations between the MRI T2* values with serum ferritin and LIC values:
The liver MRI T2* values ranged from 0.30 to 24.00 ms (median 1.57, IQR 2.40). The median serum ferritin level is 1584.5 ng/mL, ranging from 95.1 to 10682.4 ng/mL with an interquartile range (IQR) of 2090.0 ng/mL. The correlation coefficient (r) is -0.699, indicating a significant, strong negative correlation with the MRI T2* value (p-value < 0.001).

The LIC ranged from 0.81 to 106.00 mg/g with an interquartile range (IQR) of 35.76 mg/g. As expected, LIC demonstrated a strong inverse correlation with MRI T2* ($r = -0.982$, $p < 0.001$).

In summary, both serum ferritin and liver iron concentration show strong negative correlations with MRI T2* values, with liver iron concentration exhibiting an even stronger negative correlation than serum ferritin. From these findings, the total body iron load, demonstrated by the serum ferritin and liver iron concentration were reflected by the shortening of liver parenchyma T2* relaxation time.

Discussion

Thalassemia is a prevalent inherited haematological disorder in this region, particularly within the Thalassemia Belt, which encompasses the Mediterranean, Middle East, and Southeast Asia, including Malaysia [4]. Although local clinical guidelines and a national disease registry have been established, the latest Malaysian Thalassemia Registry lacks comprehensive MRI T2* data. This deficiency stems from the delayed implementation of MRI as a non-invasive diagnostic modality for liver iron overload in Malaysia, a practice that has gained prominence only in the last decade, replacing the previously established gold standard of liver biopsy.

Gender:
Based on a large systematic analysis conducted by Tuo Y. et al. [14] and the latest local registry [5], there is no gender predilection among Thalassaemia patients as it is attributed to the non-sex chromosome involvement in globin chain synthesis. This is also supported by Hoe HG et al. from local data, which shows equal gender involvement [15]. In contrast, our study showed a disparity in gender involvement, where 36.1% and 63.9% of patients are male and female respectively. This is possibly because our cohort consisted only of the patients who underwent MRI examinationand therefore does not represent the whole Thalassaemia patients in our centre.

Although both genders demonstrated severe liver iron overload, there is no significant association between the genders in determining the degree of LIC. Similar to a study done by Khadivi and co-workers in 2021, there was no significant difference between the degree of LIC with the gender [16].

Ethnicity:
The three major ethnicities in Malaysia are Malays, Chinese and Indians followed by other smaller ethnics. In this cohort, it is not surprising that Malays dominate the number of patients (81.6%) followed by Chinese. This is consistent with findings by Alwi ZB et al. where he reported 62% of Thalassaemia patients in his cohort are Malays, followed by Chinese and Kadazan-Dusuns [17]. Similarly, Mohd Ibrahim et al. reported 64.0% of Thalassaemia patient in Malaysia were Malays followed by Chinese (17.5%) and Kadazan-Dusuns (11.36%). Although Indians made up the third largest ethnicity in Malaysia, the number of Indians affected by Thalassaemia is low; less than 1% [5] while in our study, no Indians were recorded. This is possibly because the ancestors of Indian ethnicity in Malaysia originated from South India, which rarely had α-thalassaemia or β-thalassaemia [16].

An interesting finding in our cohort was the Chinese had a significantly lower number of severe liver iron overload as compared to other races. There was a strong, significant correlation between the LIC and ethnicity ($p<0.001$) where the Chinese had less severe liver iron overload as compared to the Malays. To our knowledge, there is no specific study looking into the factors contributing to this pattern. A small number of Chinese ethnicities in our cohort may not be representative of all Thalassaemia patients in Malaysia; therefore, further studies with larger sample sizes are needed to confirm this correlation. Furthermore, only 115 patients have their record on the duration of blood transfusion that included in the analysis.

THE ASEAN JOURNAL OF RADIOLOGY
ISSN 2672-9393

MRI T2* with serum ferritin and LIC:
Until the last two decades, MRI T2* has become the gold standard in determining liver iron overload and hospitals in Malaysia have started to utilize this tool within the past decade [9]. The calibration of T2* relaxation time with the degree of iron deposition in the histological specimens became the foundation of this technique [11], and the safety of this method has been well established by Angelucci et al. in their large study [19]. Recently, the neighbouring countries have also started to utilize MRI for evaluation of liver iron overload [20].

There are significant limitations of MRI for this purpose, particularly in a developing country including Malaysia in terms of cost, patient logistics, machine availability and long-waiting MRI appointment. These factors force the utilization of serum ferritin as the indicator for monitoring hepatic iron overload, a method considered second-best after biopsy in some centres. This resulted in lacking MRI T2* data being recorded in the previous Thalassaemia Registry [5]. Our cohort, being the first comprehensive data from the second largest centre in treating Thalassaemia patients has shown promising results, in line with the previously published data.

The MRI T2* value significantly correlated with the serum ferritin ($p<0.0001$, r -0.699) indicating the accuracy and reliability of the technique used in our centre, in line with evidence from neighbouring countries [20]. The results presented indicate a significant negative correlation between serum ferritin levels and liver iron concentration with MRI T2* values with a correlation coefficient (r) of -0.699 with a p-value of < 0.001. In conclusion, the serum ferritin levels increase, the MRI T2* values decrease, reflecting greater liver iron overload.

Similarly, the liver iron concentration showed an even stronger correlation ($r = -0.982$, $p < 0.001$) with MRI T2* values. This suggests that liver iron concentration is a critical factor in determining MRI T2* values, which are used to assess tissue iron levels non-invasively.

When comparing these findings to previous literature, several studies have established the relationship between serum ferritin, liver iron concentration, and MRI T2* values. For instance, studies have shown that elevated serum ferritin is a reliable marker for iron overload conditions, such as hemochromatosis and thalassemia, where MRI T2* is utilized to quantify liver iron concentration. These findings support the notion that MRI T2* is a valuable tool for assessing iron overload, correlating well with both serum ferritin and liver biopsy results [11, 21-22]. The negative correlation coefficients suggest that MRI T2* can serve as a non-invasive alternative to liver biopsy for evaluating iron burden, which is particularly beneficial in clinical settings where biopsy may pose risks or be impractical.

Limitations:
Only 158 samples were enrolled in this study due to several limitations such as machine breakdown and patients not turning up for MRI appointments. This smaller sample size represents a limitation of this study, as it may have reduced the statistical power and affected the precision and generalizability of the results. Although the achieved sample size was slightly lower than the calculated requirement, the study still included a substantial proportion of the eligible patient population at our center.

Another limitation is the unequal distribution of ethnicity and the degree of liver iron overload in our cohort which may lead to bias in the data analysis.

Conclusion

This study reinforces the established understanding of the relationship between serum ferritin, liver iron concentration, and MRI T2* values. The strong correlations observed highlight the utility of MRI T2* as a diagnostic tool in managing patients with iron overload, supporting findings from previous research in the field. Further studies could explore the implications of these findings in clinical practice, particularly in monitoring treatment efficacy in iron overload disorders. Whenever possible, monitoring of other susceptible organ for iron overload especially the myocardium, should be routinely performed in correlation with LIC. In a limited-resource centre, there is a need for more simplified and cost-effective methods to assess iron overload, particularly in TDT patients, the exploration of novel imaging modalities remains a significant research priority.

Conflict of interest

There is also no conflicts of interest between the authors which may affect the quality of this research and writing of this manuscript.

Funds

This study did not receive any specific grant from funding agencies in the public, commercial, or not-for-profit sectors.

References

1. Modell B, Darlison M. Global epidemiology of haemoglobin disorders and derived service indicators. Bull World Health Organ 2008;86:480-7. doi: 10.2471/blt.06.036673.

2. Argyropoulou MI, Astrakas L. MRI evaluation of tissue iron burden in patients with beta-thalassaemia major. Pediatr Radiol 2007;37:1191-200; quiz 1308-9. doi: 10.1007/s00247-007-0567-1.

3. Weatherall DJ. The evolving spectrum of the epidemiology of thalassemia. Hematol Oncol Clin North Am 2018;32:165-75. doi: 10.1016/j.hoc.2017.11.008.

4. De Sanctis V, Kattamis C, Canatan D, Soliman AT, Elsedfy H, Karimi M, et al. β-Thalassemia distribution in the Old World: an ancient disease seen from a historical standpoint. Mediterr J Hematol Infect Dis 2017;9:e2017018. doi: 10.4084/MJHID.2017.018.

5. Mohd Ibrahim H, Alias H, Muda Z, Gunasagaran K, Osman R. Annual report of the Malaysian Thalassaemia Registry 2019. Kuala Lumpur: Ministry of Health Malaysia; 2019.

6. Mishra AK, Tiwari A. Iron overload in beta-thalassaemia major and intermedia patients. Maedica (Bucur) 2013;8:328-32.

7. Taksande A, Prabhu S, Venkatesh S. Cardiovascular aspect of beta-thalassaemia. Cardiovasc Hematol Agents Med Chem 2012;10:25-30. doi: 10.2174/187152512799201172.

8. Coates TD. Physiology and pathophysiology of iron in hemoglobin-associated diseases. Free Radic Biol Med 2014;72:23-40. doi: 10.1016/j.freeradbiomed.2014.03.039.

9. Ministry of Health Malaysia. Clinical practice guidelines: Management of thalassaemia. 2nd ed. Kuala Lumpur: Ministry of Health Malaysia; 2024.

10. Taher AT, Saliba AN. Iron overload in thalassemia: different organs at different rates. Hematology Am Soc Hematol Educ Program 2017;2017:265-71. doi: 10.1182/asheducation-2017.1.265.

11. St Pierre TG, Clark PR, Chua-anusorn W, Fleming AJ, Jeffrey GP, Olynyk JK, et al. Noninvasive measurement and imaging of liver iron concentrations using proton magnetic resonance. Blood 2005;105:855-61. doi: 10.1182/blood-2004-01-0177.

12. Kwiatkowski JL, Kim HY, Thompson AA, Quinn CT, Mueller BU, Odame I, et al. Chelation use and iron burden in North American and British thalassemia patients: a report from the Thalassemia Longitudinal Cohort. Blood 2012;119:2746-53. doi: 10.1182/blood-2011-04-344507.

13. Hernando D, Zhao R, Yuan Q, Aliyari Ghasabeh M, Ruschke S, Miao X, et al. Multi-center reproducibility of liver iron quantification with 1.5-T and 3.0-T MRI. Radiology 2023;306:e213256. doi: 10.1148/radiol.213256.

14. Tuo Y, Li Y, Li Y, Ma J, Yang X, Wu S, et al. Global, regional, and national burden of thalassemia, 1990-2021: a systematic analysis for the Global Burden of Disease Study 2021. EClinicalMedicine 2024;72:102619. doi: 10.1016/j.eclinm.2024.102619.

15. Hoe HG, Git KA, Loh CK, Abdul Latiff Z, Hong J, Abdul Hamid H, et al. Magnetic resonance imaging T2* of the pancreas value using an online software tool and correlate with T2* value of myocardium and liver among patients with transfusion-dependent thalassemia major. Front Radiol 2022;2:943102. doi: 10.3389/fradi.2022.943102.

16. Khadivi Heris H, Nejati B, Rezazadeh K, Sate H, Dolatkhah R, Ghoreishi Z, et al. Evaluation of iron overload by cardiac and liver T2* in β-thalassemia: correlation with serum ferritin, heart function and liver enzymes. J Cardiovasc Thorac Res 2021;13:54-60. doi: 10.34172/jcvtr.2021.18.

17. Alwi ZB, Syed-Hassan SR. Thalassemia in Malaysia. Hemoglobin 2022;46:45-52. doi: 10.1080/03630269.2022.2057326.

18. Tan JA, Chin PS, Wong YC, Tan KL, Chan LL, George E. Characterisation and confirmation of rare beta-thalassaemia mutations in the Malay, Chinese and Indian ethnic groups in Malaysia. Pathology 2006;38:437-41. doi: 10.1080/00313020600922538.

19. Di Tucci AA, Matta G, Deplano S, Gabbas A, Depau C, Derudas D, et al. Myocardial iron overload assessment by T2* magnetic resonance imaging in adult transfusion-dependent patients with acquired anemias. Haematologica 2008;93: 1385-8. doi: 10.3324/haematol.12759.

20. Chaosuwannakit N, Makarawate P. The value of magnetic resonance imaging in evaluation of myocardial and liver iron overload in a thalassaemia endemic population: a report from Northeastern Thailand. Pol J Radiol 2019;84:e262-8. doi: 10.5114/pjr.2019.86094.

21. Anderson LJ. Assessment of iron overload with T2* magnetic resonanceimaging. Prog Cardiovasc Dis 2011;54:287-94. doi: 10.5114/pjr.2019.86094.

22. Wood JC, Enriquez C, Ghugre N, Tyzka JM, Carson S, Nelson MD, et al. MRI R2 and R2* mapping accurately estimates hepatic iron concentration in transfusion-dependent thalassemia and sickle cell disease patients. Blood 2005;106:1460-5. doi: 10.1182/blood-2004-10-3982.

Original Article

BI-RADS 4 and 5 lesions on mammography and ultrasonography: Positive predictive values and analysis of discordant cases

Piyakan Pathanasethpong, M.D.
Napatsorn Palitvanon, M.D.
From Department of Radiology, Faculty of Medicine, Khon Kaen University, Khon Kaen, Thailand.
Address correspondence to P.P. (email: piyapa@kku.ac.th)

Received 26 October 2025; revised 3 March 2026; accepted 9 May 2026
doi:10.46475/asean-jr.v27i2.993

Abstract

Background: Breast cancer is the leading cause of morbidity and mortality among women worldwide, including Thailand. Early detection and treatment significantly decrease mortality. The accuracy and effectiveness of mammograms are important in early breast cancer detection. In the present study, the positive predictive values of BI-RADS categories were compared against the suggested values and the histopathological results for the purposes of auditing, quality assurance, and benchmarking.

Objective: To determine the positive predictive values of different BI-RADS categories and compare the values against the suggested values based on the BI-RADS 2013 Standard, and to describe the discordant cases (cases with a mismatch between imaging and BI-RADS categorization) to determine how the misdiagnoses might happen.

Materials and Methods: This retrospective diagnostic study was conducted at Srinagarind Hospital, Thailand, between 1 January 2017 and 31 December 2021. It included 1,666 breast lesions in BIRADS 4 and 5 that had undergone image-guided biopsy (ultrasound or tomosynthesis-guided biopsy) to assess the positive rates of breast cancer among these lesions.

THE ASEAN JOURNAL OF RADIOLOGY
ISSN 2672-9393

Results: The 1,666 breast lesions were in the BI-RADS subtype categories 4A (n=899), 4B (n=492), 4C (n=149), and 5 (n=126), with positive rates for breast cancer of 5.01%, 19.51%, 57.05%, and 89.68%, respectively, with category 5 showing a lower positive rate than the standard. The discordant cases were mostly overdiagnoses of benign morphologies.

Conclusions: The positive rates of lesions in the BI-RADS 4 subcategories were within the expected ranges, whereas the positive rate of lesions in the BI-RADS 5 category was lower than expected, indicating overcategorization.

Keywords: Breast cancer, BI-RADS, Positive predictive value.

Introduction

On a global scale, breast cancer remains a primary driver of oncological morbidity and mortality. In 2022, approximately 2.3 million women were newly diagnosed with the disease, resulting in over 670,000 fatalities [1]. Within Thailand, the incidence of breast cancer has risen consistently over the past twenty years, surpassing cervical and colorectal cancers to become the most prevalent malignancy among Thai women [2].

Given that early-stage breast cancer is frequently asymptomatic, the implementation of robust screening programs and early detection initiatives is critical. Substantial evidence from large-scale studies confirms that mammography significantly reduces breast cancer mortality [3-5]. While mammography and ultrasonography serve as the primary non-invasive modalities for evaluating breast abnormalities, a definitive diagnosis necessitates histopathological assessment—typically achieved through image-guided core needle biopsy, tomosynthesis-guided biopsy, or minimally invasive surgical procedures.

To ensure standardized reporting of breast lesions, the American College of Radiology (ACR) developed the Breast Imaging Reporting and Data System (BI-RADS) [6]. This classification framework enhances the accuracy and consistency of imaging interpretation and serves as a vital instrument for predicting malignancy.

Under current guidelines, lesions categorized as BI-RADS 4 or 5 warrant tissue sampling for histopathological verification. However, the positive predictive values (PPVs) for these categories exhibit significant variability across different institutions and popu-

lations [7-13]. Consequently, institutional audits comparing radiological findings with pathological outcomes are recommended to maintain quality assurance and benchmark performance against established BI-RADS standards.

The diagnostic efficacy and detection rates of breast cancer are fundamentally dependent on the accuracy of mammographic interpretation. While existing literature has documented the PPVs of BI-RADS categories, this study aims to evaluate the PPVs specifically for BI-RADS 4 and 5 lesions and to elucidate the factors contributing to discrepancies between radiographic categorization and histopathological results.

Materials and methods

Study design and setting
The present study was a retrospective diagnostic accuracy study conducted at Srinagarind Hospital. This Hospital is a university hospital located in Khon Kaen. The study protocol was approved by the Center for Ethics in Human Research of Khon Kaen University. The study code was HE661158. Patient confidentiality was maintained by using study identification codes, and identifiable information was kept separately in secure files with restricted access.

Study patients
Inclusion Criteria:
Patients who underwent ultrasound-guided or tomosynthesis-guided breast biopsy with BI-RADS assessment of categories 4A, 4B, 4C, or category 5 at the study site during the period from January 2017 to December 2021

Exclusion criteria:
(1) Patients who did not receive histopathological results within 60 days of breast imaging at the study site.
(2) Patients whose histopathological results were unavailable or who had their biopsies performed elsewhere; or patients who had previously been diagnosed with breast cancer at the same site

Procedure
Breast imaging was performed using digital mammography and high-resolution ultrasound. All cases were serviced by one of seven board-certified radiologists at the institution, each possessing over five years of experience. The diagnostic team included three fellowship-trained breast radiologists and one breast imaging fellow. Prior imaging and clinical history were available should a radiologist request them.

THE ASEAN JOURNAL OF RADIOLOGY
ISSN 2672-9393

Each lesion was assigned a BI-RADS category (4A, 4B, 4C, or 5) based on morphological features, margins, calcification patterns, and other suspicious findings. In instances where a BI-RADS subcategory was not initially documented, a fellowship-trained radiologist performed a secondary review to assign the specific 4A, 4B, or 4C classification. All imaging interpretations were completely blinded to the histopathology results.

Histopathological sampling of breast tissue was performed by core-needle biopsy under ultrasonography-guided or tomosynthesis-guided biopsy, chosen based on the modality that provided the best lesion visibility. All ultrasonography-guided and tomosynthesis-guided biopsies were performed by the three radiologists who had been fellowship-trained. Possible pathological diagnoses are listed in Table 1.

Table 1. *Possible pathological diagnoses.*

Negative (Benign)	o Fibroadenoma o Benign phyllodes tumor o Proliferative disease without atypia o Negative for malignancy o Benign papillary neoplasm papillary lesion without atypia

Positive (Malignant)	o Proliferative disease with atypia
	o Atypical lobular hyperplasia (ALH)
	o Atypical ductal hyperplasia (ADH)
	o Non-invasive breast carcinoma
	  o Lobular carcinoma in situ (LCIS)
	  o Ductal carcinoma in situ (DCIS)
	o Invasive breast carcinoma
	  o Invasive ductal carcinoma
	  o Invasive lobular carcinoma
	  o Carcinoma with medullary features
	  o Mucinous carcinoma
	  o Tubular carcinoma

Statistical analysis

Diagnostic accuracy metrics included the positive predictive value (PPV) for BI-RADS 4 (overall and subcategories) and BIRADS 5, while using histological results as the gold standard. Exact 95% confidence intervals were calculated using the Clopper-Pearson method. All statistical analyses were conducted using STATA version 17.

Results

We enrolled the records of 1,666 patients who met the study criteria. The patients' ages ranged from 12 to 84 years old. There were 1,665 female patients and one male patient. The most common age group was 40-59 years old, encompassing 1,089 individuals, which accounted for approximately 65% of the patients in the present study.

Table 2. *Distribution of enrolled patients by age.*

Age range (years)	Patient (n)
< 19	7
20-29	82
30-39	205
40-49	554
50-59	538
60-69	219
70-79	55
> 80	6

Of the 1,666 breast lesions, 899 were in Category 4A, 492 in Category 4B, 149 in Category 4C, and 126 in Category 5. To evaluate the diagnostic accuracy of mammography at our institution in detecting breast cancer, Table 2 presents the PPV for each BI-RADS category and subcategories along with 95% confidence intervals (CI).

PPV increased with the severity of the BI-RADS category. The positive rate for PPV for BI-RADS 5 was 89.7%, whereas BI-RADS 4A had the lowest positive rate (PPV= 5.0%). The positive rates increased in a stepwise order from BI-RADS 4A to BI-RADS 5.

Table 3. describes the details of the PPVs of the present study's population, while Table 4. compares the observed positive rates of breast cancer in the present study with the expected likelihood according to BI-RADS 2013 guidelines. The observed positive rates for BI-RADS 4A (5.0%), 4B (19.5%), and 4C (57.0%) fell within the expected ranges outlined by the 2013 guidelines, indicating that the mammography assessments for these subcategories at our institution were consistent with the standard classification. However, the observed positive rate for BI-RADS 5 was 89.7%, which is slightly lower than the ≥ 95% likelihood suggested by BI-RADS 2013.

Table 3. *Agreement between BI-RADS categories and histopathological results.*

BI-RADS	# patients, n	Pathology result		Positive predictive value, (95% CI)
		Negative (n, %)	Positive (n, %)	
5	126	13 (10.3)	113 (89.7)	89.7% (83.0 – 94.4)
4C	149	64 (42.9)	85 (57.0)	57.0% (48.7 – 65.1)
4B	492	396 (80.4)	96 (19.5)	19.5% (16.1 – 23.3)
4A	899	854 (94.9)	45 (5.0)	5.0% (3.7 – 6.6)

Table 4. *Positive rates of breast cancer by BI-RADS category according to BI-RADS 2013.*

BI-RADS	BI-RADS 2013 likelihood of cancer	Observed positive rate (%)	Agreement between the observed rate and the expected likelihood
4A	Low suspicious for malignancy (>2% to <=10%)	5.0	Within the expected range
4B	Moderate suspicious for malignancy (>10% to <=50%)	19.5	Within the expected range
4C	High suspicious for malignancy (>50% to <=95%)	57.0	Within the expected range
5	Highly suggestive of malignancy (>=95%)	89.7	Lower than the expected likelihood

Table 5. summarizes the cases in which the histopathological findings were discordant with the imaging assessment for lesions categorized as BI-RADS 5. We focused on BI-RADS 5 because the observed positive rate was lower than the expected likelihood, thus highlighting this category as an area for improvement. For each case, patient demographics and clinical presentation, mammographic or ultrasound findings, and histopathological results are presented. The table also provides the reasons for the discordant diagnoses.

In the reported cases, discordance was primarily due to misinterpretation of imaging findings. Out of the twelve misinterpreted cases, ten were over-categorized as BI-RADS 5, when the imaging findings were more consistent with BI-RADS 4. These included cases with benign lesions such as fibroadenoma, fibrocystic changes, phyllodes tumors, and benign fibroepithelial lesions, in which certain clinical factors such as patient age, palpability, or interval change contributed to misinterpretation.

The last two misinterpreted cases were classified as BI-RADS 5 despite benign pathological results (angiolipoma with stromal fibrosis and lymphocytic mastitis with fibrotic stroma). Diagnosing these cases was challenging because benign conditions could mimic malignancy radiologically. The imaging findings of these two cases showed irregular spiculated margins, hyperdense masses, and suspicious axillary lymph nodes, which justified the BI-RADS 5 categorization. This misclassification to BI-RADS 5 of benign lesions was considered acceptable because fibrotic lesions are among the usual causes of false positives in BI-RADS 5.

Table 5. describes these twelve cases in the order presented above: nine cases of overcategorization of benign lesions, two cases of acceptable false positives from benign lesions, and one case of overcategorization but with a positive histopathological result.

Table 5. *Descriptions of cases with discordant diagnoses in BI-RADS category 5.*

Case No.	Demographics and Clinical presentation	Mammographic or ultrasound findings	Histopathological findings	Reasons for discordant findings
1	63-year-old female undergoing a workup for multiple organ metastases from a primary tumor	-Mammography: Suspicious segmental/linear calcifications at the 4 to 7 o'clock position of the right breast - Ultrasonography: An irregular-shaped, non-circumscribed margin, hypoechoic mass corresponding to the area of abnormal calcifications on mammography.	US-CNB: Dense fibrotic tissue without terminal ductal lobular unit. No malignancy.	The observed segmental/linear calcifications demonstrate suspicious morphology and distribution and should have been categorized as BI-RADS 4C.
2	58-year-old female with undifferentiated right breast cancer, post modified radical mastectomy, with detection of a new palpable irregular mass at the 2 o'clock position of the left breast	- Mammography: A group of amorphous calcifications suspected at the upper outer quadrant of the left breast. - Ultrasonography: A new irregular-shaped, lobulated margin hypoechoic mass corresponding to the area of abnormal calcifications on mammography.	US-CNB: Fibrotic breast tissue with unremarkable terminal ductal lobular units, no malignancy. Non-lactating effect tissue contained a group of suspicious calcification. Surgical excision: Foci of sclerosing adenosis with extensive intraluminal calcification. No malignancy.	The observed abnormal group of amorphous calcifications demonstrated suspicious morphology and distribution and should have been categorized as BI-RADS 4B.
3	43-year-old female with a known history of fibrocystic breast disease	- Mammography: No suspicious abnormalities detected. - Ultrasonography: A new irregular-shaped hypoechoic mass at the 2 o'clock position of the left breast.	US-CNB: Focal adenosis with apocrine metaplasia and increased fibro collagenous stroma with an area of fibrocystic change, no definite malignancy identified.	An irregularly shaped mass without calcifications should be classified as BI-RADS 4B.

Case No.	Demographics and Clinical presentation	Mammographic or ultrasound findings	Histopathological findings	Reasons for discordant findings
4	42-year-old female with a palpable mass located at the 10 o'clock position of the right breast	- Mammography: No suspicious abnormalities detected. - Ultrasonography: Interval growth of a macrolobulated mass with peripheral vascularity at the corresponding location, now 3.2 x 1.6 cm (previously 2.4 x 1.5 cm).	US-CNB: Fibroepithelial lesion, suggestive of fibroadenoma.	- The sonographic findings of a solid, hypoechoic mass with a macrolobulated margin correspond with BI-RADS 4A-B. - Prior ultrasounds showed variability in the reported size of the right mass at the corresponding site. These fluctuations most likely represented measurement variability rather than a true change and could have contributed to the overcategorization.
5	67-year-old female with a palpable mass located at the 12 o'clock position of the right breast	- Mammography: A 3.6 cm isodense mass with popcorn-like macrocalcifications, corresponding to the palpable area. - Ultrasonography: An oval-shaped, hypoechoic mass with internal macrocalcifications at the same location	US-CNB: Initially revealed benign breast tissue, negative for malignancy, with equivocal findings of microcalcifications. A repeated biopsy confirmed benign breast tissue, with stromal microcalcifications.	Benign morphology involving fibroadenoma (typically BI-RADS 2) could justifiably be upgraded to BI-RADS 4A based on age and clinical factors and the lack of prior imaging to confirm stability, but should not have been upgraded to BI-RADS 5.
6	64-year-old female with a palpable mass located at the 12 o'clock position of the right breast	- Mammography: Typical popcorn-like calcification without an associated soft tissue mass at the corresponding position. - Ultrasonography: An oval-shaped, heterogeneous echoic mass with internal macrocalcifications at the same site.	US-CNB: Sclerotic fibroadenoma with stromal calcification, no malignancy.	Benign morphology involving fibroadenoma (BI-RADS 2) was graded as BI-RADS 4A based on age and clinical factors, and the lack of prior imaging to confirm stability. This justified an upgrade to a low-suspicion category.
7	47-year-old female with enlarging palpable mass in the right breast at the 6 o'clock position	- Mammography: A large, well-circumscribed, and hyperdense mass corresponding to the palpable area. - Ultrasonography: A large heterogeneous echogenic mass with internal cystic changes at the same site	US-CNB: Fibroepithelial lesion Excisional biopsy: A benign phyllodes tumor, measuring about 11cm.	A growing, palpable, and large, well-circumscribed, and hyperdense mass with complex cystic features should be categorized as BI-RADS 4B or 4C due to the absence of frank malignant features.

Case No.	Demographics and Clinical presentation	Mammographic or ultrasound findings	Histopathological findings	Reasons for discordant findings
9	54-year-old female with a palpable mass at the 12 o'clock position of the left breast	- Mammography: A focal asymmetry at the palpable area without associated calcification. - Ultrasonography: An indistinct margin, isoechoic mass without posterior acoustic features or abnormal vascular flow at the same site.	US-CNB: Fibrocystic change, no malignancy	An indistinct margin, isoechoic mass corresponding to a palpable focal density on mammography. The mass showed no posterior features or abnormal vascularity. These findings warrant a BI-RADS 4B categorization.
10	64-year-old female with a palpable mass located at the 9 o'clock position of the right breast	- Mammography: A new circumscribed hyperdense mass identified at the corresponding site. - Ultrasonography: A hypoechoic mass with angular margins identified in the corresponding location.	US-CNB: Invasive ductal carcinoma, not otherwise specified	The sonographic findings of a solid, hypoechoic mass with angular margins corresponded with the palpability and mammographic abnormality. These findings should have been categorized as BI-RADS 4C.
11	61-year-old female with a history of left breast cancer, post left modified radical mastectomy, undergoing screening mammography of the right breast	- Mammography: A new irregularly shaped, hyperdense mass with spiculated margin, but without internal calcification at the 12 o'clock position of the right breast. - Ultrasonography: An irregularly shaped, heterogeneous echogenic mass measuring about 1.1 cm at the same site.	US-CNB: Benign breast tissue with increased fibrotic stroma. Excisional biopsy: Angiolipoma with stromal fibrosis.	- An irregularly shaped, hyperdense mass with a spiculated margin is highly suspicious for malignancy. - Benign fibrotic lesions can mimic malignancy and are among the benign lesions that warrant BI-RADS 5 categorization.
12	72-year-old female with a palpable mass at the axillary tail of the right breast	- Mammography: Two irregularly shaped, hyperdense masses with spiculated margins but without internal calcification at the upper outer quadrant of the right breast. - Ultrasonography: Two contiguous, irregularly shaped, and heterogeneously echogenic masses at the same site, corresponding to the findings on mammography, with associated enlarged right axillary lymph nodes.	US-CNB: Fibroadipose tissue with chronic inflammation. Wide excisional biopsy: Focal lymphoid infiltration with fibrotic stroma, suggestive of lymphocytic mastitis.	- Irregularly shaped hyperdense masses with spiculated margins and associated lymphadenopathy are highly suspicious for malignancy and warrant a BI-RADS 5. - Benign inflammation lesions with fibrosis can mimic malignancy and are among the benign lesions that warrant BI-RADS 5 categorization.

US-CNB: Ultrasound-guided core needle biopsy technique.

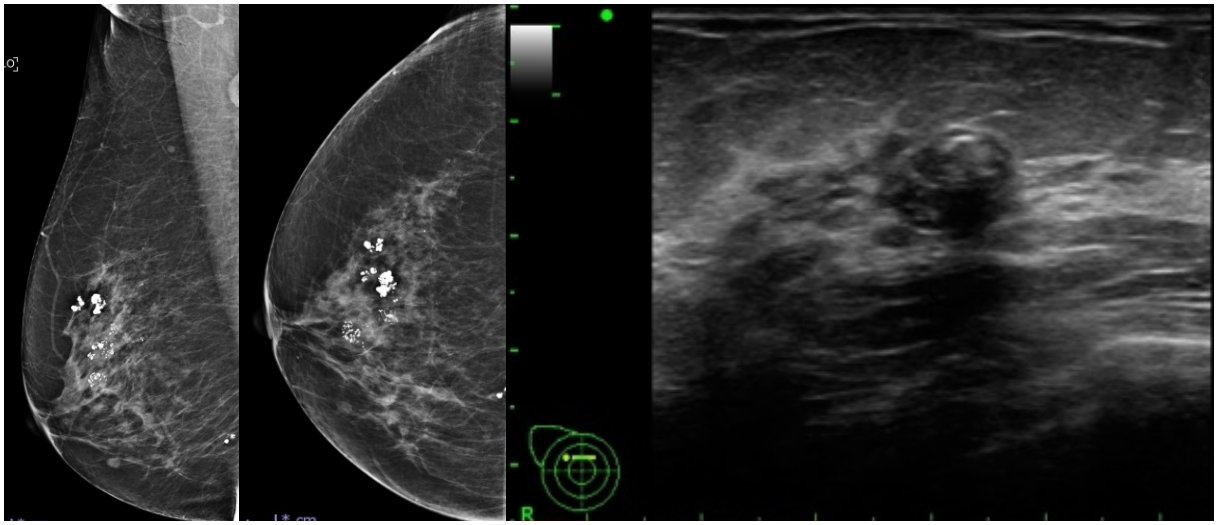

Figure 1. *Images from case no. 6 show an overcategorization to BI-RADS 5 of a calcified lesion which should have been at most BI-RADS 4A.*

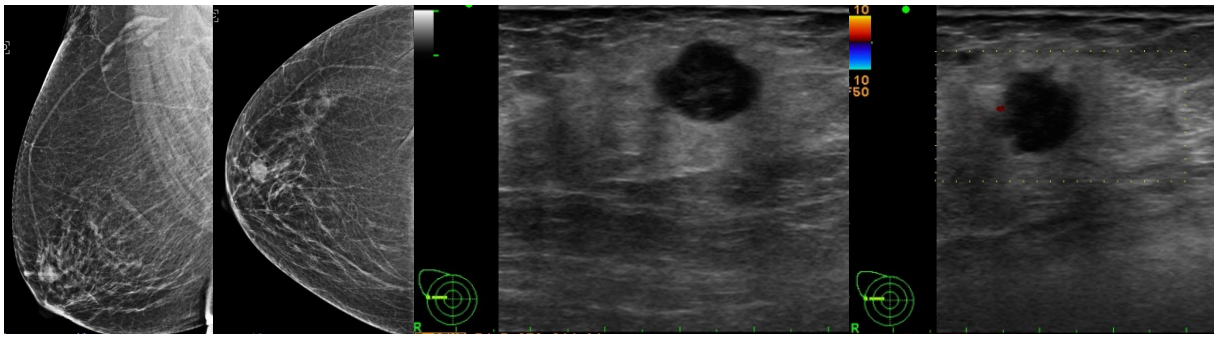

Figure 2. *Images from case no. 10 show an overcategorization to BI-RADS 5 of a non-calcified lesion which should have been at most BI-RADS 4A.*

Figure 3. *Images from case no. 11 show a benign fibrotic mass with malignant features, which correctly warranted a BI-RADS 5 categorization.*

Discussion

The present study found that the observed positive rates were mostly in agreement with the BI-RADS 2013 recommendation, except for the BI-RADS 5 category, which showed overcategorization. This overcategorization happened due to 1) benign masses with associated calcification, 2) inadequacies in lesion measurement or technical limitations, 3) fibrosis changes mimicking malignancy, and 4) overcalling a benign-looking mass that turned out to be cancerous.

Similar to some previous studies in Thailand [8-10], the present study highlighted the risk of overcategorization and its clinical consequences. Enhanced radiologic-pathologic correlation, cautious use of BI-RADS 5, and adherence to standardized criteria may help optimize diagnostic accuracy and reduce unnecessary interventions.

On the other hand, the recognition that a small proportion of BI-RADS 5 lesions may yield benign pathology is inevitable. The present study describes two cases of acceptable false positive BI-RADS 5 categorizations. Thus, the awareness that some BI-RADS 5 patients do not have malignancy is crucial to avoid repeated investigations.

Another possible explanation for the low observed positive rate in BI-RADS 5 cases was that we only included patients who underwent biopsies by radiologists, whereas patients with frank, palpable masses and thus higher likelihoods of cancer had been biopsied by surgeons.

Various studies have similarly shown overcategorization [8-11] while some others have shown under-categorization [12, 13]. This shows that there is still a need for continuous quality improvement and breast imaging practice and training, with awareness and considerations for local factors that contribute to the discordance.

The strengths of the present study include a detailed evaluation of BI-RADS 4 subcategories and an exploration of causes of overdiagnosis in BI-RADS 5 lesions. Limitations include the exclusion of biopsies performed by surgeons and the retrospective nature of the study. Future research should focus on refining imaging criteria to improve specificity and further evaluating challenging entities such as masses with calcifications or lesions with inadequate measurement. The addition of other imaging modalities and their effects on diagnostic accuracy can prove to be a fruitful direction for future research as well.

Conclusion

In the present study, the PPVs for BI-RADS 4 lesions were within the expected range, whereas for BI-RADS 5 lesions, the PPV was 89%, which is slightly lower than the expected likelihood. Overcategorization was responsible for most of the discordant cases. Continuous auditing and updating of mammographic accuracy remain essential to enhance early detection and reduce breast cancer mortality.

References

1. World Health Organization [Internet]. Geneva: WHO; c2026 [cited 2026 May 7]. Breast cancer. 16 April 2026. Available from: https://www.who.int/news-room/fact-sheets/detail/breast-cancer

2. The National Cancer Institute. Bangkok: NCI; 2023 [cited 2026 May 7]. [Hospital-based cancer registry 2023]. Thai. Available from: https://nci.go.th/files/cancer_stat/1771317685_file.pdf

3. Duffy S, Vulkan D, Cuckle H, Parmar D, Sheikh S, Smith R, et al. Annual mammographic screening to reduce breast cancer mortality in women from age 40 years: Long-term follow-up of the UK Age RCT. Health Technol Assess 2020;24:1-24. doi: 10.3310/hta24550.

4. van Schoor G, Moss SM, Otten JD, Donders R, Paap ED, den Heeten GJ, et al. Increasingly strong reduction in breast cancer mortality due to screening. Br J Cancer 2011 ;104:910-4. doi: 10.1038/bjc.2011.44.

5. Myers ER, Moorman P, Gierisch JM, Havrilesky LJ, Grimm LJ, Ghate S, et al. Benefits and harms of breast cancer screening: A systematic review. JAMA 2015;314:1615-34. doi: 10.1001/jama.2015.13183.

6. D'Orsi CJ, Sickles EA, Mendelson EB, Morris EA. 2013 ACR BI-RADS® Atlas, breast imaging reporting and data system. 5th ed. Reston (VA): American College of Radiology; 2014.

7. Mello JM RB, Bittelbrunn FP, Rockenbach MABC, May GG, Vedolin LM, Kruger MS, et al. Breast cancer mammographic diagnosis performance in a public health institution: a retrospective cohort study. Insights Imaging 2017;8:581-8. doi: 10.1007/s13244-017-0573-2.

8. Wiratkapun C, Lertsithichai P, Wibulpholprasert B. Positive predictive value of breast cancer in the lesions categorized as BI-RADS category 5. J Med Assoc Thai2006;89: 1253-9.

9. Sirikunakorn P, Marukatat N, Tangjitgamol S, Loharamtaweethong K. Positive predictive value of malignancy in BI-RADS 4 and 5 breast lesions. Vajira Med J [Internet]. 2014 [cited 2026 May 7];58(2):1-11. Available from: https://he02.tci-thaijo.org/index.php/VMED/article/view/23777/20225

10. Wongmaneerung P, Somwongprasert A, Watcharachan K, Ditsatham C. Positive predictive value of BI-RADS 4 and 5 mammography in patients with non-palpable breast mass. Thai J Surg [Internet]. 2015 [cited 2026 May 7];36:116-9. Available from: https://he02.tci-thaijo.org/index.php/ThaiJSurg/article/view/226161

11. Ghunaim HA, Alatawi RE, Borhan WM, Daqqaq TS, Alhasan AS, Aboualkheir MM, et al. Accuracy of imaging of BI-RADS 4 subcategorizations in breast lesion diagnosis: Radiologic-pathologic correlation. Saudi Med J 2024;45:1228-37. doi: 10.15537/smj.2024.45.11.20240001.

12. Ghaemian N, Haji Ghazi Tehrani N, Nabahati M. Accuracy of mammography and ultrasonography and their BI-RADS in detection of breast malignancy. Caspian J Intern Med 2021;12:573-9. doi: 10.22088/cjim.12.4.573.

13. Mohapatra SK, Das PK, Nayak RB, Mishra A, Nayak B. Diagnostic accuracy of mammography in characterizing breast masses using the 5th edition of BI-RADS: A retrospective study. Cancer Res Stat Treat [Internet]. 2022 [cited 2026 May 7];5:52-8. Available from: https://journals.lww.com/crst/fulltext/2022/05010/diagnostic_accuracy_of_mammography_in.9.aspx

Case Report

A malignant mimicker: Endometriosis presenting as a large solid–cystic pelvic mass with lymphadenopathy and distal ureteral invasion

Payia Chadbunchachai, M.D.
Kulyada Eurboonyanun, M.D.
Wichien Sirithanaphol, M.D.
Pochchara Tangpaisarn, M.D.
Sasithorn Watcharadetwittaya, M.D.

From Department of Radiology, Faculty of Medicine, Khonkaen University, Khonkaen, Thailand.

Address correspondence to P.C. (email: Payich@kku.ac.th)

Received 26 September 2024; revised 13 January 2026; accepted 22 April 2026
doi:10.46475/asean-jr.v27i2.926

Introduction

Endometriosis presents with various imaging features. The most common site of endometriosis is the ovary, followed by the pelvic peritoneum. Less frequently affected sites include the deep subperitoneal tissues, the gastrointestinal tract, the urinary bladder, the thorax, and subcutaneous tissues.

We present a rare case of endometriosis with atypical symptoms and radiographic features. The patient initially presented with hematuria. Evaluation revealed a pelvic mass with skip lesions extending to the distal ureter, mimicking malignancy. Focal endometriosis in the right external iliac region resembled nodal metastasis. These findings led clinicians and radiologists to suspect a malignant process. Consequently, endometriosis should be considered in the differential diagnosis under specific circumstances.

Keywords: Carcinoma, Endometrioma, Endometriosis, Hematuria, Ureteritis, Ureteric invasion.

THE ASEAN JOURNAL OF RADIOLOGY
ISSN 2672-9393

Introduction

Endometriosis is a common benign disease among women, particularly during their reproductive years, affecting approximately 10% of the female population [1]. One proposed theory suggests that endometriosis results from the retrograde flow of endometrial tissue through the fallopian tubes during menstruation. Endometriosis may occur within the pelvic cavity and involve pelvic organs such as the ovaries (endometriomas), uterosacral ligaments, rectosigmoid colon, abdominal wall, peritoneum, or urinary tract, consistent with deep endometriosis [1,2].

While urinary tract endometriosis is rare, accounting for approximately 1-2% of all cases of endometriosis. The urinary bladder is the most common site of involvement within the KUB system [3]. Ureteral involvement is uncommon; when present, it may result in hydronephrosis and hydroureter [2]. Imaging modalities such as ultrasonography (US), computed tomography (CT) and magnetic resonance imaging (MRI) play crucial roles in identifying the cause of hydronephrosis and characterizing pelvic masses. However, a definitive diagnosis requires histologic confirmation obtained through intervention [2]. In this report, we present a case of ureteral endometriosis presenting with hematuria, evaluated using multimodality imaging, and confirmed by histopathological examination, which guided the diagnosis and management.

Case summary

A 46-year-old woman with no underlying disease or history of medication use presented with persistent hematuria for 10 days and right lower abdominal pain. She denied any prior similar symptoms, dysuria, or abnormal urine color. Physical examination revealed no palpable abdominal mass or fever. The patient had a history of a previous transabdominal hysterectomy for the removal of a large uterine myoma at another hospital. However, information regarding the pathological findings from the previous operation was unavailable.

The patient was initially diagnosed with a urinary tract infection, based on urinalysis demonstrating a white blood cell count of approximately 10-20 cells per high-power field (HPF), and was prescribed Ofloxacin for three days; however, her symptoms did not improve. Subsequent bedside ultrasonography revealed severe right hydronephrosis and right hydroureter extending to the ureterovesical junction. The patient was then referred to a gynecologist. Transvaginal sonography demonstrated a multiloculated hypoechoic complex cystic mass measuring approximately 4.5×4.7 cm in the left adnexa (Figure 1A), accompanied by a heterogeneous solid mass measuring approximately 3.4×2.4 cm (Figure 1B), with an additional suspicious solid mass in the cul-de-sac shown in Figure 1C.

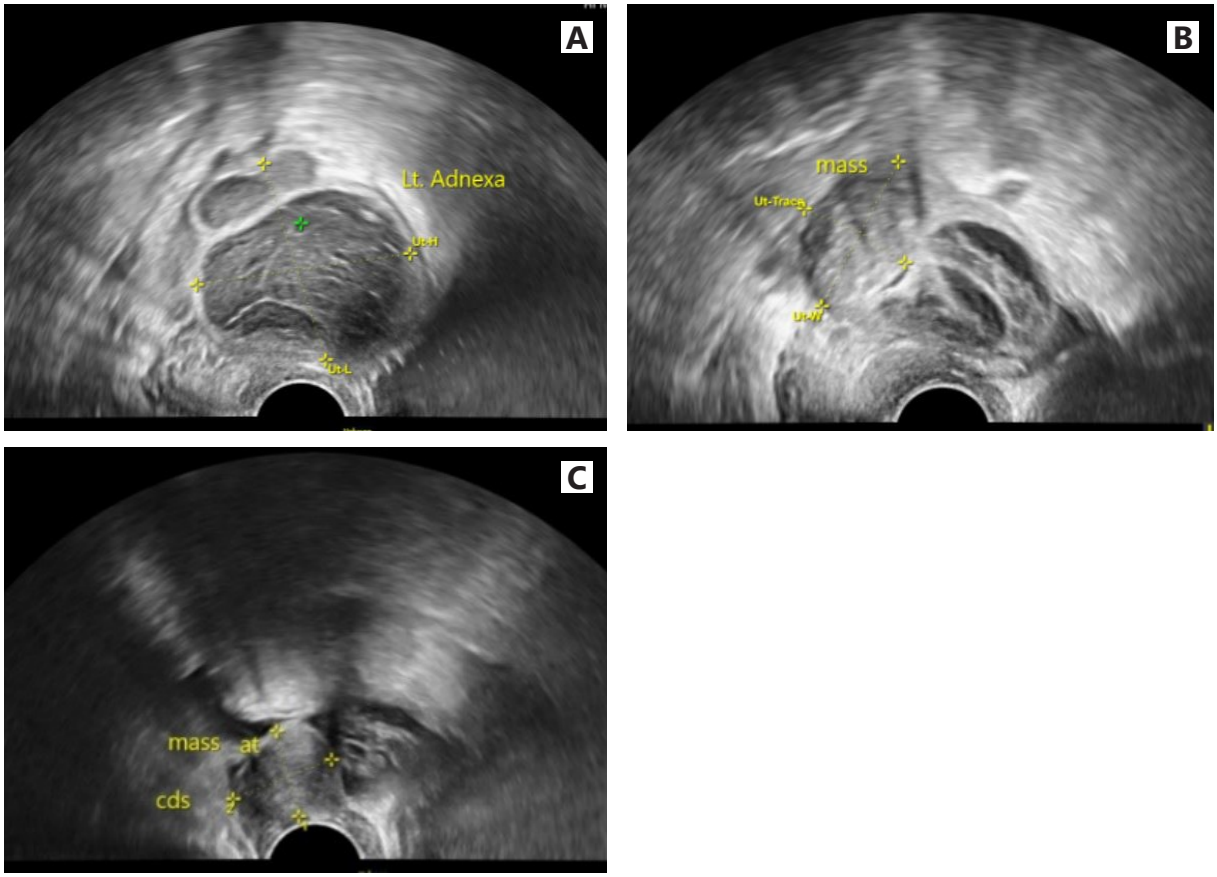

Figure 1. *Transvaginal sonography. Sagittal ultrasound images demonstrate a multiloculated hypoechoic complex cystic mass in the left adnexa measuring 4.5 x 4.7 cm (A), with an associated solid component measuring 3.4 x 2.4 cm (B), and an additional suspicious solid mass in the cul-de-sac (C).*

Further CT urography (Figures 2A and 2B) revealed an 8.2 x 6.3 x 8.3 cm complex solid-cystic mass with enhancement of the solid component, predominately located in the left pelvic cavity, consistent with the previous ultrasound findings. The lesion involved bilateral pelvic sidewalls and extended to the mesorectal region (arrows in Figures 2A and 2B). Minimal ascites was also observed in the perirectal region (asterisk in Figure 2B). The mass involved the right parametrium and invaded the right distal ureter, resulting in severe right hydronephrosis. It also abutted the left distal ureter (arrows in Figure 2C), causing mild left hydronephrosis and hydroureter (Figure 2D). In addition, an ill-defined, heterogeneous, enhancing mass measuring approximately 2.7x1.7 cm was identified in the right external iliac region, in contact with the right external iliac vessels (Figure 2E), resembling a pathologic lymph node. Malignancies such as ovarian cancer, endometrial cancer, or transitional cell carcinoma of the urinary tract with metastatic lymphadenopathy were therefore suspected.

Figure 2. *Conventional CT of the whole abdomen. (A) shows a non-contrast axial image of the pelvic cavity, and (B) depicts the post-contrast study, revealing an irregular, heterogeneous, enhancing complex solid-cystic mass. The mass involves the bilateral distal ureters (C), resulting in right hydronephrosis and mild left hydronephrosis (D). Another heterogeneous enhancing mass is noted along the right pelvic side wall (E).*

The patient underwent pelvic MRI for further evaluation of the mass (Figure 3). MRI demonstrated the same complex solid-cystic mass previously seen on ultrasound and CT in the pelvic cavity, with dark signal intensity of the solid component on T2-weighted (T2W) images, and areas of susceptibility artifact (arrows in Figures 3A and 3B). Portions of the solid component showed high signal intensity on T1 fat-saturation (T1FS) image (arrow in Figure 3C). Peripheral blooming susceptibility artifact was observed on T2 gradient echo (GRE) sequence. Post-contrast subtraction images revealed enhancement of the posterior solid component (asterisk in Figure 3D); however, there was no evidence of restricted diffusion (arrows in Figures 3E and 3F).

Consistent with the prior CT findings, the heterogeneous enhancing mass in the right external iliac region demonstrated low signal intensity on the T2W image (arrows in Figure 3G), with areas of high signal intensity on the T1FS image representing hemorrhagic component (asterisk in Figure 3H). The lesion showed minimal enhancement on the post-contrast T1FS subtraction image (Figure 3I). The coronal T2W image demonstrated involvement of the right distal ureter, with associated right distal hydroureter (Figure 3J).

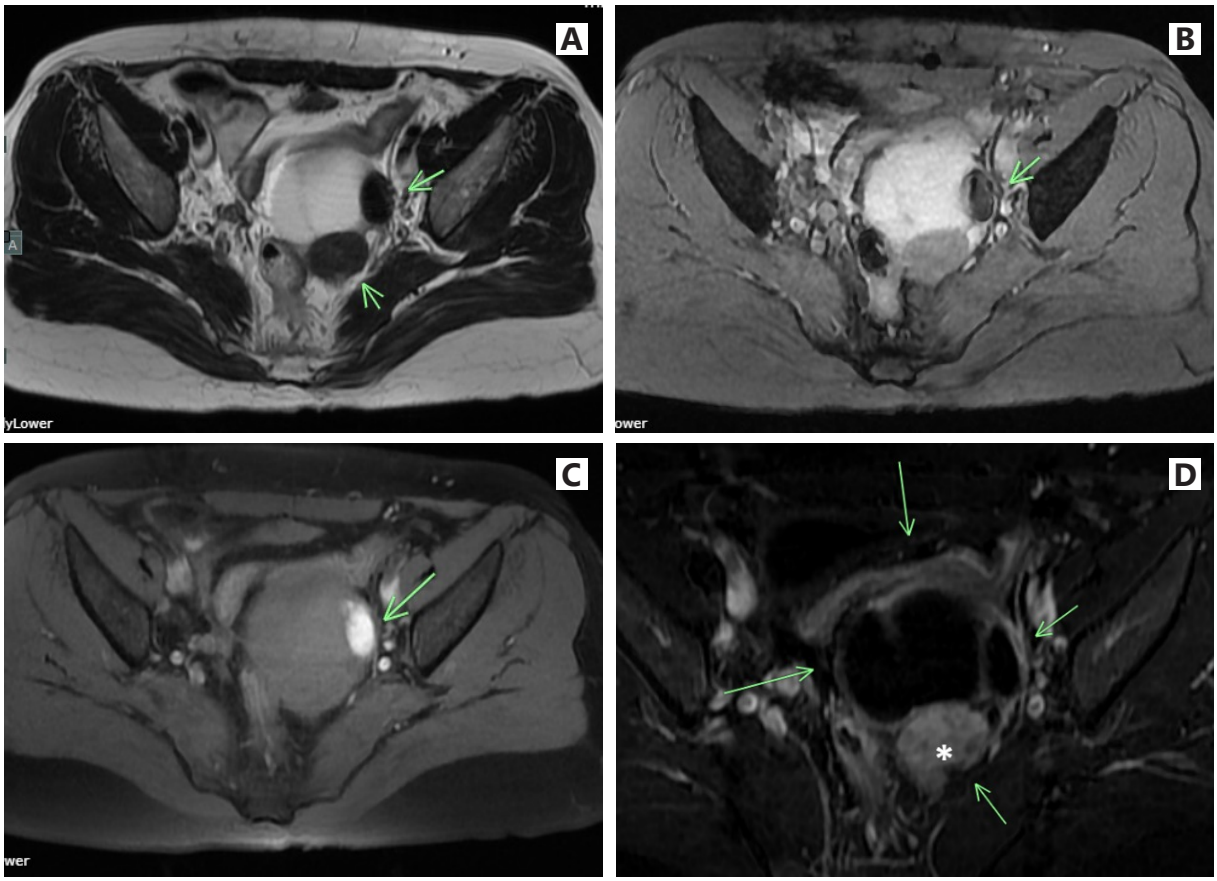

THE ASEAN JOURNAL OF RADIOLOGY
ISSN 2672-9393

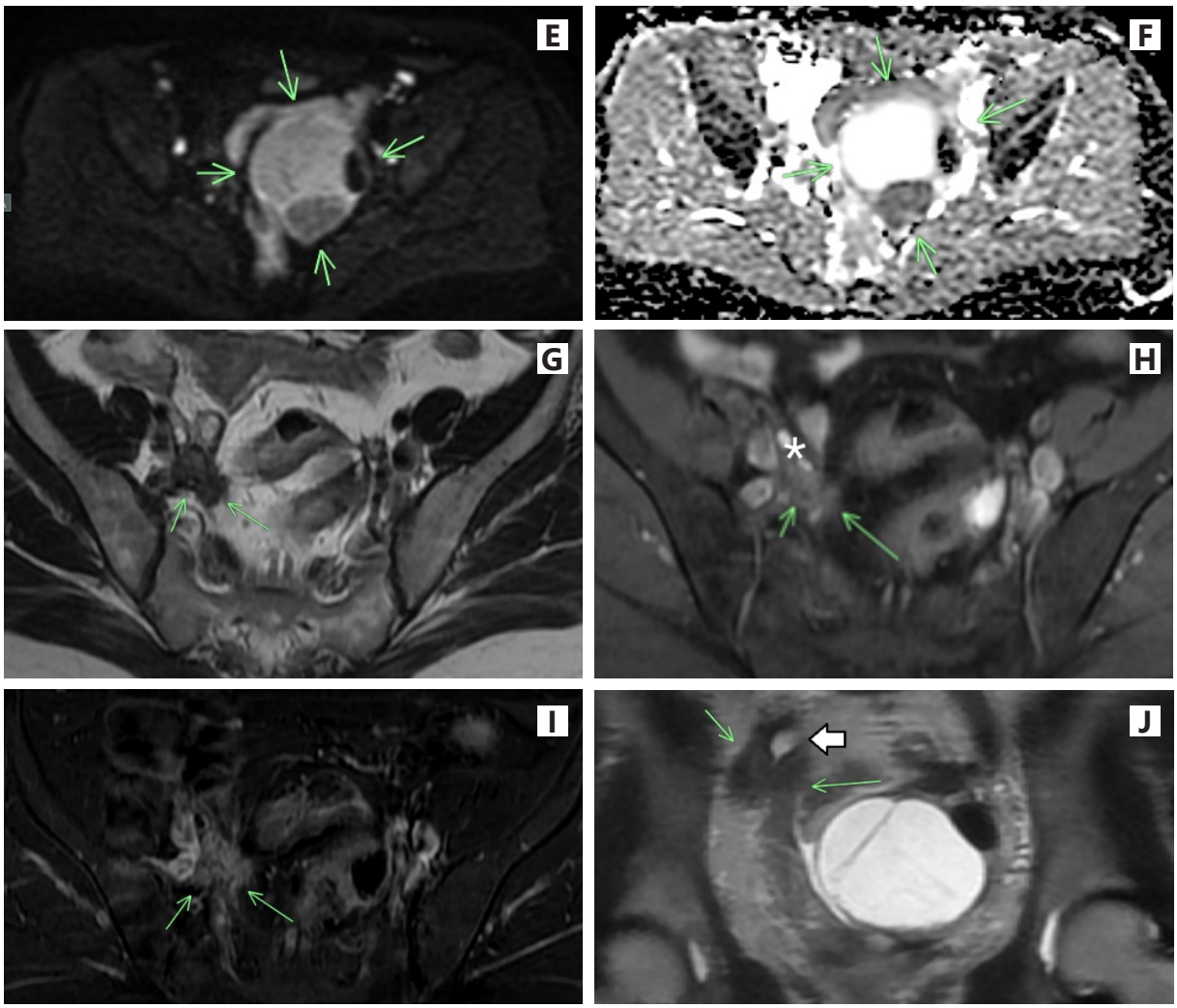

Figure 3. *A 1.5 Tesla MRI scan of the pelvic cavity revealed a complex solid-cystic mass with dark signal intensity (SI) on T2-weighted imaging (T2WI) of the solid component (A). Signal voids were observed within portions of the solid component on the gradient-echo (GRE) image (arrow in (B)). The T1-weighted fat saturation (T1FS) image demonstrated areas of hyperintense signal within the mass. A focal enhancing solid component was identified on post-contrast images (asterisk in (D)); however, there was no evidence of restricted diffusion on diffusion-weighted imaging (DWI, b=800) (E) or on the apparent diffusion coefficient (ADC) map (F). An additional irregular, spiculated, heterogeneous lesion demonstrated intermediate-to-low SI on the T2W image (G) and intermediate SI on the T1FS image, with foci of high signal intensity on the T1FS image suggestive of hemorrhagic components (asterisk in (H)). This lesion showed minimal enhancement on the post-contrast T1FS subtraction image (I), with evidence of right distal ureter involvement on the coronal T2W image (J).*

Further evaluation by a urologist included cystourethroscopy for double-J stent placement, which revealed a well-defined endoluminal filling defect within the right distal ureter, measuring approximately 2-3 cm in length and located about 3 cm from the right ureteral orifice (Figure 4). Partial laser resection of the mass was performed, and histopathological examination confirmed the diagnosis of endometriosis (Figures 5 and, 6).

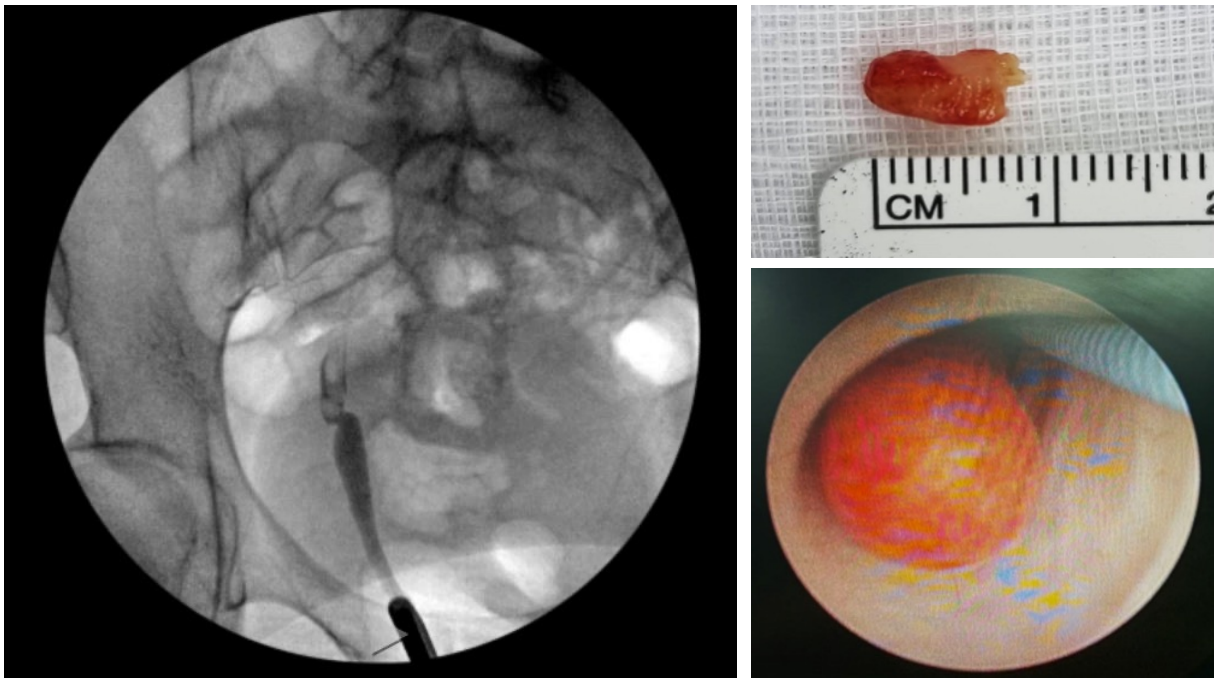

Figure 4. *Retrograde pyelography shows an intraluminal filling defect within the right distal ureter.*

The tissue biopsy obtained from the right ureter showed a small polypoid lesion with denuded surface epithelium and small hemorrhagic foci. The structure consisted of tubular-shaped glands lined by columnar epithelial cells and stroma resembling endometrium tissue (Figure 5). The diagnosis of ureteric endometriosis was confirmed by immunohistochemical staining for CK7, CK20, PAX-8, CD10, ER, and PR (Figure 6).

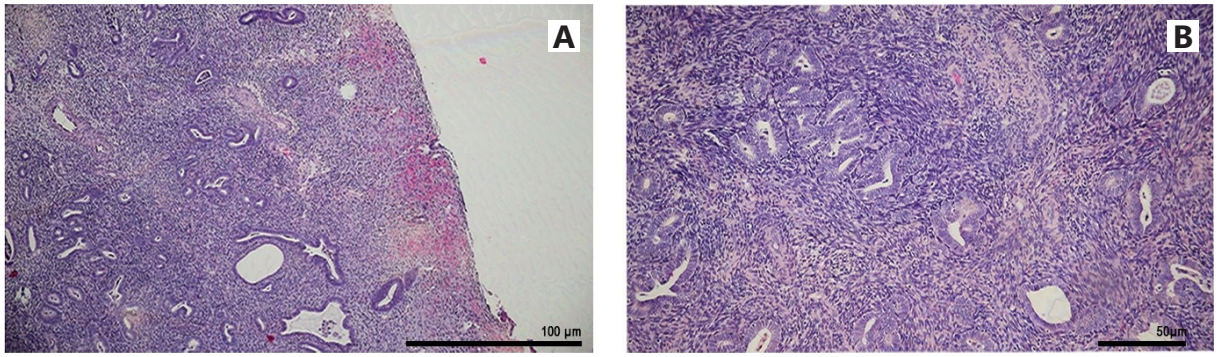

Figure 5. *The histopathological examination (A and B) reveals a polypoid tissue with a denuded surface and scattered hemorrhage. The lesion is composed of endometrial glands and stroma, along with hyalinized blood vessels. The specimen does not contain a muscle layer (Hematoxylin and eosin stain; x100 and x200).*

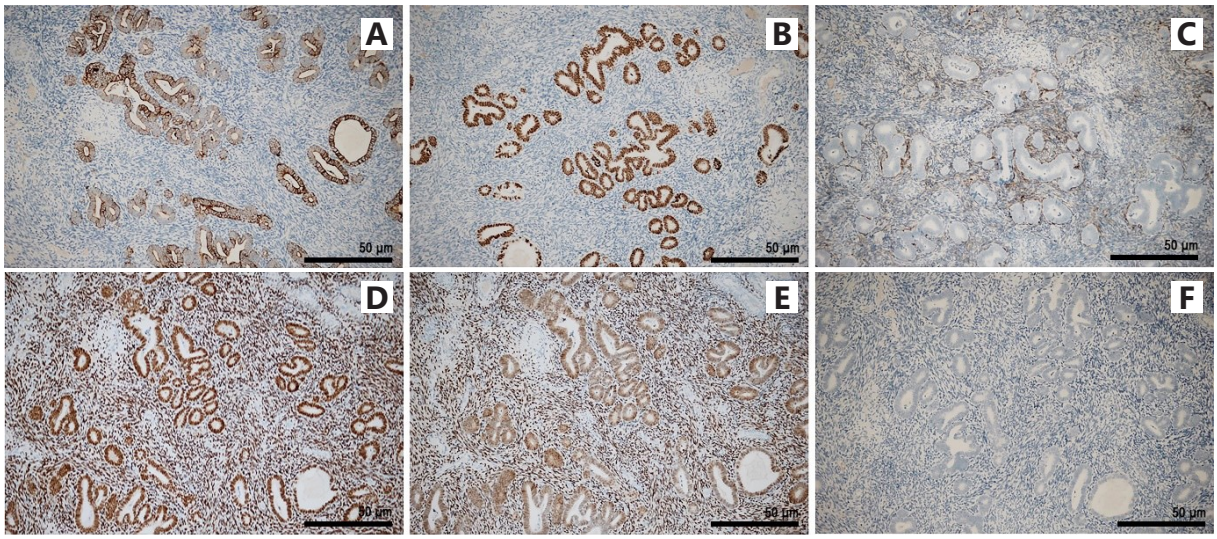

Figure 6. *Immunohistochemistry reveals that CK7 (A) and PAX-8 (B) highlight the endometrial glands. CD10 exhibits cytoplasmic staining specifically in the stromal cells (C). The estrogen receptor (ER) (D) and progesterone receptor (PR) (E) are positive in both the endometrial glands and stroma. CK20 shows negative staining (F).*

The patient was diagnosed with ureteral endometriosis with an associated endometrioma and was treated with a gonadotropin-releasing hormone (GnRH) agonist. A baseline MRI of the pelvic cavity was performed before treatment. A follow-up MRI after hormonal therapy revealed a reduction in the size of the complex solid-cystic mass within the pelvic cavity (Figure 7).

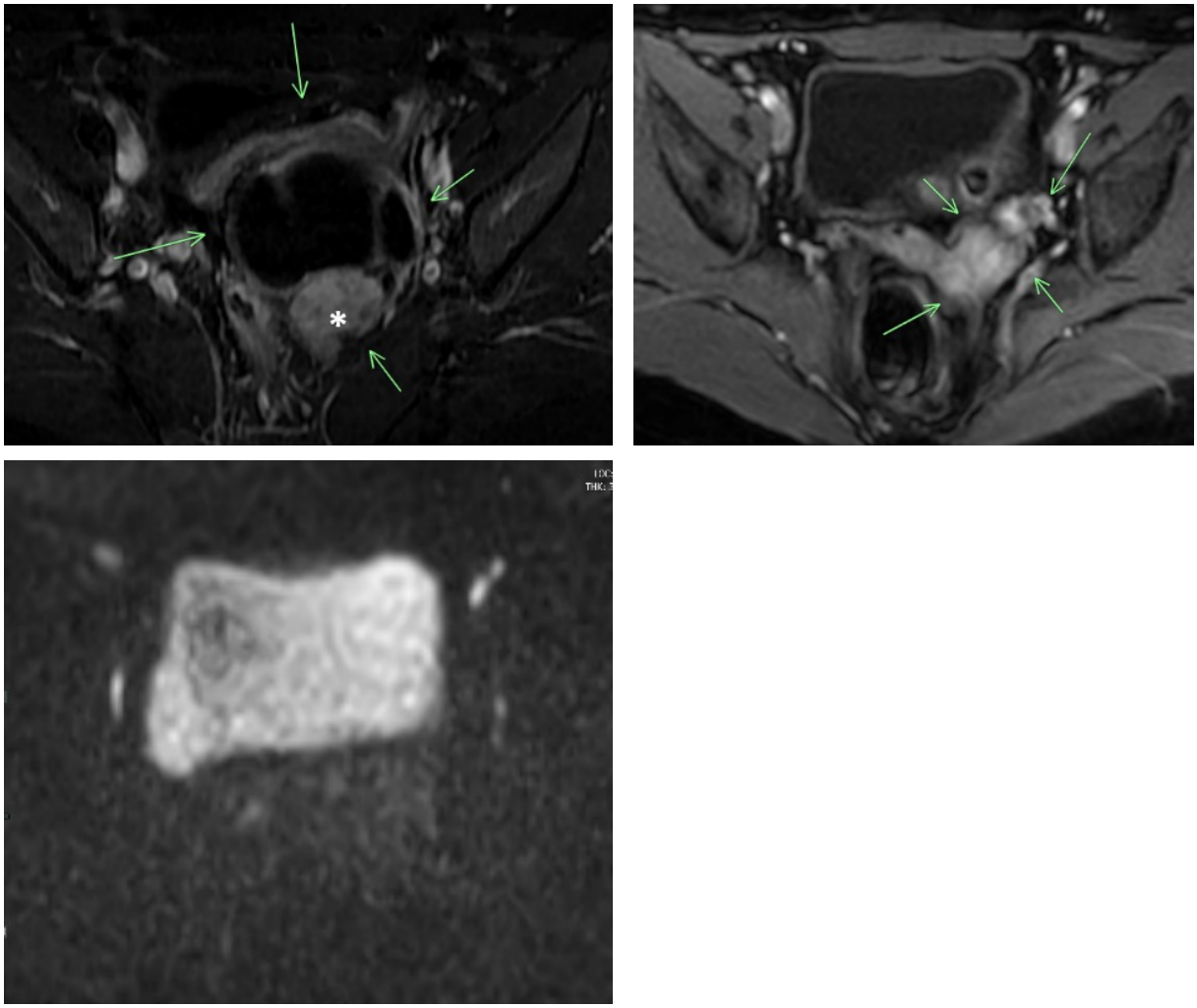

Figure 7. *1.5 Tesla MRI scan of the pelvic cavity. Before treatment with GnRH (A), a complex pelvic mass was observed. After treatment, there was, an interval decrease in size, with a residual enhancing solid component in the left pelvic cavity on the post-contrast subtraction image (B). There is no evidence of restricted diffusion (DWI B=800) within the enhancing solid nodule (C).*

THE ASEAN JOURNAL OF RADIOLOGY
ISSN 2672-9393

Discussion

This case illustrates a heterogeneous mass involving the right distal ureter and a complex solid-cystic mass in the left adnexa. The lesion caused architectural distortion and an irregular intraluminal filling defect of the right distal ureter on retrograde pyelography, along with an irregular mass observed on conventional CT and MRI imaging. Evidence of ureteral obstruction, including hydronephrosis and hydroureter, was also noted on the CT study. These imaging findings are more likely to be misinterpreted as urothelial neoplasia.

Pathological examination of a surgical biopsy from the intraluminal filling defect revealed endometriosis. Ureteral endometriosis is relatively uncommon, accounting for approximately 1% of all endometriosis cases [1]. It can be divided into extrinsic and intrinsic ureteral endometriosis based on the depth of ureteral wall infiltration. Extrinsic ureteral endometriosis, the more common form, involves invasion of the adventitia or periureteral tissues, whereas intrinsic ureteral endometriosis is confined to the muscularis and/or mucosa of the ureter wall [4].

Retrospective evaluation of the pyelography of this case suggested intrinsic ureteral endometriosis, as indicated by the presence of an irregular mucosal lesion in the right distal ureter. However, this finding may have been influenced by inadequate tissue sampling, as pathological analysis did not show evidence of muscular involvement [4].

Regarding the complex solid-cystic mass in the left pelvic cavity, it appeared as a large cystic lesion with focal hyperintensity on T1W images and hypointensity on T2W images, consistent with the T2 shading sign. These imaging features are characteristic of an endometrioma, suggesting ovarian endometriosis. In addition, these findings raise the possibility of deep endometriosis involving the surrounding pelvic structures [5].

Additionally, the areas of enhancement observed on imaging may be attributable to inflammation, fibrosis, granulation tissue, or fibromuscular hyperplasia surrounding ectopic endometrial glands. In this case, the likelihood of malignancy is lower because the enhancing lesion does not demonstrate restricted diffusion [1,2].

For this case, because biopsy confirmed endometriosis and the follow-up MRI after gonadotropin-releasing hormone (GnRH) agonist therapy showed a reduction in the size of the suspicious mass, endometriosis is the most likely diagnosis. According to an

article by Aki et al., the response of endometriosis to hormonal therapy, such as GnRH agonists, is not uniform. A good response is generally observed in cases of endometriosis that do not exhibit T2 shading [6]. As observed in this case, portions of the lesion demonstrating T2 shading remained visible on post-treatment imaging, whereas other components showed a decrease in size.

However, follow-up MRI still revealed some solid components, and although no definite restricted diffusion was observed on DWI images, ongoing clinical and imaging surveillance is recommended to monitor for potential malignant transformation [1,2].

Disclosure instructions

Clinical information, baseline data, and imaging studies were obtained from the medical records and the Picture Archiving and Communication System (PACS) at Srinagarind Hospital, Khonkaen University, Thailand.

During the preparation of this manuscript, the author used ChatGPT to assist with grammatical correction and to improve sentence structure, clarity, and coherence. Following the use of this tool, the author reviewed and edited the content as necessary and takes full responsibility for the integrity and accuracy of the publication.

THE ASEAN JOURNAL OF RADIOLOGY
ISSN 2672-9393

References

1. Takeuchi M, Matsuzaki K, Harada M. Endometriosis, a common but enigmatic disease with many faces: current concept of pathophysiology, and diagnostic strategy. Jpn J Radiol 2024;42:801–19. doi: 10.1007/s11604-024-01569-5.

2. VanBuren W, Feldman M, Shenoy-Bhangle AS, Sakala MD, Young S, Chamie LP, et al. Radiology state-of-the-art review: Endometriosis imaging interpretation and reporting. Radiology 2024 ;312:e233482. doi: 10.1148/radiol.233482.

3. Leonardi M, Espada M, Kho RM, Magrina JF, Millischer AE, Savelli L, et al. Endometriosis and the urinary tract: From diagnosis to surgical treatment. Diagnostics (Basel) 2020;10:771. doi: 10.3390/diagnostics10100771.

4. Rennan L, Yao S, Jin H, Yi Q, Wang Y, Yang Y. Ureteral endometriosis: MR imaging appearance for predicting complex procedures. Heliyon 2024;10:e34884. doi: 10.1016/j.heliyon.2024.e34884.

5. Chin S, Kitzing YX, Quesada J, Lo G. Endometriosis MRI : Atypical cases, pitfalls and mimics. J Med Imaging Radiat Oncol 2024;68:427–33. doi: 10.1111/1754-9485.13670.

6. Kido A, Himoto Y, Moribata Y, Kurata Y, Nakamoto Y. MRI in the diagnosis of endometriosis and related diseases. Korean J Radiol 2022;23:426-45. doi: 10.3348/kjr.2021.0405.

Case Report

Radiologic and pathologic correlation of leptomeningeal metastasis presenting as a circumscribed comedo-like bulky mass with minimal brain parenchymal invasion: A case report

Arunnit Boonrod, M.D.[(1)]
Nontaphon Piyawattanametha, M.D.[(2)]
Mix Wannasarnmetha, M.D.[(1)]
Waritta Kunprom, M.D.[(3)]
From [(1)]Department of Radiology, [(2)]Department of Surgery, [(3)]Department of Pathology, Faculty of Medicine, Khon Kaen University, Khon Kaen, 40002, Thailand.
Address correspondence to M.W. (email: mixwan@kku.ac.th)

Received 9 December 2025; revised 5 February 2026; accepted 16 February 2026
doi:10.46475/asean-jr.v27i2.1003

Abstract

Bulky, mass-like leptomeningeal metastasis is rare. In radiology and surgery, it mimics an extra-axial mass and can be mistaken for meningioma. When reported pathologically as metastasis, it can be mistaken for parenchymal brain tumors, potentially delaying appropriate CSF-directed therapy. We report a unique case in which leptomeningeal disease presented as an extra-axial lesion embedded in the cortex with a comedo-like protruding surface. Recognizing this imaging and intraoperative appearance may be important, as differentiating leptomeningeal from parenchymal metastases could alter prognosis and help guide treatment decisions, including consideration of CSF-directed treatments, such as intrathecal chemotherapy or craniospinal irradiation, rather than relying on focal radiosurgery alone. Although anecdotal, this report underscores the need for heightened diagnostic awareness and warrants the need for further study to determine whether this feature reliably indicates leptomeningeal disease and meaningfully influences patient management.

Keywords: Comedo-like morphology, Differential diagnosis, Extra-axial mass, Leptomeningeal metastasis, Mimics.

THE ASEAN JOURNAL OF RADIOLOGY
ISSN 2672-9393

Introduction

When evaluating an intracranial mass on MRI, the first step is to distinguish intra-axial from extra-axial location. Definitive findings of an extra-axial lesion are a cerebrospinal fluid cleft separating the lesion from the brain, interposed cortical vessels, preservation of the cortex between the mass and white matter edema and an intact dura between a potential epidural mass and the parenchyma. Suggestive findings include a broad-based peripheral attachment along the calvarium, focal bone remodeling or sclerosis of the adjacent skull, enhancement of the overlying meninges and displacement of brain away from the inner table without true infiltration [1]. Once an extra-axial location is established, the differential diagnosis narrows to dural-based entities such as meningioma or solitary fibrous tumor, and, in rare cases, to dural metastasis even in patients without a known primary malignancy.

Leptomeningeal metastasis classically appears as diffuse linear or nodular leptomeningeal enhancement along the sulci, cranial nerves and cisterns. While "linear" and "nodular leptomeningeal enhancement" are well-established descriptors, there is no widely used term for a discrete, bulky leptomeningeal mass [2]. However, in this case we observed a comedo-like appearance, in which the lesion demonstrated definitive extra-axial radiologic features, yet was largely embedded within the brain parenchyma with only a small portion of the tumor surface protruding into the subarachnoid space. This pattern may represent a focal, bulky leptomeningeal deposit.

Case summary

A 49-year-old male presented with right hemiparesis for two days. His past medical history was unremarkable, with no known primary malignancy at presentation. Neurologic examination revealed grade II right hemiparesis.

MRI Findings: The patient underwent contrast-enhanced brain MRI for evaluation of these neurological symptoms. MRI revealed a well-circumscribed, heterogeneously enhancing mass along the left parieto-occipital convexity. It appeared iso- to slightly hypointense on T1WI and isointense on T2WI and FLAIR with iso-diffusion. A thin CSF rim (CSF cleft sign) and preserved cortical interface suggested an extra-axial location. Moderate surrounding white matter edema was observed. No significant bone involvement was seen. The initial impression favored meningioma (including atypical meningioma) or hemangiopericytoma, with metastasis considered unlikely due to extra-axial location, solitary presentation, and absence of known systemic malignancy. (Figure 1 and 2)

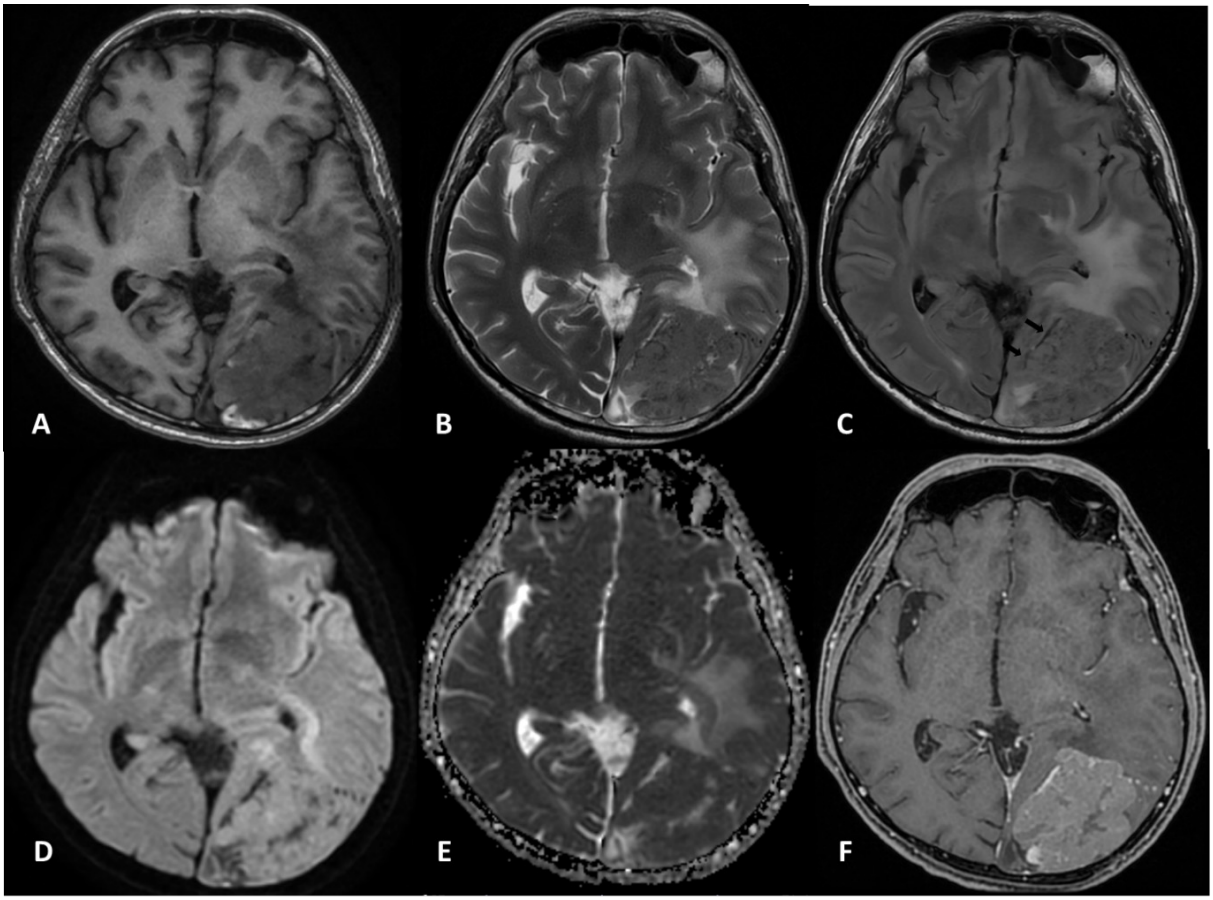

Figure 1. *MRI shows a well-defined heterogeneous enhancing mass over the left parieto-occipital convexity with associated perilesional white matter edema. (A) Axial T1WI, (B) T2WI, (C) FLAIR, (D) DWI, (E) ADC and (F) post-contrast T1WI show a heterogeneous lesion with mixed hypo- to isointense signal on T1WI and heterogeneous isointense signal on T2WI and FLAIR. The lesion demonstrates isodiffusion on DWI and ADC. Mild, heterogeneous solid enhancement is seen post-contrast T1WI.*

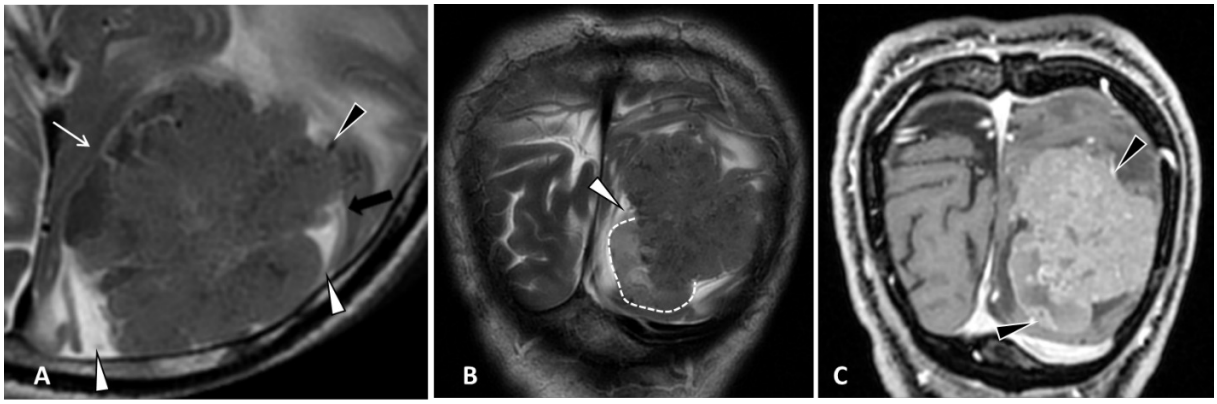

Figure 2. *MRI shows a close-up view of the mass. (A) Axial T2WI, (B) Coronal T2WI, (C) Coronal T1WI+Gd show the CSF-cleft sign (white arrowhead in A and B), intervening vessels (black arrowhead in A and C), an intervening cortex between mass and white matter (black arrow in A) and white matter buckling sign (white arrow in A). The dashed line in (B) represents the portion of the tumor surface protruding outward.*

Intraoperative Findings: The tumor appeared firm, well-defined, and embedded within the brain parenchyma. A small part of the mass was visible at the surface. It was easily dissected with a preserved plane from the brain, except for minor focal adherence to the brain parenchyma. No true dural attachment was identified. The characteristic "comedo-like" term, as used here, refers to the lesion's imaging and intraoperative morphology: a sharply demarcated mass embedded in the brain surface, partially protruding from the cortical surface, with minimal cortical brain invasion, resembling a comedo or blackhead embedded beneath the skin with a visible surface component (Figure 3).

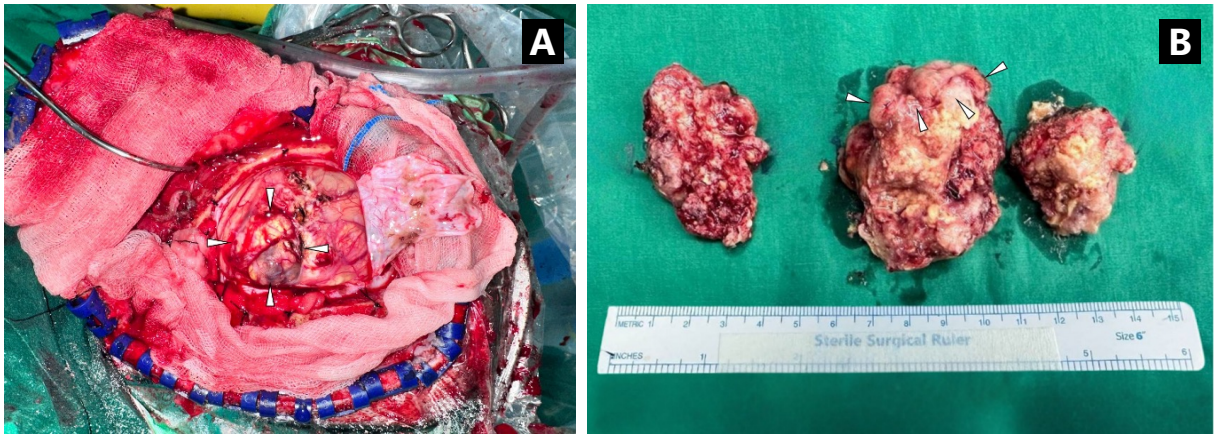

Figure 3. *Intraoperative photo (A) and gross specimens (B) show a lobulated-surface mass subtly emerging from the brain surface (arrowhead), with the majority of the mass embedded within the brain, consistent with the "comedo-like" description.*

Pathologic Findings: Histological examination demonstrated a well-circumscribed lesion with a pushing border, composed of atypical glandular, papillary, and micropapillary architectural patterns. Scattered foci of necrosis were also observed. Tumor cells were identified within the leptomeninges and lymphovascular spaces, with only minimal involvement of the adjacent brain parenchyma. Immunohistochemical staining was positive for TTF-1 and Napsin A, consistent with metastatic pulmonary adenocarcinoma. (Figure 4 and 5)

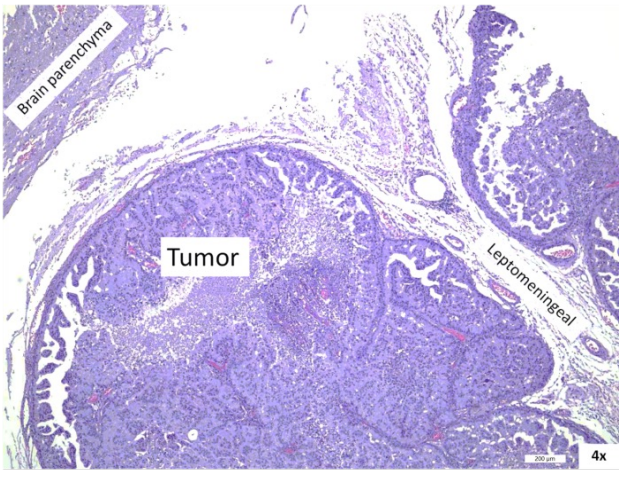

Figure 4. *Histologic section (magnification = 4X and scale bar = 200 µm) demonstrates a well-circumscribed tumor centered within the leptomeningeal space, composed of atypical glandular, papillary, and micropapillary structures with focal necrosis. These features are consistent with leptomeningeal metastatic adenocarcinoma.*

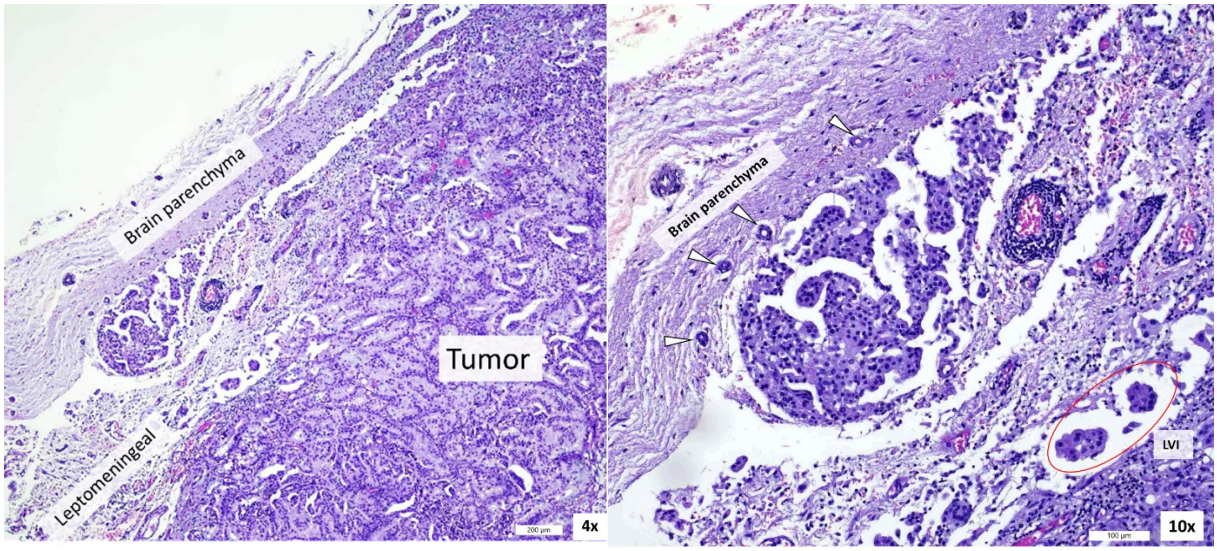

Figure 5. *Histologic sections at (A) 4× magnification (200 µm scale bar) and (B) 10× magnification (100 µm scale bar) demonstrate tumor involvement of the leptomeninges, with infiltration into lymphovascular channels (LVI) and focal extension into the adjacent brain parenchyma (arrowhead). These findings support a leptomeningeal origin with secondary parenchymal invasion.*

Discussion

In radiologic practice, classifying an intracranial mass as extra-axial typically directs attention toward dural-based pathology, particularly meningiomas and solitary fibrous tumors [3,4]. However, this focus can be overly restrictive and may lead to under-recognition of lesions arising from the pia and arachnoid mater, which together form the leptomeninges. This limitation is particularly relevant when leptomeningeal metastases present as focal, mass-like lesions, rather than in the more common diffuse pattern [2,5,6].

In the present case, the mass was correctly localized radiologically and surgically as extra-axial but was initially presumed to be dural-based, and the histopathologic diagnosis of metastasis was initially interpreted clinically as parenchymal "brain" metastasis. Only after pathologic re-evaluation, prompted by the imaging appearance and intraoperative impression, was the lesion recognized as leptomeningeal metastasis. This case underscores that the term "extra-axial" encompasses not only dural lesions but also leptomeningeal pathology and highlights the importance of distinguishing these compartments when evaluating superficially embedded, well-marginated intracranial masses.

Recognizing leptomeningeal spread rather than parenchymal disease has direct implications for management and prognosis [7]. A solitary bulky parenchymal metastasis is often managed with surgical resection followed by stereotactic radiosurgery or focal radiotherapy[8]. In contrast leptomeningeal disease calls for cerebrospinal fluid-directed therapies such as intrathecal chemotherapy or high-dose systemic chemotherapy and often craniospinal irradiation. Even when a focal mass is amenable to radiosurgery it must be combined with CSF-directed treatment given the risk of diffuse multifocal recurrence [7].

We propose the term "comedo-like" to describe the lesion's distinctive imaging and surgical morphology, which we believe may represent a reproducible and recognizable pattern that raises suspicion for leptomeningeal origin. On MRI, the mass appeared as a smoothly marginated, contrast-enhancing lesion subtly protruding beyond the cortical margin, suggesting a subarachnoid or leptomeningeal source. This configuration resembles a comedo, in which a subepidermal lesion becomes externally visible through a small surface breach, in this case, the cerebral cortex. Although observed in a single case, this pattern may offer a useful visual clue when considering atypical pathology in superficially embedded lesions, thereby guiding more accurate diagnosis and oncologic management. Further studies are warranted to determine whether this imaging feature can help differentiate leptomeningeal metastases from more common benign extra-axial tumors.

In conclusion, we report a rare case of leptomeningeal metastasis presenting as a circumscribed, extra-axial mass with a "comedo-like" configuration on preoperative MRI and intraoperative assessment. This distinctive presentation challenges conventional diagnostic assumptions and emphasizes the need for radiologists and pathologists to consider leptomeningeal metastasis in the differential diagnosis of superficially embedded, well-marginated intracranial masses. While anecdotal, the "comedo-like" appearance may serve as a helpful radiologic feature worthy of further study. Increased awareness of this imaging pattern may facilitate earlier diagnosis and appropriate oncologic intervention.

Funding

Fundamental fund 2569 (Khon Kaen University).

Conflict of interest

The authors declare that they have no conflict of interest.

Ethical approval

This study is approved by the Ethics Committee for Human Research, Khon Kaen University.

References

1. Hussain S, Mubeen I, Ullah N, Shah SSUD, Khan BA, Zahoor M, et al. Modern diagnostic imaging technique applications and risk factors in the medical field: A review. Biomed Res Int 2022;2022:5164970. doi: 10.1155/2022/5164970.

2. Commandeur F, Goeller M, Dey D. Cardiac CT: Technological advances in hardware, software, and machine learning applications. Curr Cardiovasc Imaging Rep 2018; 11:19. doi: 10.1007/s12410-018-9459-z.

3. Alberto NRI, Alberto IRI, Puyat CVM, Antonio MAR, Ho FDV, Dee EC, et al. Disparities in access to cancer diagnostics in ASEAN member countries. Lancet Reg Health West Pac 2023;32:100667. doi: 10.1016/j.lanwpc.2022.100667.

4. Niki R. The wide distribution of CT scanners in Japan. Soc Sci Med 1985;21:1131-7. doi: 10.1016/0277-9536(85)90171-6.

5. TheGlobalEconomy.com [Internet]. 2026 [cited 2026 Apr 23]. Computed tomography scanners - Country rankings. Available from: https://www.theglobaleconomy.com/rankings/computed_tomography_scanners_per_million_people/South-East-Asia/

6. Reyes-Santias F, Antelo M. Explaining the adoption and use of computed tomography and magnetic resonance image technologies in public hospitals. BMC Health Serv Res 202;21:1278. doi: 10.1186/s12913-021-07225-2.

7. TechSci Research [Internet]. New York (NY): TechSci Research; 2025 [cited 2026 Apr 23]. Vietnam CT scanners market by slice (8-slice, 16-slice, 32-slice, 64-slice, 128-slice & above), by modality (fixed v/s mobile), by device architecture (O-arm v/s C-arm), by application (cardiology, oncology, neurology, others), by end users (hospitals, diagnostic centers, others), by region, competition forecast & opportunities, 2020-2030F. Available from: https://www.techsciresearch.com/report/vietnam-ct-scanners-market/8254.html

8. Research and Markets [Internet]. Dublin (Ireland): Research and Markets; 2025 [cited 2026 Apr 23]. Vietnam CT scanners market, by region, competition, forecast & opportunities, 2020-2030F. Available from: https://www.researchandmarkets.com/reports/5646390

THE ASEAN JOURNAL OF RADIOLOGY
ISSN 2672-9393

Classic Case

Imaging findings of OHVIRA syndrome with surgical correlation in an 11-year-old girl: A classic case

Fon Suratsukkasem, M.D.
From Department of Radiology, Mahidol Bumrungrak Nakhonsawan Medical Center, Nakhonsawan, Thailand.
Address correspondence to F.S. (email: fonfon212224@gmail.com)

Received 5 March 2026; revised 25 March 2026; accepted 28 March 2026
doi:10.46475/asean-jr.v27i2.1021

Abstract

OHVIRA syndrome (Obstructed Hemivagina and Ipsilateral Renal Agenesis) is a rare congenital Müllerian duct anomaly characterized by uterine duplication, obstructed hemivagina, and ipsilateral renal agenesis. Early recognition is essential to prevent long-term complications such as endometriosis and infertility. We report the case of an 11-year-old girl who presented with acute lower abdominal pain for one day without fever. Physical examination revealed a 10-cm vaginal mass. Transabdominal ultrasonography demonstrated a cystic mass in the mid-pelvic cavity. Contrast-enhanced computed tomography confirmed uterine didelphys with marked distension of the right hemivagina and absence of the right kidney. Surgical exploration revealed a bulging right hemivagina with approximately 400 mL of retained brownish fluid, and vaginal septum excision was performed. The postoperative course was uneventful. This case highlights the importance of multimodality imaging in the early diagnosis and management of OHVIRA syndrome.

Keywords: Computed tomography, Obstructed hemivagina, OHVIRA syndrome, Renal agenesis, Ultrasound.

Introduction

OHVIRA syndrome, also known as Herlyn–Werner–Wunderlich syndrome, is a rare congenital Müllerian duct anomaly characterized by the triad of uterine didelphys, obstructed hemivagina, and ipsilateral renal agenesis [1]. The estimated incidence of Müllerian duct anomalies ranges from 0.1% to 3.8% in the general population [2].

The Müllerian (paramesonephric) ducts normally develop into the fallopian tubes, uterus, cervix, and upper vagina through a process of elongation, fusion, canalization, and septal resorption. At 9 weeks of gestation, the ducts elongate and reach the urogenital sinus. The uterovaginal canal is formed and inserted into the urogenital sinus at the Müller tubercle [2].

The mesonephric (Wolffian) ducts play an important role in the development of the urinary system and are closely related to the Müllerian ducts during embryogenesis. Disruption of this coordinated development may result in combined genital and urinary tract anomalies. In OHVIRA syndrome, failure of Müllerian duct fusion leads to uterine didelphys, while ipsilateral renal agenesis is attributed to abnormalities of the mesonephric duct.

Patients typically present shortly after menarche with cyclic lower abdominal pain, dysmenorrhea, and a tender vaginal mass. Other reported symptoms include recurrent urinary tract infections, urinary retention, and vaginal discharge [3]. Delayed diagnosis may lead to complications such as endometriosis, pelvic adhesions, and an increased risk of infertility and other adverse reproductive outcomes [4].

Ultrasonography is usually the first-line imaging modality because it is readily available, cost-effective, and free of ionizing radiation. Magnetic resonance imaging is considered the reference standard because of its multiplanar capability and superior soft-tissue characterization [5]. Early recognition is essential for timely surgical management and prevention of long-term reproductive complications.

Herein, we report a classic case of OHVIRA syndrome in an 11-year-old girl presenting with acute lower abdominal pain, emphasizing the role of multimodality imaging in diagnosis and surgical management.

THE ASEAN JOURNAL OF RADIOLOGY
ISSN 2672-9393

Case summary

An 11-year-old girl presented with acute lower abdominal pain for one day. She denied fever, abnormal uterine bleeding, or urinary symptoms. Physical examination revealed a palpable lower abdominal mass and a 10-cm bulging vaginal mass. Transabdominal ultrasonography demonstrated a well-defined hypoechoic cystic mass measuring approximately 9.4 × 5.9 cm, located in the mid-pelvic cavity, with a suspected connection to the right uterine horn. The left uterine horn was separately identified in the left pelvic cavity (Figure 1).

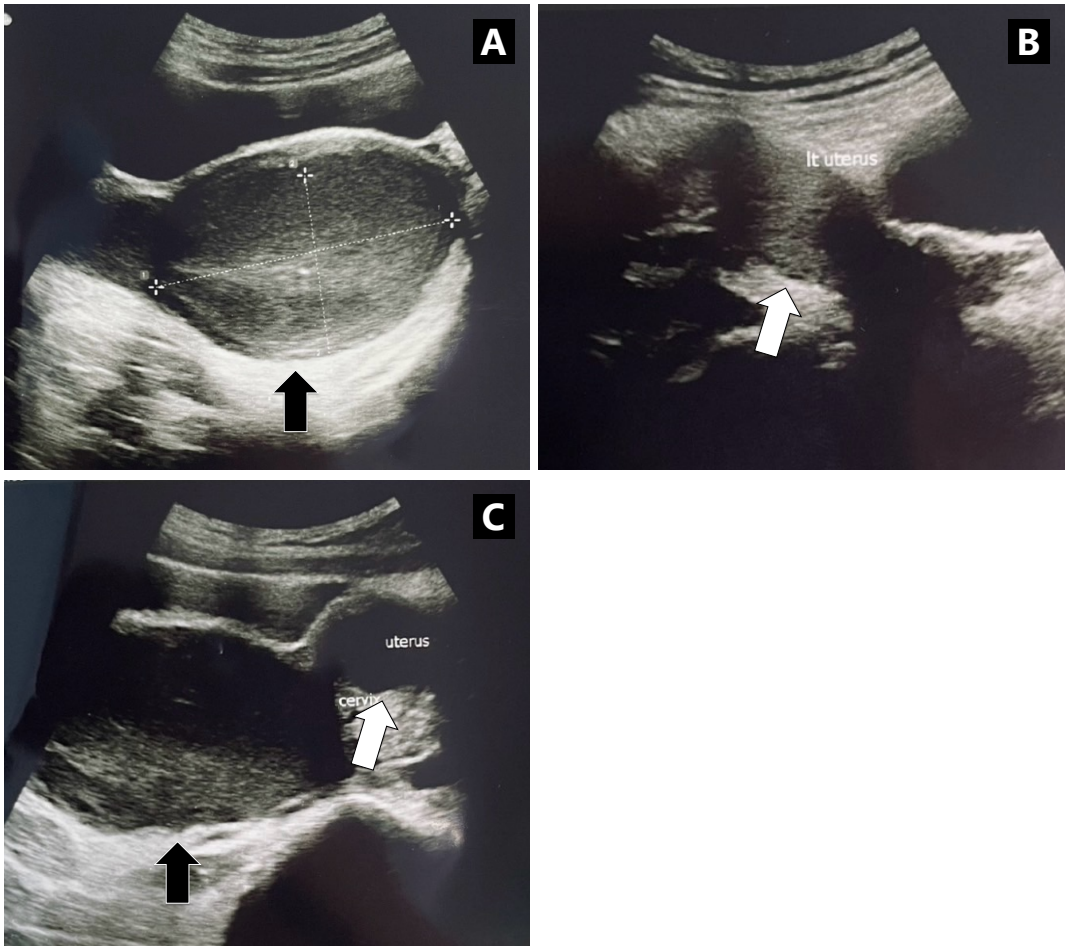

Figure 1. *Transabdominal ultrasonography shows a well-defined hypoechoic cystic mass in the mid-pelvic cavity (A and C, black arrow) and the left uterine horn in the left pelvic cavity (B and C, white arrow).*

Contrast-enhanced computed tomography of the lower abdomen confirmed uterine didelphys. Hydrocolpos of the right hemivagina was seen, measuring 6.9 × 7.7 × 13.9 cm (AP × transverse × craniocaudal dimensions). It communicated with the right uterine horn, which demonstrated hydrometra. The right kidney was not visualized, while the left kidney appeared normal. The left hemivagina, left uterine horn, and bilateral ovaries were unremarkable (Figure 2).

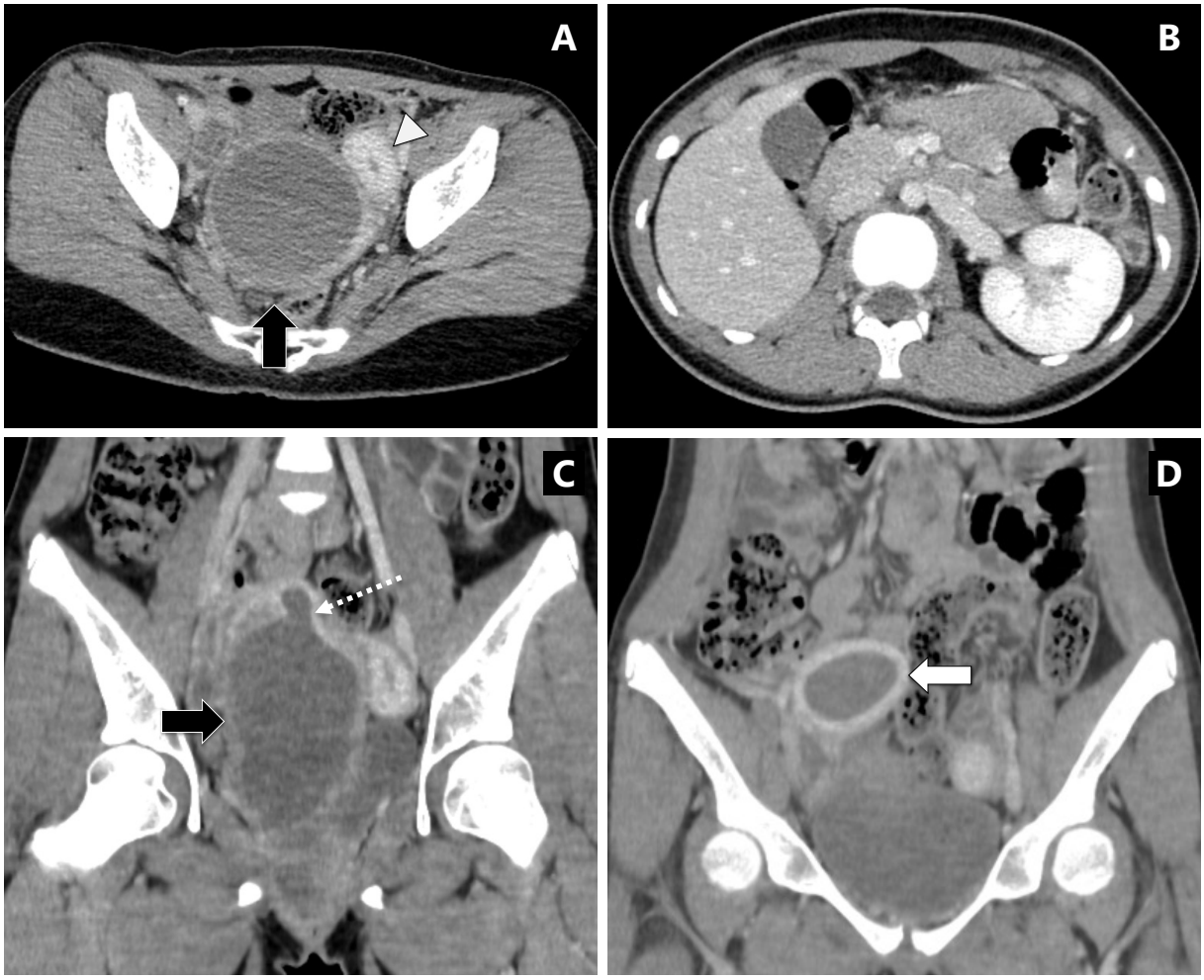

Figure 2. *Axial (A, B) and coronal (C, D) contrast-enhanced CT images of the lower abdomen demonstrate hydrocolpos of the right hemivagina (black arrow), communicating with the endocervix (white dotted arrow) and extending into the right uterine horn, which shows hydrometra (white arrow). The left uterine horn is unremarkable (arrowhead). The right kidney is not visualized (B).*

THE ASEAN JOURNAL OF RADIOLOGY
ISSN 2672-9393

The patient underwent vaginoplasty with resection of the vaginal septum under general anesthesia. Intraoperative findings revealed a bulging right vaginal canal, from which approximately 400 mL of thick brownish fluid was drained. The vaginal septum was incised to establish continuity of the vaginal canal. A partial vaginal septum, located approximately 5 cm above the hymen, was subsequently excised to reconstruct a single vaginal canal. The procedure was completed without complications, and the postoperative course was uneventful.

Discussion

OHVIRA syndrome represents a rare spectrum of Müllerian duct anomalies resulting from abnormal development of the Müllerian and mesonephric ducts. The condition is classically characterized by uterine didelphys, obstructed hemivagina, and ipsilateral renal agenesis [1,6]. The close embryologic relationship between the genital and urinary systems explains why renal anomalies frequently coexist in affected patients.

Several classifications have been proposed based on the degree of vaginal obstruction and uterine communication. Our case corresponds to Type 1.1 [7], defined as a completely obstructed hemivagina with a blind hemivaginal pouch. This subtype typically presents at an earlier age, often shortly after menarche due to the progressive accumulation of menstrual blood, leading to hematocolpos and hematometra. Early recognition is particularly important in Type 1.1 cases, as prolonged obstruction may predispose patients to endometriosis, pyosalpinx, and even pyocolpos [7,8].

Ultrasonography is usually the first-line imaging modality because it is readily available and free of ionizing radiation [5]. In this patient, transabdominal ultrasonography demonstrated a large midline cystic pelvic mass with a separately identified uterine horn, raising suspicion for a Müllerian duct anomaly. Although magnetic resonance imaging is considered the reference standard for evaluating complex Müllerian anomalies due to its multiplanar capability and superior soft-tissue characterization [5], contrast-enhanced CT was performed due to the patient's acute presentation and institutional availability. CT adequately delineated uterine duplication, marked distension of the right hemivagina containing slightly hyperattenuating fluid suggestive of retained old blood products, and absence of the right kidney. These findings were essential for confirming the diagnosis and guiding surgical planning.

Definitive management consists of surgical resection of the obstructing vaginal septum to restore normal outflow and prevent long-term complications [9]. In our case, surgical findings correlated well with imaging, revealing a markedly distended right vaginal canal containing retained old blood. Septum excision successfully established a single vaginal canal, and the postoperative course was uneventful.

This case underscores the pivotal role of multimodality imaging in the diagnosis of OHVIRA syndrome and highlights the importance of early detection, particularly in completely obstructed subtypes, to prevent reproductive sequelae.

This report provides additional educational value by demonstrating the diagnostic role of CT in emergency settings and highlighting precise imaging-surgical correlation in a classic OHVIRA subtype.

Conclusion

This case demonstrates the characteristic imaging findings of OHVIRA syndrome and emphasizes the importance of considering this diagnosis in adolescent females presenting with pelvic pain and a cystic pelvic mass, particularly in the presence of ipsilateral renal agenesis. Multimodality imaging plays a pivotal role in accurate diagnosis. Although magnetic resonance imaging remains the reference standard, contrast-enhanced CT can provide sufficient anatomic detail in acute settings to confirm the diagnosis and guide surgical management. Early recognition is essential to prevent long-term reproductive complications.

References

1. Taliento C, Rondoni A, Scutiero G, Pavone M, Mordenti M, Vizzieli G, et al. Uterus didelphys with hematocervix in the unilateral obstructed hemivagina and ipsilateral renal agenesis: a case report of Herlyn-Werner-Wunderlich syndrome. Reprod Med [Internet]. 2024 [cited 2026 Mar 28];5:197-203. Available from: https://doi.org/10.3390/reprodmed5040018

2. Burgis J. Obstructive Müllerian anomalies: case report, diagnosis, and management. Am J Obstet Gynecol 2001;185:338–44. doi: 10.1067/mob.2001.116738.

3. Devanabanda B, Chatterton B, Hassan IN, Patel J. Obstructed hemivagina with ipsilateral renal agenesis (OHVIRA) syndrome: typical presentation of a rare syndrome. Radiol Case Rep 2023;18:2437-40. doi: 10.1016/j.radcr.2023.04.016.

4. Del Vescovo RD, Battisti S, Di Paola VD, Piccolo CL, Cazzato RL, Sansoni I, et al. Herlyn-Werner-Wunderlich syndrome: MRI findings, radiological guide (two cases and literature review), and differential diagnosis. BMC Med Imaging 2012;12:4. doi: 10.1186/1471-2342-12-4.

5. Behr SC, Courtier JL, Qayyum A. Imaging ofMüllerian duct anomalies. Radiographics 2012;32:E233-50. doi: 10.1148/rg.326125515.

6. Kim HJ, Lee EJ, Chang YW, Hong SS, Hwang J, Nam B, et al. Anatomical variations, genitourinary anomalies and clinical presentations in obstructed hemivagina and ipsilateral renal anomaly syndrome: case series. J Korean Soc Radiol 2025;86:129-40. doi: 10.3348/jksr.2024.0018.

7. Zhu L, Chen N, Tong JL, Wang W, Zhang L, Lang JH. New classification of Herlyn-Werner-Wunderlich syndrome. Chin Med J (Engl) 2015;128:222-5. doi: 10.4103/0366-6999.

8. Tong J, Zhu L, Chen N, Lang J. Endometriosis in association with Herlyn-Werner-Wunderlich syndrome. Fertil Steril 2014;102:790-4. doi: 10.1016/j.fertnstert.2014.05.025.

9. Smith NA, Laufer MR. Obstructed hemivagina and ipsilateral renal anomaly (OHVIRA) syndrome: management and follow-up. Fertil Steril 2007;87:918-22. doi: 10.1016/j.fertnstert.2006.11.015.

Perspective

Ultrasound imaging for preventative services in a preventive radiology initiative

Rijo M Choorakuttil, M.D.[(1)]
Praveen K Nirmalan, M.P.H.[(2)]
From [(1)]Department of Preventive Radiology & Integrated Diagnostics, [(2)]Department of Research AMMA Scans-AMMA Center for Diagnosis and Preventive Medicine Pvt Ltd, Kochi, Kerala, India.
Address correspondence to P.N. (email: echasapt@gmail.com)

Received 9 March 2026; revised 25 March 2026; accepted 10 April 2026
doi:10.46475/asean-jr.v27i2.1025

Keywords: Non-Communicable Diseases, Preventive Radiology, Shear Wave Elastography, Ultrasound.

Introduction

The disease-prevention model identifies early pre-clinical disease and subgroups at risk of developing symptoms and signs of abnormal structure and function. This model, integrating genetic, environmental, social, and other information with predictive biomarkers (biomolecular or imaging), helps monitor disease development and progression, the structural and functional integrity of organ systems, and the impact of preventive and therapeutic interventions. Medical imaging provides standardised, protocol-based, non-invasive, and relatively painless objective measurements that guide therapeutic pathways through integration with quantitative imaging and volumetric assessments. Ultrasound imaging techniques with better visualisation of structures, faster turnaround times, predictive and prognostic algorithms, and improved access and affordability through portable and point-of-care applications are currently available. These ultrasound advancements can be leveraged for ultrasound-based screening and early detection of abnormalities in the preclinical stages before the presentation with late-stage disease.

THE ASEAN JOURNAL OF RADIOLOGY
ISSN 2672-9393

The epidemiological transition level (ETL) provides the ratio of the disability-adjusted life years for communicable and non-communicable diseases (NCDs). A decreasing ETL ratio indicates an increasing relative magnitude of NCDs. India had an ETL of 1.56 in 1990, which decreased to 0.50 in 2016, with all states in India reporting an ETL < 1.0 in 2016 [1]. Several studies from India have reported the large prevalence of NCDs in India including 11·4% for diabetes, 15·3% for prediabetes, 35·5% for hypertension, 28·6% for generalised obesity, 39·5% for abdominal obesity, and a 32.0% prevalence of ultrasound-detected non-alcoholic fatty liver disease (NAFLD) in urban India in 2009 and 30·7% in rural India in 2016 [2-9]. The high prevalence of NCDs translates to a large population at high risk for complications of NCDs and end-organ damage in India unless they are detected early and managed appropriately through the course of NCDs.

Preventive Radiology Program in India

The Indian Radiological and Imaging Association (IRIA) started a preventive radiology initiative in 2021, positioning radiologists as an important first line for preventive and risk prediction services. This initiative promotes preventive and integrated radiology as a career path for radiologists, apart from the existing clinical and interventional radiology paths. The program uses imaging-based biomarkers for the early identification of NCDs, including metabolic disorders, to assess endothelial dysfunction, identify imaging-based criteria to guide therapeutic interventions, and monitor the progress of diseases and the impact of interventions on the structural and functional integrity of target end-organ systems. The preventive radiology program works towards these goals by establishing dedicated integrated radiology imaging diagnostics clinics with ultrasound imaging as the fulcrum for screening. Ultrasound was chosen as the primary imaging modality due to its availability, accessibility, affordability, and ability to scale up services, compared to CT or MRI imaging, and specialised biochemical or molecular tests. Ultrasound has a more rapid report turnaround time, provides objective visual reporting of structural and functional abnormalities, is non-invasive and relatively painless, and has availability, affordability and accessibility advantages compared to specialised biochemical or molecular testing, especially in rural, remote and low-resource areas.

Conceptual Structure of the Program

Several core areas in the ultrasonography curriculum and service provision must be strengthened to transition effectively to preventive radiology. Most radiologists currently offer imaging services based on demand from referring physicians. A shift towards proactive imaging based on clinical history, risk factors, and towards early detection is essential to provide preventive services. Additionally, continuous technical skill upgradation to improve the interpretative ability and the application of imaging biomarkers for screening and early identification of NCDs, expanding the reach of the program through regular offline and online learning initiatives, improving the local evidence base on imaging biomarkers, developing policy guidelines to improve synergy with other multidisciplinary stakeholders, and identifying NCD priorities based on the specific country profiles are needed.

The preventive radiology initiative in India initially focuses on metabolic syndromes, atherosclerotic cardiac diseases and strokes, cancers, and endothelial dysfunction. Each identified disease priority has an academic and training national lead, a trainer of trainers' pool at the national and state levels, and a team of multi-institutional experts who lead research appropriate for the condition and population needs. Generating local evidence on the various measurement parameters that underpin the screening algorithms used for the assessment optimisation of clinical protocols is a priority. The various aspects of the preventive radiology initiative are presented in Table 1.

THE ASEAN JOURNAL OF RADIOLOGY
ISSN 2672-9393

Table 1. *The various aspects of the Preventive Radiology Program.*

The various aspects of the Preventive Radiology Program
1. Creation of subcommittees and working groups to a. Organize continuous medical education programs, workshops and hands-on training, b. Develop a pool of trainer-of-trainers, c. Provide competency-based training for radiologists in the state, d. Provide competency-based training for radiology postgraduate residents at teaching hospitals, e. Provide training to start preventive radiology outpatient units, f. Generate local data on the use and integration of imaging biomarkers. g. Generate local evidence to inform algorithms, h. Develop local multidisciplinary research teams for non-communicable and chronic diseases.
2. Identification and evaluation of imaging biomarkers- organ, system, and disease-specific.
3. Evidence-based integration of imaging biomarkers with clinical and biochemical algorithms and establishment of evidence-based protocols for image-guided interventions and biopsies.
4. Integrate healthy aging, wellness and image-based screening for biomarkers.
5. Develop NCD-specific guidelines and algorithms.
6. Develop image-based biobanks.
7. Develop specific pragmatic applications for preventive radiology at the primary, secondary, and tertiary care levels.
8. Integrate with the appropriate National Digital Health Mission and health programs at the governmental level.
9. Integrate AI and deep-learning algorithms.
10. Develop a technology entrepreneurship program.
11. Health Education and Awareness: optimising the use of digital media.

Early Results from India

The preventive radiology initiative has published the standardised techniques for ultrasound shear wave elastography of the liver, the first published normative distribution of liver stiffness measurements in this population, and liver stiffness-based prevalence of non-alcoholic fatty liver disease in India [10-12]. Nineteen hands-on training workshops focused on US-SWE liver imaging (60 participants per workshop), and 218 webinars (mean 162±18 participants per webinar) on liver, cancer, stroke, breast cancer, musculoskeletal and neurological conditions have been conducted since 2021 to upskill radiologists in preventive radiology practices using ultrasonography. The risk stratification and predictive capabilities of fetal Doppler and trimester-specific ultrasound-based protocols focused on preterm preeclampsia (PE), fetal growth restriction (FGR) and comprehensive pregnancy assessments were integrated with antenatal care to address perinatal mortality (PMR) in India, which led to a substantive reduction in the magnitude of PE, FGR and PMR in India, as reported in published studies [13-18]. The preventive radiology initiative has collaborated with the state government of Kerala, local non-governmental organisations, and healthcare stakeholders to develop a comprehensive cancer screening program integrating medical imaging for early identification of pre-cancerous lesions.

A dedicated preventive radiology clinic, established a year ago within an integrated diagnostics radiology centre, at Kochi in the southern Indian state of Kerala, offers walk-in services for persons seeking screening for early signs of NCDs and lifestyle diseases. The clinic has so far screened 1,181 persons with a mean age of 44.33 ± 10.03 years (range 29 to 62 years). Most of the screened population were females (69.44%), 41.47% had a body mass index (BMI) ≥25 to 30 kg/m2, 31.79% had a BMI ≥30 kg/m2, 26.20% had hypertension, and 32.23% had diabetes mellitus. Liver stiffness measurements (LSM) using ultrasound shear wave elastography were between 7 to 9 kPa in 22.79%, and 14.29% had LSM >9 kPa. Screen positive persons (for LSM abnormalities) were recommended dietary and lifestyle changes and triaged for referral to a multidisciplinary hepatology unit for further care. These early results in this opportunistic screening highlight the potential for preventive lifestyle interventions, especially concerning metabolic dysfunction-associated steatotic liver disease (MASLD) in nearly one-fourth of the screened population. These are early interim results focused on the liver and obesity from this OPD, and the OPD is currently expanding to include other NCDs in the screening and early detection of structural and functional abnormalities.

THE ASEAN JOURNAL OF RADIOLOGY
ISSN 2672-9393

Preventive Radiology for the ASEAN Region

The ASEAN region shares several characteristics with the South Asian region in the context of healthcare priorities, including an epidemiological transition with increasing NCD prevalence, and a declining yet persistent prevalence of communicable diseases, perinatal mortality, and undernutrition [19,20]. Nearly two-thirds of all deaths in the ASEAN region were attributable to NCDs in 2021, and over half of these deaths occurred in persons aged 30-69 years [19.20]. Cardiovascular diseases, cancers, diabetes and chronic respiratory diseases were the major contributors to the NCD magnitude in the ASEAN region [19,20]. Metabolic risk factors such as raised blood pressure, high body mass index or waist-to-hip ratio, high blood sugar levels and abnormal serum lipid concentrations are common in the ASEAN region [19]. Similar to South Asia, urbanization, industrialization, demographic transition to an aging population, increased life expectancy, dietary changes and sedentary lifestyles contribute to the increasing prevalence of NCDs in the ASEAN region [19]. Governments in the ASEAN region have initiated several programs based on global and regional action plans and WHO action plans, to address the growing magnitude of NCDs in the ASEAN region. However, similar to South Asia, progress towards meeting acceptable targets has been slow.

The preventive radiology program has the potential to scale up early identification of NCDs in the ASEAN region, incorporating early interventions, including lifestyle and therapeutic interventions to reduce progression to late-stage disease and complications. Ultrasound is widely available and can be developed as a first-line screening tool in the ASEAN region. The screening potential of CT and MRI can be optimized in regions where these are widely available, affordable and accessible in the region, however, there is a wide disparity in the availability of these services, similar to South Asia. The early results from the preventive radiology model in India suggest that a similar model may be considered in the ASEAN region to complement and supplement existing healthcare systems in the region. However, the model must adapt to consider local contexts, healthcare needs, available infrastructure and resources, including trained personnel and training programs.

Conclusion

Radiologists focused on ultrasound practice can develop dedicated clinics focused on early identification, risk stratification, individualised prediction and prognostic paths that bridge the gap between primary and tertiary care. Early identification through these clinics can reduce the absolute number of cases identified at late stages, and baseline objective measurements are useful to assess interventional impact and progress. This approach will be useful in initiating care pathways earlier in rural areas that do not have access to specialised biochemistry or molecular labs, and can minimise issues with the storage and transport of samples. The radiology curriculum must be revised to include these preventive possibilities to offer newer career pathways for radiologists as an integral part of the healthcare system. Operator skill dependency is a limitation with ultrasound (as it is for laboratory tests) that is offset to a certain degree with the newer machines, techniques like elastography that provide operator and vendor-neutral results, and AI-integrated algorithms. Radiology can develop as the proactive fulcrum around which more effective integrated service delivery systems are developed for preventive and follow-up care in rural areas, which remain a challenge in the healthcare system.

Funding

The Preventive Radiology program of IRIA is supported in part by a grant provided by M/s Mindray Medical India Pvt. Ltd. to the Indian Radiological and Imaging Association to support training programs. The grant agency did not have any input into data collection, research related to the program, analysis, interpretation, or preparation of the manuscript.

References

1. Indian Council of Medical Research, Public Health Foundation of India, and Institute for Health Metrics and Evaluation. India: Health of the Nation's States — The India State-Level Disease Burden Initiative [Internet]. New Delhi, India: ICMR, PHFI, and IHME; 2017 [cited 2026 Apr 5]. Available from: https://www.healthdata.org/research-analysis/library/india-health-nations-states

2. Anjana RM, Unnikrishnan R, Deepa M, Pradeepa R, Tandon N, Das AK, et al. Metabolic non-communicable disease health report of India: the ICMR-INDIAB national cross-sectional study (ICMR-INDIAB-17). Lancet Diabetes Endocrinol 2023;11:474-89. doi: 10.1016/S2213-8587(23)00119-5.

3. Sarin SK, Kumar M, Eslam M, George J, Al Mahtab M, Akbar SMF, et al. Liver diseases in the Asia-Pacific region: a Lancet Gastroenterology & Hepatology Commission. Lancet Gastroenterol Hepatol 2020;5:167-228. doi: 10.1016/S2468-1253(19)30342-5. Epub 2019 Dec 15. Erratum in: Lancet Gastroenterol Hepatol 2020;5:e2. doi: 10.1016/S2468-1253(20)30021-2.

4. Younossi ZM, Koenig AB, Abdelatif D, Fazel Y, Henry L, Wymer M. Global epidemiology of nonalcoholic fatty liver disease-Meta-analytic assessment of prevalence, incidence, and outcomes. Hepatology 2016;64:73-84. doi: 10.1002/hep.28431.

5. Mukherjee PS, Vishnubhatla S, Amarapurkar DN, Das K, Sood A, Chawla YK, et al. Etiology and mode of presentation of chronic liver diseases in India: A multi centric study. PLoS One 2017;12:e0187033. doi: 10.1371/journal.pone.0187033.

6. Duseja A, Singh SP, Saraswat VA, Acharya SK, Chawla YK, Chowdhury S, et al. Non-alcoholic fatty liver disease and metabolic syndrome-positionpaper of the Indian National Association for the Study of the Liver, Endocrine Society of India, Indian College of Cardiology and Indian Society of Gastroenterology. J Clin Exp Hepatol 2015;5:51-68. doi: 10.1016/j.jceh.2015.02.006.

7. Duseja A, Singh SP, Mehta M, Shalimar, Venkataraman J, Mehta V, et al. Clinicopathological profile and outcome of a large cohort of patients with nonalcoholic fatty liver disease from South Asia: Interim results of the Indian Consortium on Nonalcoholic Fatty Liver Disease. Metab Syndr Relat Disord 2022;20:166-73. doi: 10.1089/met.2021.0104.

8. Chalmers J, Ban L, Leena KB, Edwards KL, Grove JL, Aithal GP, et al. Cohort profile: the Trivandrum non-alcoholic fatty liver disease (NAFLD) cohort. BMJ Open 2019;9: e027244. doi: 10.1136/bmjopen-2018-027244.

9. Sarin SK, Prasad M, Ramalingam A, Kapil U. Integration of public health measures for NAFLD into India's national programme for NCDs. Lancet Gastroenterol Hepatol 2021;6:777-8. doi:10.1016/S2468-1253(21)00264-8.

10. Choorakuttil RM, Chaubal RN, Arunachalam VK, Bagri N, Gupta A, Bansal J, et al. Practical steps of shear wave elastography for nonalcoholic fatty liver disease in an adult population. Indographics 2022; 01: 171-83. doi: 10.1055/s-0042-1759544.

11. Choorakuttil RM, Chaubal RN, Pratap T, Chelladurai A, Nirmalan PK. Distribution of normative percentiles of liver stiffness measurement using ultrasound shear wave elastography in an adult Asian Indian population. Indian J Radiol Imaging 2024; 34:596-602. doi: 10.1055/s-0044-1782163.

12. Choorakuttil RM, Chaubal RN, Pratap T, Arunachalam VK, Kumar SH, Bagri N, et al. Prevalence of chronic liver disease based on ultrasound shear wave elastography in an adult Asian Indian population attending outpatient preventive radiology clinics in India. J Clin Ultrasound 2025 ;53:459-68. doi: 10.1002/jcu.23888.

13. Choorakuttil RM, Rajalingam B, Satarkar SR, Sharma LK, Gupta A, Baghel A, et al. Reducing perinatal mortality in India: Two-Years results of the IRIA fetal radiology Samrakshan program. Indian J Radiol Imaging 2022;32:30-7. doi: 10.1055/s-0041-1741087.

14. Sharma LK, Choorakuttil RM, Jadon DS, Nirmalan PK. Impact of the community-integrated model of Samrakshan on perinatal mortality and morbidity in Guna district of central India. Indian J Radiol Imaging 2022;33:65-9. doi: 10.1055/s-0042-1759483.

15. Gupta A, Choorakuttil RM, Nirmalan PK. Integration of fetal doppler with routine antenatal third-trimester ultrasound significantly reclassifies the magnitude of fetal growth restriction in northern India. J Ultrasound 2025;28:679-84. doi: 10.1007/s40477-025-01062-3.

16. Satarkar SR, Sharma LK, Choorakuttil RM, Nirmalan PK. Effectiveness of risk stratification for fetal growth restriction at routine antenatal ultrasound assessment at 11-14 gestation weeks in a rural population of western India. J Clin Ultrasound 2025;53:1304-11. doi: 10.1002/jcu.23989.

17. Sharma LK, Choorakuttil RM, Nirmalan PK. Impact of a stage-based classification on the incidence of fetal growth restriction, preterm birth rates, and birthweight in a rural community of central India. Fetal Diagn Ther 2025;52:1-7. doi: 10.1159/000540199.

18. Sharma, LK, Choorakuttil, RM, Nirmalan P K Impact of a community-oriented comprehensive clinical and ultrasound care modelIntegrating risk stratification, fetal doppler, health education and low-dose aspirin on preeclampsia rates in central India. Sonography [Internet]. 2025 [cited 2026 Apr 7];12:512-7. Available from: https://doi.org/10.1002/sono.70019

19. Castillo-Carandang NT, Buenaventura RD, Chia YC, Do Van D, Lee C, Duong NL, et al. Moving towards optimized noncommunicable disease management in the ASEAN region: Recommendations from a review and multidisciplinary expert panel. Risk Manag Healthc Policy 2020;13:803-19. doi: 10.2147/RMHP.S256165.

20. de Silva A, Varghese C, Amin MR, Bhagwat SS, Bruni A, Bunleusin S, et al. Non-communicable diseases in South-East Asia: Journeying towards the SDG target. Lancet Reg Health Southeast Asia 202318:100305. doi: 10.1016/j.lansea.2023.100305.

Pictorial Essay

Acute and critical paediatric neurological conditions: The role of the neuroradiologist

Vicka Tang, M.B.B.S.
Yee Ling Elaine Kan, M.B.Ch.B., F.R.C.R., F.H.K.C.R., F.H.K.A.M.
From Department of Radiology, Hong Kong Children's Hospital, Hong Kong, People Republic of China.
Address correspondence to V.T. (email: v.tang@ha.org.hk)

Received 16 January 2026; revised 12 March 2026; accepted 22 April 2026
doi:10.46475/asean-jr.v27i2.1009

Abstract

Acute paediatric neurological diseases are common conditions that can result in significant morbidity and mortality, particularly if a timely diagnosis is not made. Unfortunately, clinical presentations can be non-specific, with seizures and headaches being the most frequent complaints. It is therefore important for radiologists to be familiar with these conditions and their respective imaging features to allow prompt diagnosis and management.

The aim of this article is to briefly review the clinical presentation and imaging features across six common categories: intracranial haemorrhage, toxin-related injury, infections, autoimmune disorders, stroke, and seizures.

Keywords: Acute toxic leucoencephalopathy, ADEM, Neonatal CNS infection, Neuroradiologist, Paediatric, Paediatric stroke, PRES.

Background

In a multi-institutional study of 960,020 paediatric admissions across 11 states in the US, 10.7% of admissions included a neurologic diagnosis [1]. Children admitted with a neurologic diagnosis had a significantly longer median length of hospital stay, were nearly three times more likely than other hospitalized children to require intensive care, and had a threefold higher mortality rate [1].

THE ASEAN JOURNAL OF RADIOLOGY
ISSN 2672-9393

Imaging Modality

Non-contrast head CT is the study of choice in patients with suspected acute intracranial haemorrhage. It is also indicated for patients requiring rapid imaging due to acute changes in neurologic status, particularly if brain MRI is not readily available. As paediatric patients are more susceptible to the adverse effects of ionizing radiation exposure than adults, CT protocols must be optimized for paediatric dosing following the As Low As Reasonably Achievable (ALARA) principle. Contrast may be necessary when infection is suspected.

MRI is sometimes handicapped by its long scan time and the need for anaesthesia for younger children. However, it has higher sensitivity and specificity than CT and ultrasound for detecting many pathologies and hence remains a crucial tool in the diagnosis and monitoring of many paediatric neurological diseases. The use of non-pharmacological methods including "feed and wrap" in infants or MRI video displays in children should be employed whenever possible. Fast MRI protocols such as HASTE and SSFSE allow rapid image acquisition, which can minimize or sometimes eliminate the need for sedation. If sedation is deemed necessary, patients should be monitored closely by the anaesthesia or paediatric care team.

Intracranial Haemorrhage

A range of injuries to the scalp, skull, or brain may be seen in term babies following normal or assisted vaginal delivery. There are various maternal and fetal factors which increase the risk of cranial trauma.

In birth-related head trauma, the most common cranial injuries are subdural haematoma (SDH), cephalohaematoma, subarachnoid haemorrhage, and intraparenchymal haemorrhage [2] (Figure 1). Common locations of SDH include the tentorial, interhemispheric, cerebral convexity, and parafalcine regions [2]. Vacuum- and forceps- assisted delivery are by far the most common causes of birth-related head injuries [2] (Figure 2). Fractures caused by birth trauma are more frequently depressed than linear, and the parietal and frontal bones are most often involved [3].

The dating of extra-axial haematomas based on CT attenuation must be interpreted with caution. A study was conducted to analyse the first appearance of a hypodense component within an SDH in 11 infants who had a history of abusive head injury. Uniformly hyperdense SDH was seen on the initial CT scan. For each case, there is a

range of times over which the hypodense component could have appeared, and these ranged from a minimum of 0.3 days to a maximum of 16 days [4]. Multiple factors are known to affect the neuroimaging appearances of SDH, such as the concentration of red blood cells, the integrity of cell membranes, the protein content of the blood clot, and the amount of cerebrospinal fluid within the collection.

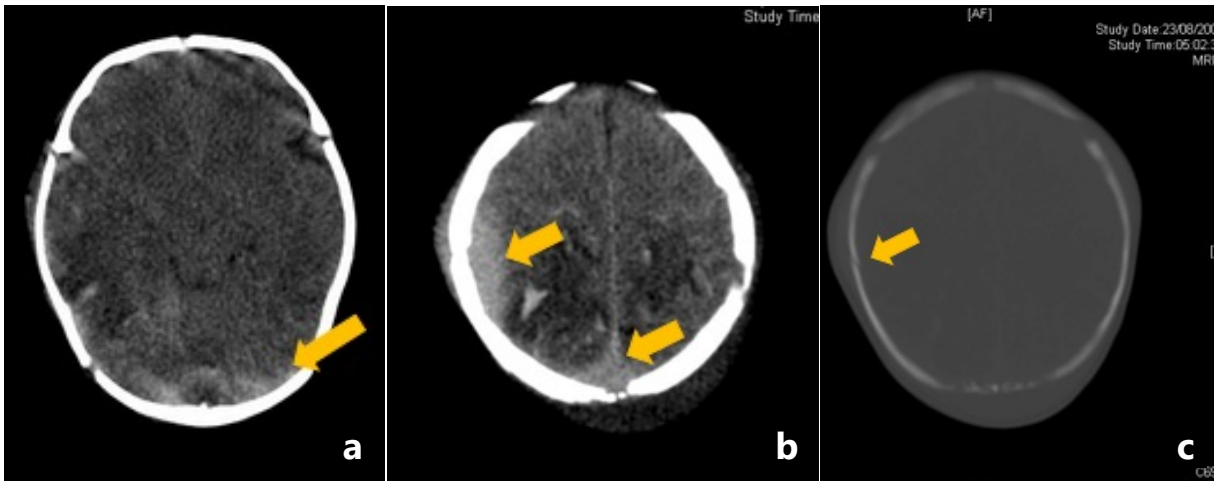

Figure 1. *Non-enhanced CT brain of a full-term infant born by caesarean delivery who presented with seizure and apnoea. (a) There is evidence of subdural haematoma along the tentorium, (b) epidural haematoma, and (c) a right parietal skull fracture.*

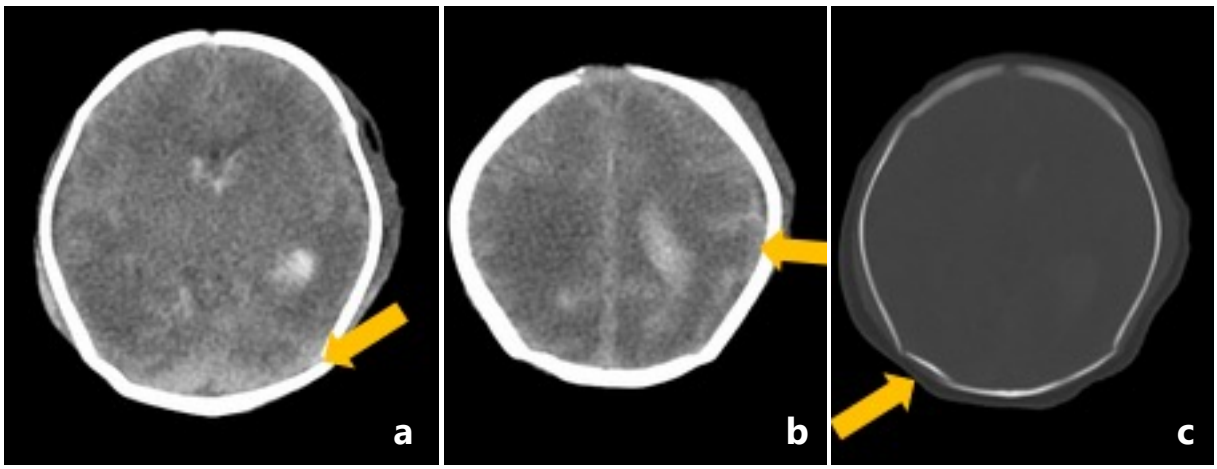

Figure 2. *Non-enhanced CT brain of a premature infant born at 32 weeks of gestation born via forceps-assisted delivery. (a) Subdural haematoma is seen along the tentorium (arrow), (b, c) demonstrate grade III intraventricular haemorrhage and subarachnoid haemorrhage (arrow), with marked cerebral oedema and sulcal effacement. (c) On the bone window, there is a mildly depressed fracture involving the occipital bone (arrow).*

THE ASEAN JOURNAL OF RADIOLOGY
ISSN 2672-9393

Toxin-Related Insults

There are multiple causes of neurotoxicity in children. These include intrinsic causes which result from the build-up of toxic metabolites due to genetic or acquired disorders, and metabolic abnormalities, as well as extrinsic causes such as medications, toxins, and other insults (Table 1).

Early identification of imaging findings can facilitate early diagnosis and the institution of appropriate treatment to reverse or limit injury to the developing brain.

Table 1. *Intrinsic and external causes of neurotoxicity in children.*

Intrinsic causes	Extrinsic causes
Inborn errors of metabolism	Chemotherapy and radiotherapy
Progressive organ failure causing toxic metabolites to build up	Medications, illicit drugs, and poisons

Two common imaging patterns of neurotoxicity of extrinsic nature are posterior reversible encephalopathy syndrome (PRES) and acute toxic leukoencephalopathy [5].

The pathogenesis of PRES is not well understood but is generally believed to be secondary to endothelial dysfunction due to exposure to exogenous toxins. Common causes include medications, including chemotherapeutic agents and steroids, infections, and transplantation (including bone marrow, stem cell, and solid organ transplantation). Common symptoms include headache, seizures, and encephalopathic features. Typically, there is bilateral vasogenic oedema of the parieto-occipital lobes, with sparing of the central white matter. Despite its name, frontal, temporal, and cerebellar regions can also be involved (frontal involvement is demonstrated in Figure 3). Atypical imaging patterns include purely unilateral involvement, brainstem or basal ganglia involvement without cortical white matter involvement (also known as central PRES), and spinal cord involvement. Progression to infarction and haemorrhage can also be seen. The various manifestations of PRES can sometimes make diagnosis challenging; therefore, correlation with clinical features as well as predisposing factors is important. Supportive treatment and removal of the offending agent are required.

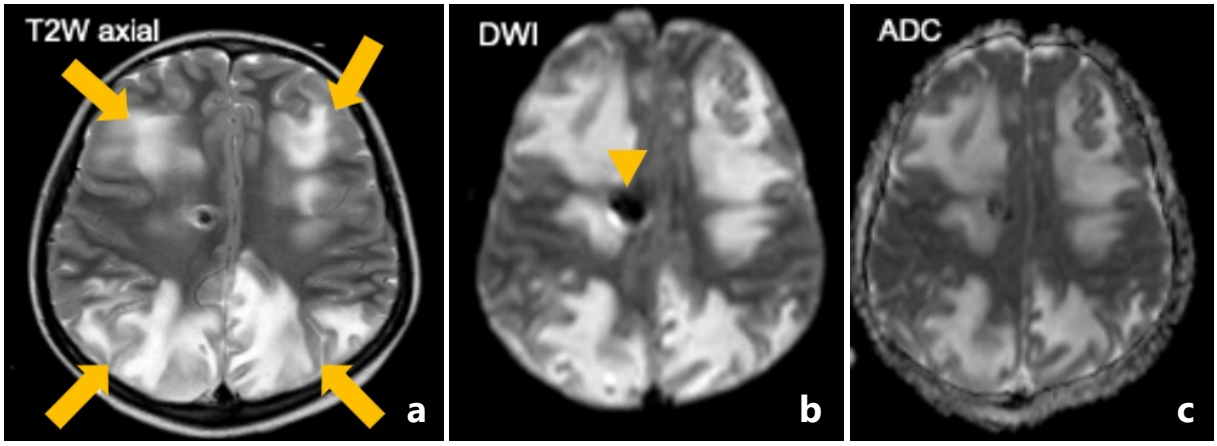

Figure 3. *Non-enhanced MRI brain of a 13-year-old patient on induction chemotherapy for acute lymphoblastic leukaemia, presenting with seizures and labile hypertension [6]. (a) The T2 sequence shows bilateral symmetrical parenchymal abnormalities (arrows) with DWI (b) and ADC sequences (c) showing vasogenic oedema. These findings are consistent with PRES. An extra-ventricular drainage catheter was inserted for monitoring of intracranial pressure (arrowhead).*

Acute toxic leukoencephalopathy is a neurotoxic condition that predominantly damages the white matter. It is most commonly secondary to medications, namely methotrexate and other chemotherapeutic agents such as fluorouracil. Methotrexate use is the most common cause among the paediatric oncological population, and the risk increases with high-dose regimens and intrathecal administration. These patients typically present 2-4 weeks after methotrexate administration. Sepsis and metabolic abnormalities such as uraemia are less common causes. Clinical presentations vary and can range from a decreased level of consciousness to more severe manifestations including hemiplegia and aphasia. On imaging, these typically manifest as restricted diffusion in the unilateral or bilateral centrum semiovale, which crosses vascular territories. In contrast, restricted diffusion is only present in 25% of PRES cases. Treatment with aminophylline and leucovorin may aid in reversing the acute parenchymal changes.

THE ASEAN JOURNAL OF RADIOLOGY
ISSN 2672-9393

Infections

Neonatal infections of the brain are often non-specific. Early imaging, particularly MRI, aids in early diagnosis, which can avoid devastating outcomes including neurodevelopmental delay.

Neonatal leptomeningitis occurs in 0.4% of births. The commonest pathogens are group B streptococcus and Escherichia coli [7]. Imaging findings include enlargement of the subarachnoid spaces, subdural effusions (Figure 4) as well as leptomeningeal thickening and enhancement (Figure 5). Parenchymal involvement could lead to cerebritis and cerebral liquefaction. Inflammation of meninges can also affect the perivascular spaces, leading to infarction. This occurs in approximately 10% of neonates with meningitis [8]. Other complications include cerebral abscesses and empyema formation.

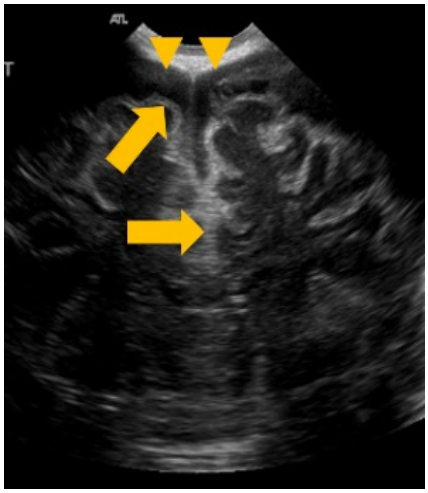

Figure 4. *USG brain of a 5-month-old infant presenting with late-onset GBS meningitis. There is marked leptomeningeal thickening (arrow) and bilateral subdural effusions (arrowhead), causing mild mass effect on the underlying brain.*

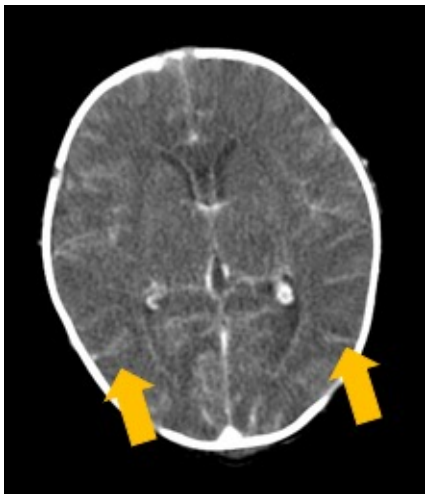

Figure 5. *Contrast-enhanced CT brain of a term infant presenting on the day of birth with septic shock, respiratory failure, and leptomeningitis. There is marked cerebral oedema with effacement of the sulcal spaces, while the lateral ventricles demonstrate increased ependymal enhancement and mild dilatation. Increased leptomeningeal enhancement is also noted (arrows).*

Viral encephalitis is commonly caused by herpes simplex virus (HSV) types 1 and 2, cytomegavirus (CMV) and human herpesvirus-6 (HHV) HHV-6. Patients in the early post-transplant period following haematopoietic stem cell transplantation are particularly at risk. Imaging features are non-specific, though abnormal T2 hyperintensities involving both grey and white matter are often seen. Associated restricted diffusion caused by cytotoxic oedema is also a common feature (Figure 6). Classic imaging patterns associated with different viruses have also been described. In CMV infections, there is periventricular white matter involvement with ependymal enhancement. In HSV infections, the limbic system and periventricular white matter are often involved, and the basal ganglia is typically spared. HHV-6 affects the limbic system, with involvement of the hippocampus and amygdala. Of note, these classical findings are sometimes absent due to the patients' impaired immune response.

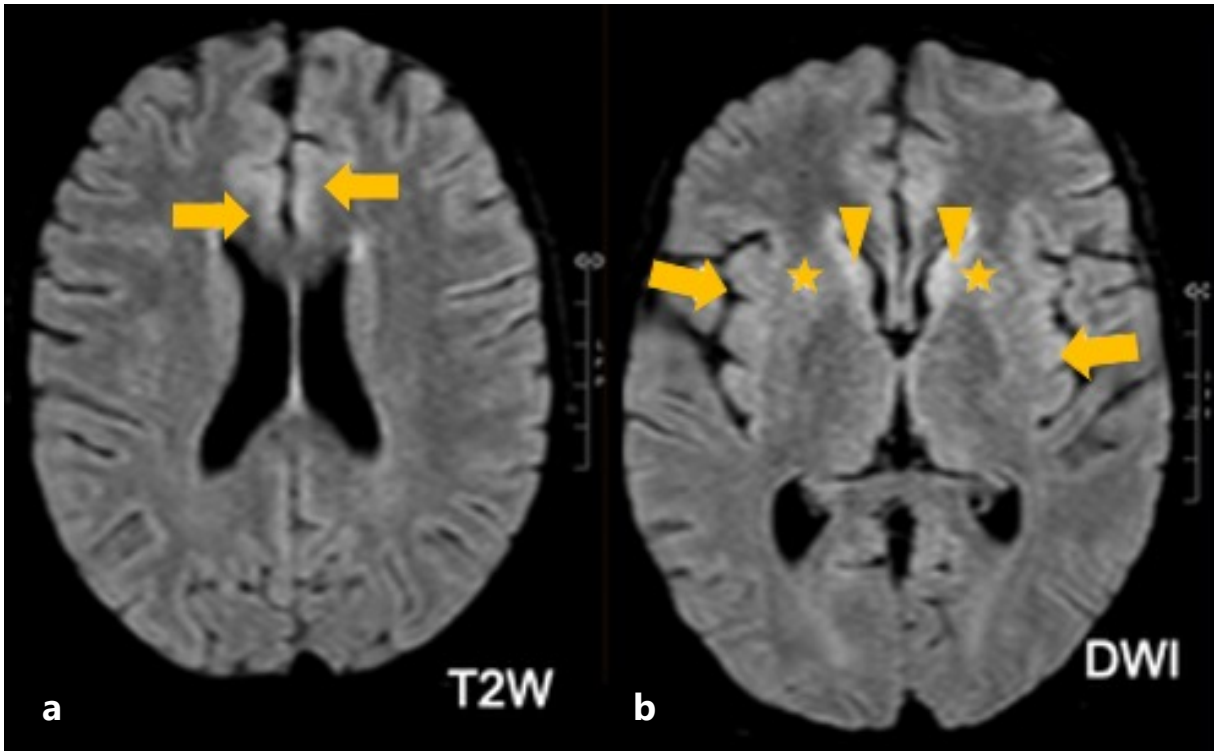

Figure 6. *MRI brain of a patient with acute myeloblastic leukaemia, following peripheral blood stem cell transplantation [6]. There are abnormally high T2 signals in the bilateral medial frontal lobes (a), anterior putamina (b, asterisks), caudate heads (b, arrowheads) and insula (b, arrows). Findings may suggest, but not limited to, viral encephalitis.*

Among immunosuppressed patients, invasive fungal disease is a devastating complication with a high rate of mortality and morbidity. Unfortunately, clinical signs and symptoms are often non-specific, posing difficulties for early diagnosis. More common CNS-related symptoms include headache, seizures, and impaired vision. Radiological findings are also often non-specific. CT is commonly the initial imaging modality as it allows rapid assessment of potential complications including haemorrhage, hydrocephalus, and brain abscess. MRI, on the other hand, is more sensitive in the diagnosis of meningitis (Figure 7), cerebritis, and ventriculitis.

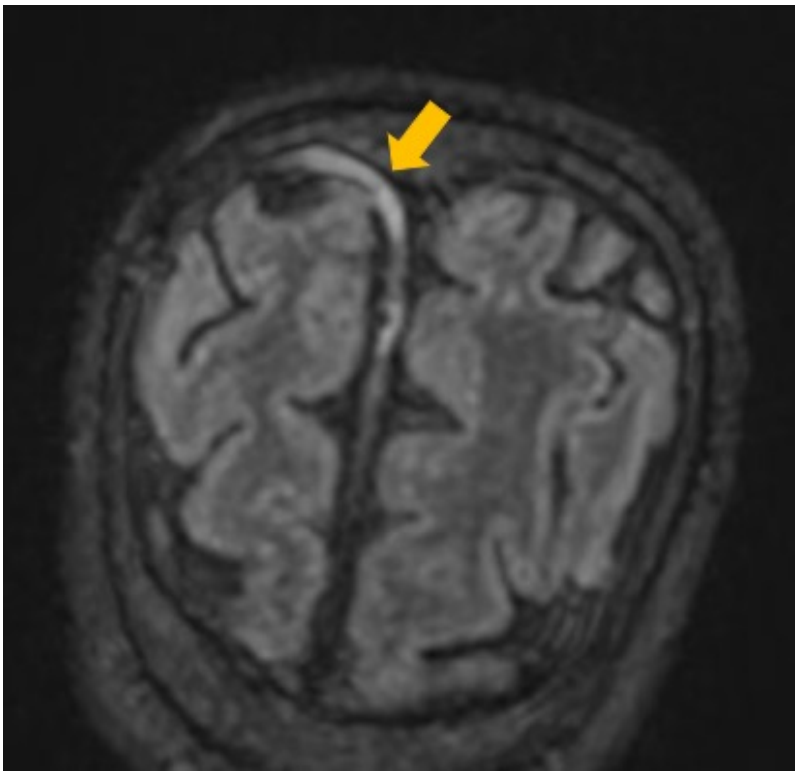

Figure 7. *Contrast-enhanced MRI brain of a 14-year-old boy with acute myeloblastic leukaemia [6]. He had invasive fungal infection involving the right nasal cavity and maxillary sinus. Contrast-enhanced MRI shows increased dural enhancement along the right frontal anterior falx (arrow), suggestive of intracranial extension of infection.*

Autoimmune Disorders

Associations and risk factors for central nervous system (CNS) autoimmunity are heterogeneous. Genetic defects can lead to immune disorders, resulting in autoimmune and lymphoproliferative diseases and immunodeficiency. Environmental factors, including exposure to hormones, and vitamin D levels, also play important roles. Infection and neoplasm are common triggers for first presentations and flare-ups. Autoimmune CNS conditions can be divided into primary CNS diseases and systemic autoimmune conditions with CNS involvement (Table 2).

Table 2. *Examples of primary CNS conditions and systemic conditions with CNS involvement.*

Primary CNS conditions	Systemic conditions
Multiple sclerosis	SLE
Acute disseminated encephalomyelitis	Sarcoidosis
Neuromyelitis optica spectrum disorder	Behcet's
Autoimmune encephalitis	Granulomatosis with polyangiitis
Primary vasculitis	Scleroderma
	Sjogren's syndrome
	Thrombotic microangiopathies
	Aicardi Gouteire
	Hemophagocytic lymphohistiocytosis

An example of a primary CNS autoimmune disorder is acute disseminated encephalomyelitis (ADEM), which is a clinical diagnosis that describes an acute presentation of polyfocal demyelination, accompanied by encephalopathy. It is usually a monophasic disorder. Peak onset occurs between 5 and 8 years of age, and a history of recent infection or vaccination is common. Commonly involved regions include the grey matter, particularly the basal ganglia, subcortical white matter, thalami and brainstem (Figure 8). The spinal cord may also be involved to a lesser extent (Figure 9).

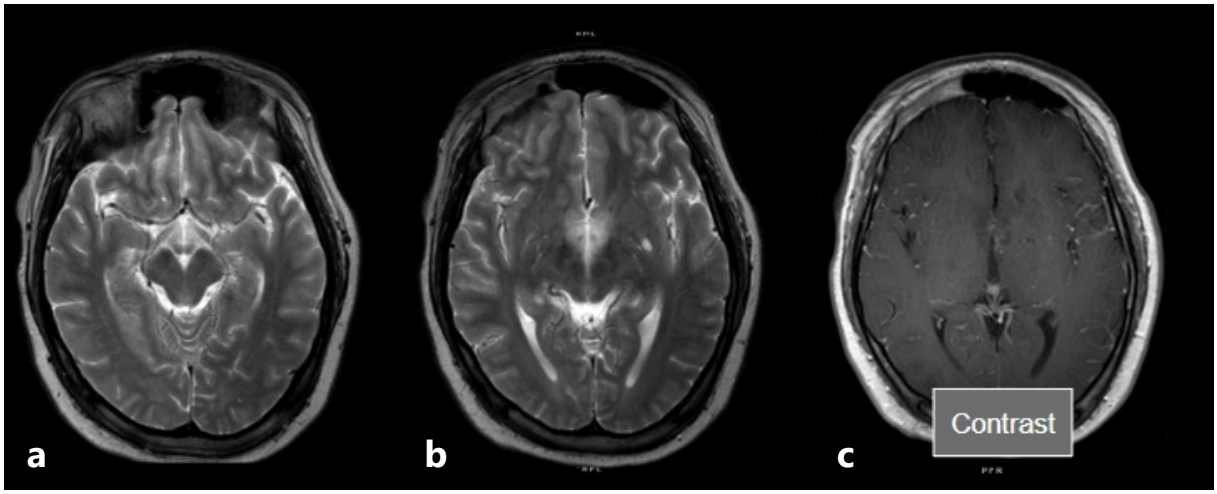

Figure 8. *Contrast-enhanced MRI brain of a 16-year-old patient with ADEM presenting with acute-onset bilateral lower limb weakness, acute retention of urine, and a sensory level at T4. On T2-weighted sequences, there are bilateral symmetrical T2 hyperintense signals in the bilateral paraterminal gyri (a, b), extending to the mamillary bodies. Post-contrast imaging shows mild leptomeningeal enhancement (c).*

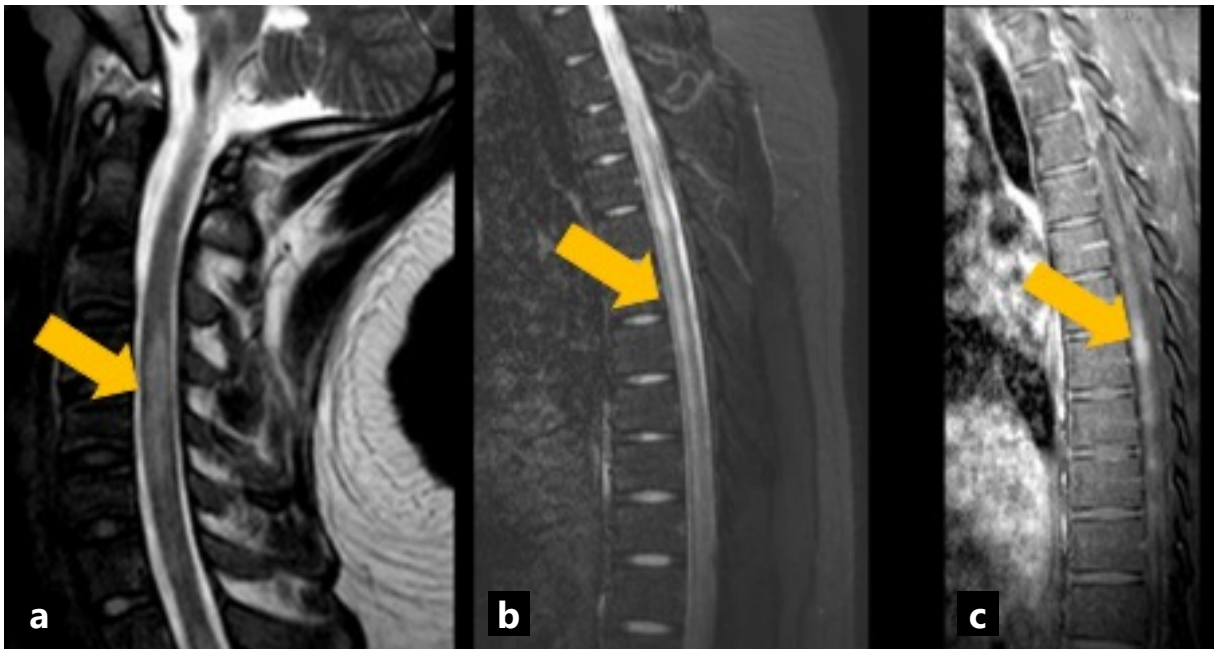

Figure 9. *CMRI spine of the same patient as Figure 8. Extensive T2 hyperintense signals are seen involving C4-7, T1-11 (a, b) with patchy enhancement on post-contrast sequences (c).*

A less common example of primary CNS autoimmune disorder is steroid-responsive encephalopathy associated with autoimmune thyroiditis (SREAT), also known as Hashimoto's encephalopathy. This is a rare autoimmune encephalitis associated with autoimmune thyroid disease. Imaging findings are non-specific. Reported MRI findings include white matter T2W hyperintensity and dural enhancement (Figure 10).

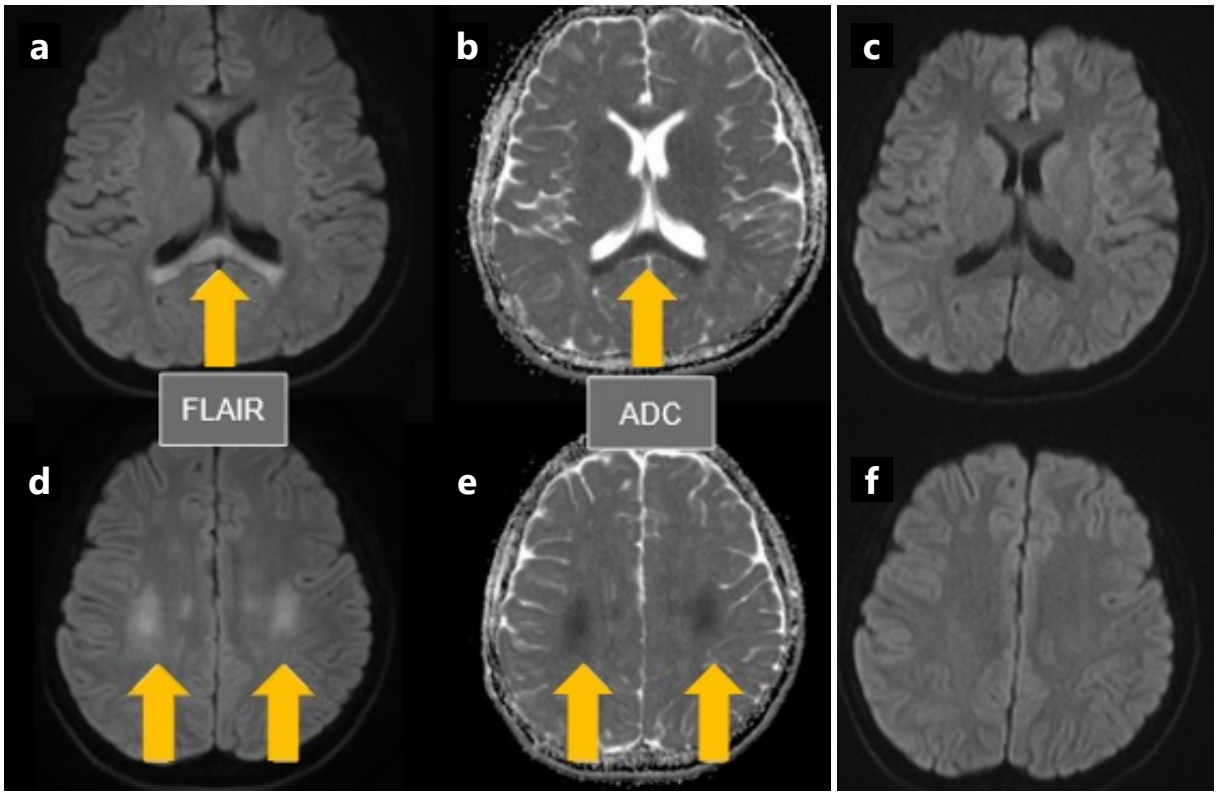

Figure 10. *Non-enhanced MRI brain of a 10-year-old patient with SREAT, who presented with thyroid storm and sudden onset of confusion and aphasia, with a GCS of 9/15. MRI FLAIR sequence shows T2 hyperintense and T1 hypointense signals in the splenium of corpus callosum (a, c, arrow) and bilateral centrum semiovale (b, d arrow). Non-enhanced MRI brain (e, f) FLAIR sequence of the same patient after 11 days of treatment (methylprednisolone and plasma exchange) demonstrates resolution of previously noted T2/FLAIR hyperintense signals.*

THE ASEAN JOURNAL OF RADIOLOGY
ISSN 2672-9393

Stroke

Stroke is rare in the paediatric population, with an incidence of 2.3-13 per 100,000 children. However, it is one of the commonest causes of childhood death [9]. Unlike the adult population, paediatric stroke is evenly distributed between ischaemic and haemorrhagic subtypes. Risk factors also differ, with arteriopathies, congenital heart disease, prothrombotic conditions, sickle cell disease, and vasculitis being common risk factors. Ischaemic stroke is further divided into arterial ischaemic stroke and cerebral sinovenous thrombosis (Table 3). While acute ischaemic stroke presents as focal neurological deficits, most patients with cerebral sinovenous thrombosis and haemorrhagic stroke present with non-specific symptoms, including headache and seizures.

Table 3. *Comparison between arterial ischaemic stroke and cerebral sinovenous thrombosis.*

Arterial ischaemic stroke	Cerebral sinovenous thrombosis
Focal deficit localising to an arterial distribution	Non-specific symptoms: headache, papilledema, nausea, seizures
Arteriopathies (moyamoya vasculopathy, focal cerebral arteriopathy, or dissection), congenital heart disease, prothrombotic conditions, sickle cell disease, systemic vasculitis	Head and neck disorders, acute and chronic systemic illnesses, prothrombotic states

One example of arterial ischaemic stroke is focal cerebral arteriopathy of childhood, which is associated with a high risk of recurrent ischaemic stroke. This condition is believed to be inflammatory, classically caused by Varicella zoster infections, and Herpes infections in some cases. MRI angiography can be used to visualise unilateral stenosis of the distal internal carotid artery, and proximal middle and/or anterior cerebral arteries. Vessel wall imaging could reveal wall thickening and concentric enhancement.

Intracranial venous thrombosis is associated with the use of L-asparaginase and high-dose corticosteroids (Figure 11). Key imaging findings include hyperattenuated and expanded veins on non-enhanced CT, filling defects and the “empty delta” sign on CT venography, and infarcts that are not confined to an arterial territory. Haemorrhagic infarcts can also be seen.

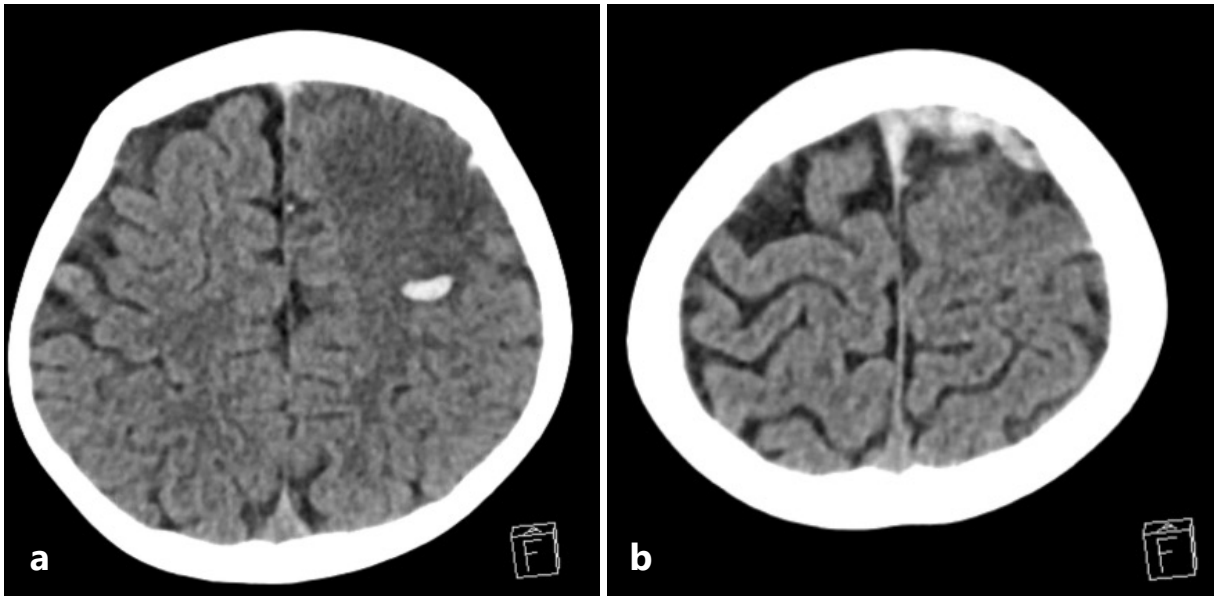

Figure 11. *Non-enhanced CT brain of a 6-year-old boy with acute lymphoblastic leukaemia who had received L-asparaginase and high-dose corticosteroids. (a) Hypodensity involving the left frontal lobe with loss of grey-white differentiation, suggestive of a recent infarct with an acute haematoma. (b) Hyperdensity within the superior sagittal sinus near the vertex with extra-axial curvilinear hyperdensities, suggestive of venous thrombosis and subdural haemorrhage.*

Seizures

Seizures are transient occurrences of signs and/or symptoms due to abnormally excessive or synchronous neuronal activity in the brain. Epilepsy refers to recurrent and unprovoked seizures. These range from the benign and self-limiting simple febrile seizures to life-threatening status epilepticus. The Centers for Disease Control and Prevention estimate that approximately 0.6% of children younger than 17 years of age suffer from epilepsy [10]. Status epilepticus is the commonest neurologic emergency in children. Underlying causes include genetic factors and intracranial and systemic abnormalities.

THE ASEAN JOURNAL OF RADIOLOGY
ISSN 2672-9393

Children with neurometabolic disease can present with seizures. For example, urea cycle disorders are caused by a deficiency of enzymes that convert ammonia to urea. Hyperammonaemia results in diffuse generalised oedema involving the cerebral cortex and the subcortical white matter, which could be caused by increased levels of glutamine resulting from the metabolism of ammonia. In addition, the basal ganglia may show abnormal signal intensities, including T1 and T2 hyperintensities of the globus pallidi and T2 hyperintensity of the putamina and caudate nuclei. This pattern of basal ganglia involvement distinguishes urea cycle disorders from hypoxic-Ischemic encephalopathy. While T1 and T2 findings are relatively non-specific, a scalloped ribbon pattern of injury at the depth of sulci on diffusion-weighted imaging strongly supports the diagnosis (Figure 12).

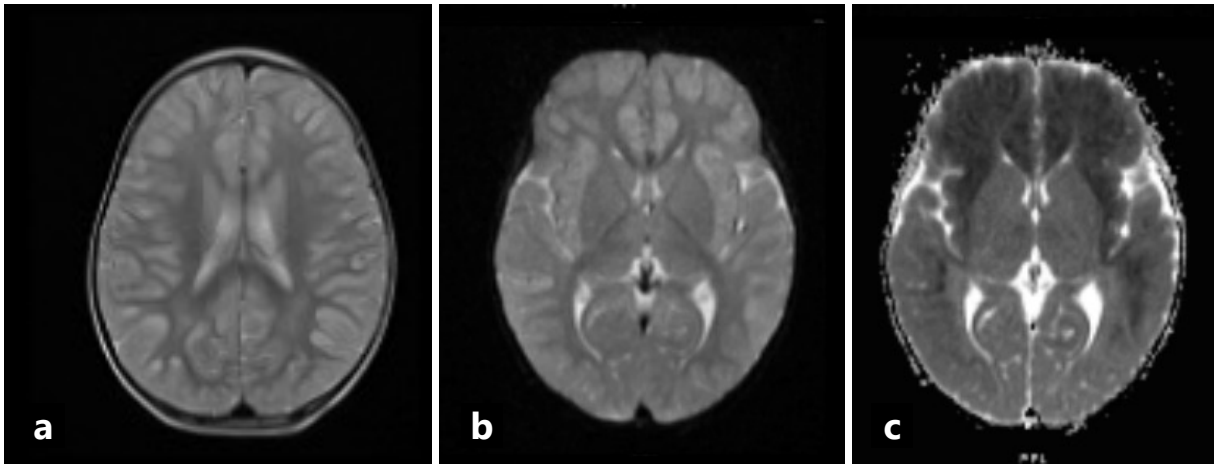

Figure 12. *Non-enhanced MRI brain of a 2-year-old boy with hyperammonaemia, presenting with seizures. (a) A T2 weighted sequence shows increased T2 signals in the bilateral subcortical white matter. (b) DWI and (c) ADC images show wavy bands of restricted diffusion at the cortical-subcortical junction of the insular regions (also known as the deep sulcus sign).*

Conclusion

Acute paediatric neurological diseases can result in morbidity and mortality, yet they commonly present with non-specific symptoms. In this article, we reviewed common acute critical neurological diseases in the paediatric population. Imaging can help identify specific entities when provided with a precise clinical history and unequivocal imaging findings, such as the diagnosis of empyema in a patient with known meningitis. In other cases, imaging can help localise abnormalities that correlate with specific clinical findings, such as anatomical localisation in autoimmune diseases or acute ischaemic stroke. Even when both clinical and radiological findings are inconclusive, imaging features can often help narrow the list of differential diagnoses. Thus, imaging plays a pivotal role in the accurate and timely diagnosis of critical neurological diseases.

Conflicts of interest

The authors declare no conflict of interest.

References

1. Moreau JF, Fink EL, Hartman ME, Angus DC, Bell MJ, Linde-Zwirble WT, et al. Hospitalizations of children with neurologic disorders in the United States. Pediatr Crit Care Med. 2013;14: 801-10. doi:10.1097/PCC.0b013e31828aa71f.

2. Pollina J, Dias MS, Li V, Kachurek D, Arbesman M. Cranial birth injuries in term newborn infants. Pediatr Neurosurg 2001;35:113-9. doi:10.1159/000050403.

3. King S J, Boothroyd AE. Cranial trauma following birth in term infants. Br J Radiol 1998;71:233-8. doi:10.1259/bjr.71.842.9579191.

4. Bradford R, Choudhary AK, Dias MS. Serial neuroimaging in infants with abusive head trauma: timing abusive injuries. J Neurosurg Pediatr 2013;12:110-9. doi:10.3171/2013.4.PEDS12596.

5. Kontzialis M, Huisman TAGM. Toxic-metabolic neurologic disorders in children: A neuroimaging review. J Neuroimaging 2018;28:587-95. doi:10.1111/jon.12551.

6. Cheung C, Fung KFK, Ng CWK, Chan PKJ, Wong KC, Lam KSG, et al. Treatment-related complications in children with cancer. Radiographics 2024;44: e230072. doi:10.1148/rg.230072.

7. Zhai Q, Li S, Zhang L, Yang Y, Jiang S, Cao Y. Changes in pathogens of neonatal bacterial meningitis over the past 12 years: A single-center retrospective study. Transl Pediatr 2022;11:1595-603. doi:10.21037/tp-22-103.

8. Friede RL. Cerebral infarcts complicating neonatal leptomeningitis. Acute and residual lesions. Acta Neuropathol 1973;23:245–53. doi: 10.1007/BF00687879.

9. George MP, Kim WG, Lee EY. Tales from the night:: Emergency MR imaging in pediatric patients after hours. Magn Reson Imaging Clin N Am 2019;27: 409-26. doi:10.1016/j.mric.2019.01.013.

10. Census Bureau US, US Department of Commerce. 2022 National Survey of Children's Health: methodology report. Accessed March 21, 2026. https://www2.census.gov/programs-surveys/nsch/technical-documentation/methodology/2022-NSCH-Methodology-Report.pdf

ASEAN Movement in Radiology

Computed tomography (CT) scanner imports in Vietnam (2023–2025): Market growth, technology structure, and manufacturer distribution in an ASEAN Context

Canh Nguyen Bui, M.D, M.Sc.[(1)]
Trieu Nghi Hoang, Ph.D.[(2)]
Ngoc Nguyen Thi, M.D.[(3)]
Uyen Bao Nguyen, Ph.D.[(4)]
Nam Thanh Pham, M.Sc.[(5)]
From [(1)]GE Healthcare Vietnam Co., Ltd. Ho Chi Minh City, [(2)]Ngoc Minh Clinic, Ho Chi Minh City, [(3)]Novartis Vietnam Co., Ltd., Hanoi, [(4)]Private Healthcare Association of Vietnam, Hanoi, [(5)]JVC Vietnam Co., Ltd., Hanoi, Vietnam.
Address correspondence to C.N.B. (email: onionsnguyencanh@gmail.com)

Received 12 February 2026; revised 22 April 2026; accepted 26 April 2026
doi:10.46475/asean-jr.v27i2.1019

Keywords: ASEAN health systems, CT scanner, Diagnostic imaging, Medical device import, Vietnam.

Introduction

Computed tomography (CT) is indispensable in contemporary diagnostic imaging, enabling accurate assessment across emergency medicine, oncology, neurology, and cardiovascular care [1,2]. In ASEAN countries, the distribution and technological level of CT scanners represent key indicators of health system capacity [3-5]. Vietnam has experienced substantial healthcare growth over the past decade, yet systematic evidence describing CT procurement trends remains limited.

Materials and methods

This study utilized official national import data for CT scanners covering the period from 2023 to 2025. Data included manufacturer, slice category, year of import, and quantity. CT systems were grouped into four technology categories: low-end slice CT

THE ASEAN JOURNAL OF RADIOLOGY
ISSN 2672-9393

(≤64 slices), Mid-end slice CT (128–160 slices), and High-end slice CT (256–640 slices), and specialized CT systems.

Descriptive analysis was performed to examine trends and market structure. Statistical analysis was performed using R software (version 4.3.2; R Foundation for Statistical Computing, Vienna, Austria). Slice categories were treated as categorical variables and summarized as frequencies and percentages by year and manufacturer. Differences in the distribution of slice categories across years (2023–2025) manufacturer were assessed using the chi-square test of independence.

Given the exploratory and market-oriented nature of the analysis, statistical significance was defined at a two-sided p-value < 0.10. P-values between 0.05 and 0.10 were interpreted as indicative of trends rather than definitive statistical differences. Exact p-values are reported where appropriate.

Results

A total of 438 CT devices were included in the analysis, comprising 115 machines in 2023, 188 in 2024, and 171 in 2025. Across all years, the CT system with ≤64 slices constituted the largest proportion (305/438; 69.6%), followed by Mid-end slice CT (111/438; 25.3%) and High-end slice CT system (35/438; 8.0%). Advanced acquisition techniques, including PCCT and Simulation CT, accounted for a smaller proportion of the dataset (5/438; 1.1% and 22/438; 5.0%, respectively).

Comparative analysis using the chi-square test showed no statistically significant difference in the overall distribution of slice categories across the three years (χ^2 = 13.08, df = 8, p = 0.109). Although the overall comparison did not reach the predefined significance threshold, descriptive analysis revealed notable temporal patterns. Specifically, the number of CT systems with <64 slices increased substantially from 2023 to 2024, followed by a moderate decline in 2025, while medium- and high-end slice CT demonstrated a gradual increase over time. In addition, PCCT and Simulation CT slices were more frequently represented in 2025, suggesting an emerging trend toward the adoption of advanced imaging techniques in the later study period.

Overall, while the categorical distribution remained relatively stable across years, these findings indicate a temporal shift in data composition, characterized by increasing diversity in slice categories and imaging modalities.

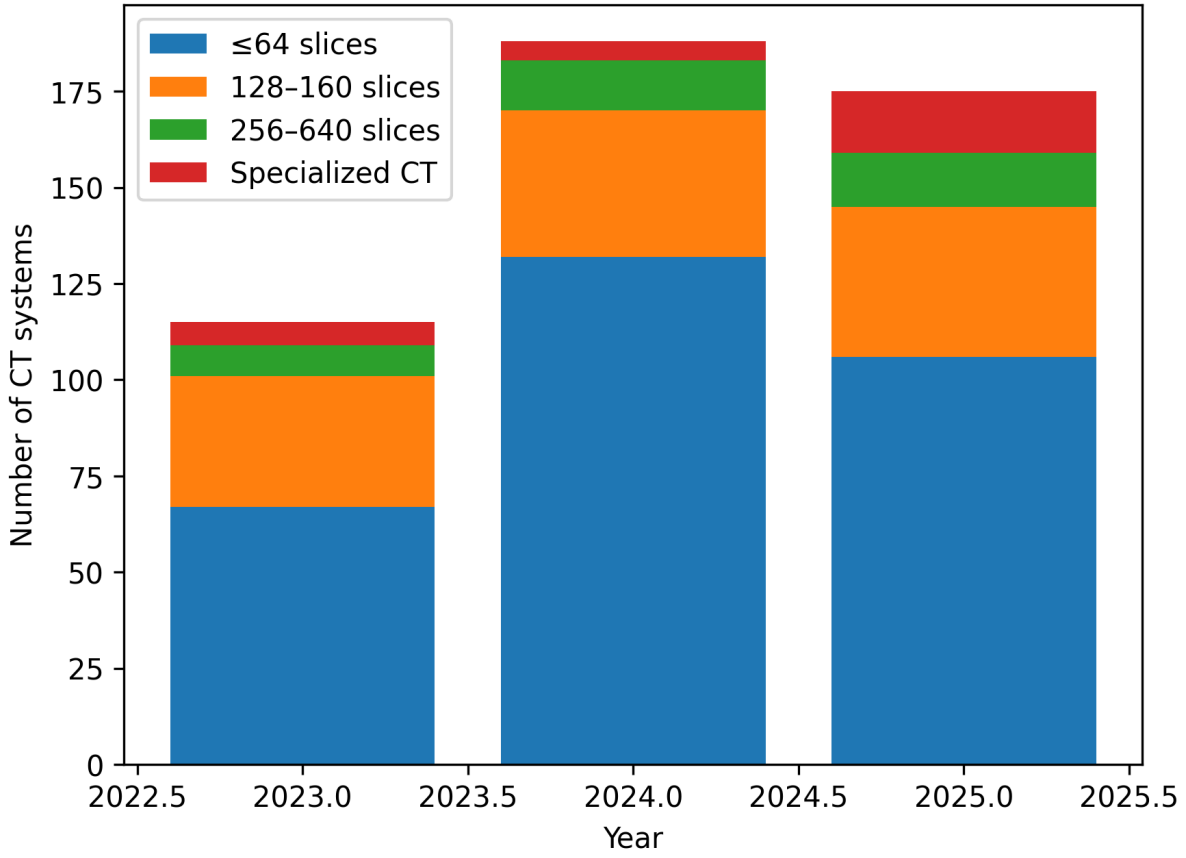

Slice category	2023	2024	2025	*Total*
≤64 slices	67	132	106	305
128–160 slices	34	38	39	111
256–640 slices	8	13	14	35
PCCT*	1	0	4	5
Simulation CT	5	5	12	22
Total	115	188	171	438

**Photon-counting CT*

Figure & Table 1. *Annual CT scanner imports in Vietnam by slice category (2023–2025).*

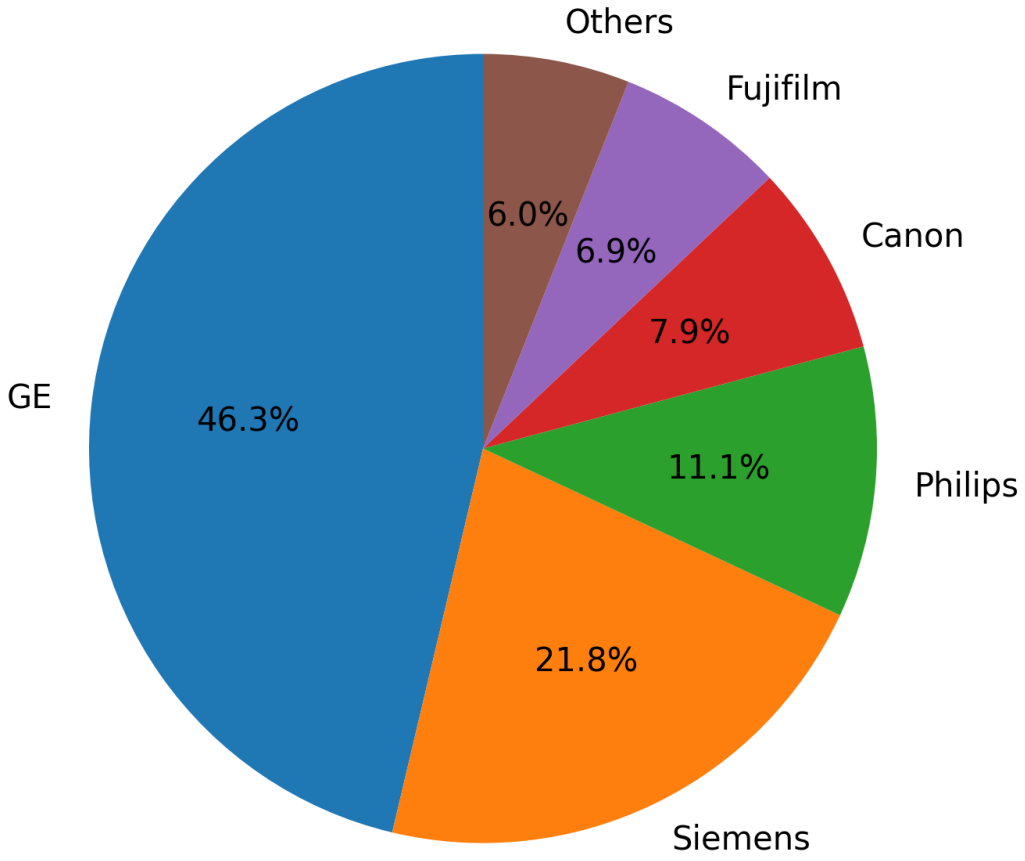

Manufacturer	Number of systems	Market share (%)
GE	100	46.3
Siemens	47	21.8
Philips	24	11.1
Canon	17	7.9
Fujifilm	15	6.9
Other manufacturers	13	6.0
Total	216	100.0

Figure & Table 2. *Market share of CT scanner manufacturers in Vietnam, 2025.*

A chi-square goodness-of-fit test demonstrated a statistically significant difference in market share among manufacturers (χ^2 = 124.56, df = 4, $p < 0.001$). GE Healthcare accounted for 46.3% of the total market, substantially exceeding the shares of the remaining manufacturers, each of which held less than 22%.

Discussion

Vietnam's CT scanner market demonstrates a clear transition from rapid baseline capacity expansion toward technological upgrading, consistent with broader ASEAN health system trends. Early growth was driven by deployment of ≤64-slice CT systems, while 2025 showed increased adoption of higher-slice and specialized CT technologies (Figure & Table 1).

In the early stages of market development, growth was principally driven by the deployment of ≤64-slice CT systems, which offered a cost-effective solution to address urgent diagnostic needs, particularly in regional and provincial healthcare settings [6]. These systems facilitated broad access to cross-sectional imaging, aligning with public health priorities to expand basic diagnostic infrastructure in the context of rising demand for imaging services [7,8].

As market penetration of basic CT technology approached saturation, there was an observable shift in investment toward higher-slice systems and specialized CT modalities. This transition reflects several converging factors. First, the increasing prevalence of complex diseases—such as oncologic, cardiovascular [2], and interstitial lung pathologies—requires higher spatial and temporal resolution for accurate diagnosis, staging, and treatment planning, which multi-slice CT and advanced technologies can better provide [9] Second, higher-slice CT equipment and advanced imaging capabilities, including photon-counting CT (PCCT) and simulation CT platforms, support enhanced workflows, improved image quality, and sophisticated analysis such as dose reduction and multiphase studies, making them attractive for tertiary care and private imaging centers [10,11].

Moreover, improvements in clinical expertise, information technology infrastructure, and healthcare policy frameworks have enabled more effective utilization of advanced imaging technology, reducing barriers to adoption and increasing demand for value-added services. The fact that advanced modalities such as PCCT [12] and Simulation CT are more prominent in 2025, data indicates a deepening of market maturity, where differentiation and quality of diagnostic output become central competitive factors rather than mere acquisition of additional basic units.

Overall, this pattern aligns with broader global trends in CT utilization and technology adoption, whereby emerging markets initially prioritize accessibility and basic capacity, and then progressively adopt sophisticated imaging solutions as clinical demand and economic capacity evolve [8,9]. Such transformation not only reflects technological progress but also underscores the increasing complexity of healthcare needs and expectations in Vietnam's evolving medical landscape.

GE Healthcare maintains market leadership through a broad portfolio and strong service infrastructure, contributing significantly to advanced cardiac and spectral CT adoption (Figure & Table 2). Siemens Healthineers dominates the premium segment with technological leadership in high-slice CT systems, though higher capital costs may moderate expansion. Philips remains competitive in mid-to-high segments, particularly in private hospitals. Canon Medical and Fujifilm demonstrate stable participation in mid-range and cost-sensitive segments. Smaller manufacturers collectively account for a minor but gradually increasing market share.

As an observational market-based analysis, this report primarily aims to provide a structured overview of CT technology diffusion in Vietnam. While it does not incorporate geographic or sectoral stratification, the findings offer a preliminary framework for understanding imaging capacity evolution in a rapidly developing ASEAN healthcare system. Future studies integrating regional distribution, public–private segmentation, and economic indicators would further strengthen health policy relevance.

Limitations

This study is based solely on national import data and does not include information on installation status, geographic distribution, public–private sector allocation, utilization rates, or clinical outcomes. Additionally, economic indicators were not incorporated into the current analysis. Future research integrating health system and economic data will be necessary to provide deeper policy-level insights.

Conclusion

CT scanner imports in Vietnam increased substantially between 2023 and 2025, with growing adoption of advanced and specialized technologies. These findings provide relevant evidence for imaging investment planning and policy development across ASEAN health systems.

References

1. Hussain S, Mubeen I, Ullah N, Shah SSUD, Khan BA, Zahoor M, et al. Modern diagnostic imaging technique applications and risk factors in the medical field: A review. Biomed Res Int 2022;2022:5164970. doi: 10.1155/2022/5164970.

2. Commandeur F, Goeller M, Dey D. Cardiac CT: Technological advances in hardware, software, and machine learning applications. Curr Cardiovasc Imaging Rep 2018; 11:19. doi: 10.1007/s12410-018-9459-z.

3. Alberto NRI, Alberto IRI, Puyat CVM, Antonio MAR, Ho FDV, Dee EC, et al. Disparities in access to cancer diagnostics in ASEAN member countries. Lancet Reg Health West Pac 2023;32:100667. doi: 10.1016/j.lanwpc.2022.100667.

4. Niki R. The wide distribution of CT scanners in Japan. Soc Sci Med 1985;21:1131-7. doi: 10.1016/0277-9536(85)90171-6.

5. TheGlobalEconomy.com [Internet]. 2026 [cited 2026 Apr 23]. Computed tomography scanners - Country rankings. Available from: https://www.theglobaleconomy.com/rankings/computed_tomography_scanners_per_million_people/South-East-Asia/

6. Reyes-Santias F, Antelo M. Explaining the adoption and use of computed tomography and magnetic resonance image technologies in public hospitals. BMC Health Serv Res 202;21:1278. doi: 10.1186/s12913-021-07225-2.

7. TechSci Research [Internet]. New York (NY): TechSci Research; 2025 [cited 2026 Apr 23]. Vietnam CT scanners market by slice (8-slice, 16-slice, 32-slice, 64-slice, 128-slice & above), by modality (fixed v/s mobile), by device architecture (O-arm v/s C-arm), by application (cardiology, oncology, neurology, others), by end users (hospitals, diagnostic centers, others), by region, competition forecast & opportunities, 2020-2030F. Available from: https://www.techsciresearch.com/report/vietnam-ct-scanners-market/8254.html

8. Research and Markets [Internet]. Dublin (Ireland): Research and Markets; 2025 [cited 2026 Apr 23]. Vietnam CT scanners market, by region, competition, forecast & opportunities, 2020-2030F. Available from: https://www.researchandmarkets.com/reports/5646390

9. Straits Research [Internet]. Pune (Maharashtra): Straits Research; 2026 [cited 2026 Apr 23].Bora D. CT Scanners market size, share & trends analysis report by technology (high-end slice CT, mid-end slice CT, low-end slice CT, cone beam CT (CBCT)), by application (oncology, cardiology, vascular, neurology, musculoskeletal, others), by end user (hospitals, diagnostic imaging centers, others) and by region (North America, Europe, APAC, Middle East and Africa, LATAM) forecasts, 2026-2034 Available from: https://straitsresearch.com/report/ct-scanners-market

10. Blue Weave Consulting [Internet]. Noida U.P. (India): Blue Weave Consulting; 2022 [cited 2026 Apr 23].Vietnam CT scanners market, by type (stationary, portable), by architecture (c-arm, o-arm), by application (cardiac, abdominal, spinal and musculoskeletal, oncology, brain and neurology), by slice (8-slice, 16-Slice, 32-slice, 64-slice, 128-slice, and above 128-slice), end-user (hospitals & clinics, diagnostic centre, ambulatory care, and others), trend analysis, competitive market share & forecast, 2018-2028. Available from: https://www.blueweaveconsulting.com/report/vietnam-ct-scanners-market

11. Jhaveri KS, Saini S, Levine LA, Piazzo DJ, Doncaster RJ, Halpern EF,et al. Effect of multislice CT technology on scanner productivity. AJR Am J Roentgenol 2001 ;177: 769-72. doi: 10.2214/ajr.177.4.1770769.

12. Meloni A, Frijia F, Panetta D, Degiorgi G, De Gori C, Maffei E, et al. Photon-counting computed tomography (PCCT): Technical background and cardio-vascular applications. Diagnostics (Basel) 2023;13:645. doi: 10.3390/diagnostics13040645.

ASEAN

This journal provide 4 areas of editorial services: language editing, statistical editing, content editing, and complete reference-citation check in 8 steps:

Step	Services to authors	Services providers
I	Manuscript submitted	Editor
II	Language editing/ A reference-citation check	Language consultant/Bibliographer
III	First revision to ensure that all information remains correct after language editing	Editor
IV	Statistical editing	Statistical consultant
V	Content editing*	Three reviewers
VI	Second revision	Editor
VII	Manuscript accepted/ rejected	Editor/Editorial board
VIII	Manuscript published	Editorial office

*Content editing follows a double-blind reviewing procedure

JOURNAL OF RADIOLOGY